Supporting Information

Tunable Optical Molecular Thermometers Based on Metallacrowns

Elvin V. Salerno,[†] Albano N. Carneiro Neto,[#] Svetlana V. Eliseeva,[*,‡] Miguel A. Hernández-Rodríguez,[#] Jacob C. Lutter,[†] Timothée Lathion,[†] Jeff W. Kampf,[†] Stéphane Petoud,[*,‡] Luis D. Carlos,[*,#] and Vincent L. Pecoraro[*,†]

[†] *Department of Chemistry, Willard H. Dow Laboratories, University of Michigan, Ann Arbor, Michigan 48109, United States. *Email: V. L. Pecoraro, vlpec@umich.edu*

[#] *Phantom-g, CICECO-Aveiro Institute of Materials, Department of Physics, University of Aveiro Campus de Santiago, Aveiro, Portugal. *Email: L. D. Carlos, lcarlos@ua.pt*

[‡] *Centre de Biophysique Moléculaire CNRS UPR 4301, 45071 Orléans Cedex 2, France. *E-mails: S. V. Eliseeva, svetlana.eliseeva@cnrs-orleans.fr; S. Petoud, stephane.petoud@inserm.fr*

Contents

1. X-ray single crystal and powder X-ray diffraction analysis

Structure refinement details. See main text for instrument description.

Colorless plates of **evs5075_sq** (Dy_2moshi_8) were grown from a dimethylformamide/water solution of the compound at 22 °C. A crystal of dimensions 0.12 x 0.12 x 0.02 mm was analyzed. The exposure times were 5 sec. for the low angle images, 45 sec. for the high angle. The integration of the data yielded a total of 237733 reflections to a maximum 2θ value of 139.17° of which 29633 were independent and 18606 were greater than 2σ(*I*). The final cell constants (**Table S2**) were based on the xyz centroids of 20032 reflections above 10σ(*I*). The structure was solved using the space group *P*2(1)/c with *Z* = 4 for the formula $C_{105}H_{89}N_{11}O_{56}Na_2Dy_2Ga_8(C_3H_7NO)_{7.5}(H_2O)_{3.5}$ + [solvent]. Full matrix least-squares refinement based on F^2 converged at $R_1 = 0.0695$ and $wR_2 = 0.1637$ [based on $I > 2\sigma(I)$], $R_1 = 0.1155$ and $wR_2 = 0.1897$ for all data.

Yellow plates of **jl7155_sq** (Sm_2nha_8) were grown from a dimethylformamide/water solution of the compound at 20 °C. A crystal of dimensions 0.08 x 0.07 x 0.02 mm was analyzed. A total of 4159 images were collected with an oscillation width of 1.0° in *w*. The exposure times were 1 sec. for the low angle images, 5 sec. for the high angle. The integration of the data yielded a total of 126426 reflections to a maximum 2θ value of 139.49° of which 4181 were independent and 3107 were greater than 2σ(*I*). The final cell constants (**Table S2**) were based on the xyz centroids of 35090 reflections above 10σ(*I*). The structure was solved using the space group *P*4/mnc with *Z* = 2 for the formula $C_{120}H_{64}N8O_{48}Na_2Ga_8Sm_2$, 5.5($H_2O$), [+ solvent]. All non-hydrogen atoms were refined anisotropically with the hydrogen atoms placed in idealized positions. The structure is characterized by significant disorder. Full matrix least-squares refinement based on F^2 converged at $R_1 = 0.0961$ and $wR_2 = 0.2989$ [based on $I > 2\sigma(I)$], $R_1 = 0.1056$ and $wR_2 = 0.3083$ for all data.

Colorless plates of **evs4001c_sq** (Tb_2mshi_8) were grown from a dimethylformamide/water solution of the compound at 20 °C. A crystal of dimensions 0.14 x 0.12 x 0.08 mm was analyzed. A total of 2028 images were collected with an oscillation width of 1.0° in *w*. The integration of the data yielded a total of 57958 reflections to a maximum 2θ value of 138.64° of which 1999 were independent and 1951 were greater than 2σ(*I*). The final cell constants (**Table S2**) were based on the xyz centroids of 24925 reflections above 10σ(*I*). The structure was solved using the space group *I*4/mmm with *Z* = 2 for the formula $C_{96}H_{68}N_8O_{44}Na_2Ga_8Tb_2$ [+ solvent]. Full matrix least-squares refinement based on F^2 converged at $R_1 = 0.0459$ and $wR_2 = 0.1384$ [based on $I > 2\sigma(I)$], $R_1 = 0.0466$ and $wR_2 = 0.1401$ for all data.

Table S1. Refinement parameters for the $Ln_2L'_8$ crystal structures.

Sample	Sm_2nha_8	Dy_2moshi_8	Tb_2mshi_8
Identification code	jl7155_sq	evs5075_sq	evs4001c_sq
Empirical formula	$C_{120}H_{72}Ga_8N_8Na_2O_{53.50}Sm_2$	$C_{127.50}H_{148.50}Ga_8N_{18.50}Na_2O_{67}Dy_2$	$C_{96}H_{68}Ga_8N_8Na_2O_{44}Tb_2$
Formula weight	3386.29	3940.88	2959.16
Temperature	85(2) K	85(2) K	85(2) K
Wavelength	1.54184 Å	1.54184 Å	1.54178 Å
Crystal system, space group	Tetragonal, *P*4/*mnc*	Monoclinic, *P*2(1)/*c*	Tetragonal, *I*4/*mmm*
Unit cell dimensions	a = 20.26971(8) Å, α = 90° b = 20.26971(8) Å, β = 90° c = 21.0036(2) Å, γ = 90°	a = 22.8934(4) Å, α = 90° b = 23.2819(4) Å, β = 108.988(3)° c = 31.5425(10) Å, γ = 90°	a = 19.28300(10) Å, α = 90° b = 19.28300(10) Å, β = 90° c = 20.0758(3) Å, γ = 90°
Volume	8629.57(11) Å^3	15897.4(7) Å^3	7464.87(14) Å^3
Z, Calculated density	2, 1.303 mg/m^3	4, 1.647 mg/m^3	2, 1.317 mg/m^3
Absorption coefficient	7.052 mm^{-1}	7.305 mm^{-1}	6.769 mm^{-1}
F(000)	3340	7924	2904
Crystal size	0.080 x 0.070 x 0.020 mm	0.120 x 0.120 x 0.020 mm	0.140 x 0.120 x 0.080 mm
Θ range for data collection	3.030 to 69.744°	2.787 to 69.586°	3.241 to 69.324°
Limiting indices	$-23 \le h \le 21$ $-24 \le k \le 24$ $-25 \le l \le 25$	$-27 \le h \le 27$ $-28 \le k \le 28$ $-38 \le l \le 38$	$-23 \le h \le 22$ $-23 \le k \le 23$ $-24 \le l \le 23$
Reflections collected / unique	126426 / 4181 [R(int) = 0.0720]	237733 / 29633 [R(int) = 0.1402]	57958 / 1999 [R(int) = 0.0529]
Completeness to Θ = 67.679	100.00%	99.90%	99.90%
Absorption correction	Semi-empirical from equivalents	Semi-empirical from equivalents	Semi-empirical from equivalents
Max. and *min.* transmission	1.00000 and 0.38114	1.00000 and 0.50193	1.00000 and 0.52245
Refinement method	Full-matrix least-squares on F^2	Full-matrix least-squares on F^2	Full-matrix least-squares on F^2
Data / restraints / parameters	4181 / 252 / 411	29633 / 277 / 2167	1999 / 6 / 173
Goodness-of-fit on F^2	0.987	1.106	1.145
Final R indices [$I>2\sigma(I)$]	R_1 = 0.0961, wR_2 = 0.2989	R_1 = 0.0695, wR_2 = 0.1637	R_1 = 0.0459, wR_2 = 0.1384
R indices (all data)	R_1 = 0.1056, wR_2 = 0.3083	R_1 = 0.1155, wR_2 = 0.1897	R_1 = 0.0466, wR_2 = 0.1401
Extinction coefficient	0.0014(2)	n/a	0.00024(4)
Largest diff. peak and hole	1.337 and –0.502 e$^-$Å^{-3}	2.004 and –1.340 e$^-$Å^{-3}	1.104 and –0.645 e$^-$Å^{-3}

Table S2. Unit cell parameters for Ln_2L_8 complexes (Ln = Dy, Sm, Gd, Tb; L' = shi^{3-}, $moshi^{3-}$, $mshi^{3-}$, nha^{3-}).

Complex	a (Å)	b (Å)	c (Å)	α (°)	β (°)	γ (°)	Volume (Å^3)
[a,b] Dy_2shi_8	14.108	17.581	19.220	113.11	102.70	98.22	4135.39
[b] Sm_2shi_8	14.152	17.741	19.188	112.91	102.71	98.27	4185.38
[b] Gd_2shi_8	14.104	17.581	19.217	113.09	102.60	98.35	4134.44
[b] Tb_2shi_8	14.105	17.595	19.248	113.24	102.63	98.16	4142.24
[a] Dy_2moshi_8	22.893	22.282	31.543	90	108.99	90	15897.40
Sm_2moshi_8	22.967	23.318	31.009	90	108.76	90	15725.01
Gd_2moshi_8	23.013	23.428	31.581	90	108.88	90	16110.06
Tb_2moshi_8	22.297	23.333	31.351	90	108.86	90	15870.77
Sm_2mshi_8	19.422	19.422	20.091	90	90	90	7578.58
Gd_2mshi_8	19.494	19.494	19.490	90	90	90	7406.47
[a] Tb_2mshi_8	19.283	19.283	20.076	90	90	90	7464.87
[a] Sm_2nha_8	20.27	20.27	21.01	90	90	90	8629.57

[a] Full structure was solved for this analogue. [b] Data previously presented.[1]

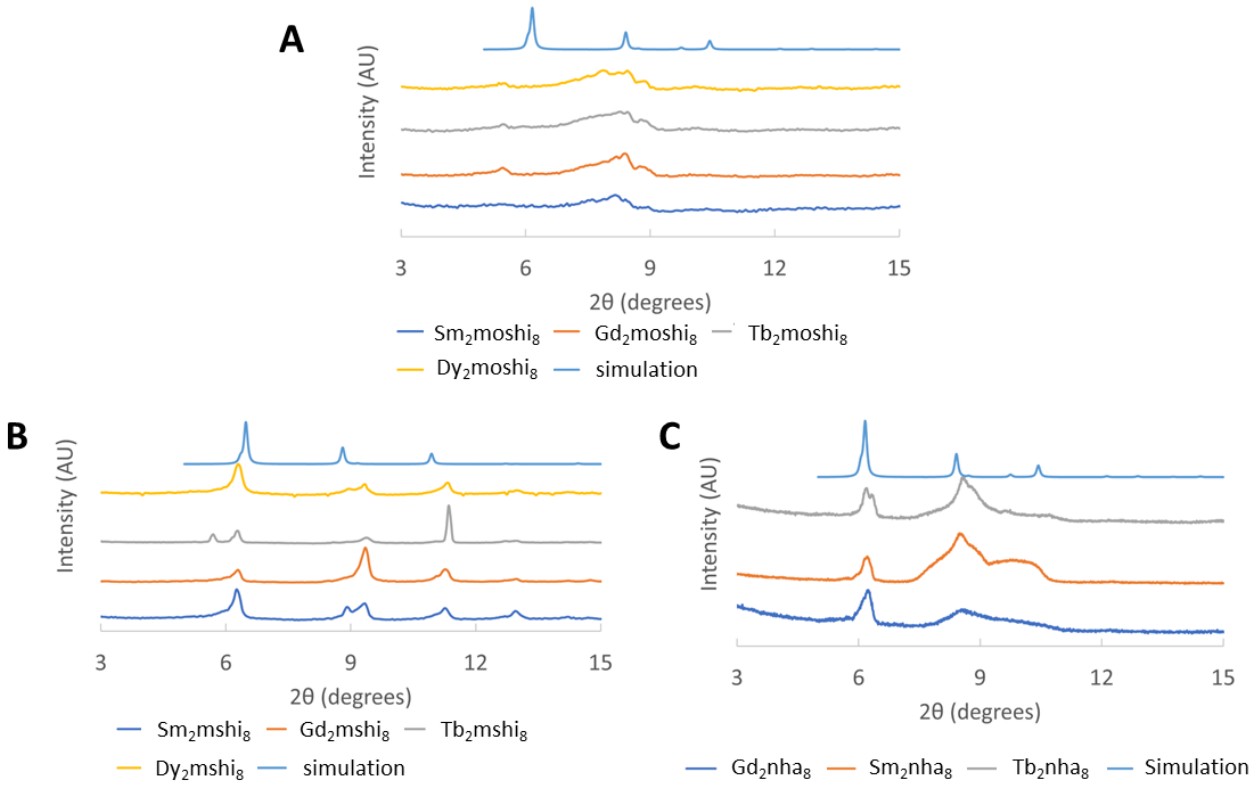

Figure S1. Powder X-ray diffraction (PXRD) data for novel $Ln_2L'_8$ complexes: **A**: L'=moshi, **B**: L'=mshi, **C**: L'=nha. The PXRD spectrum simulated from the crystal structure is presented for comparison. For **A**, simulated from crystal structure of Dy_2moshi_8; for **B**: from Tb_2mshi_8; for **C**: from Sm_2nha_8.

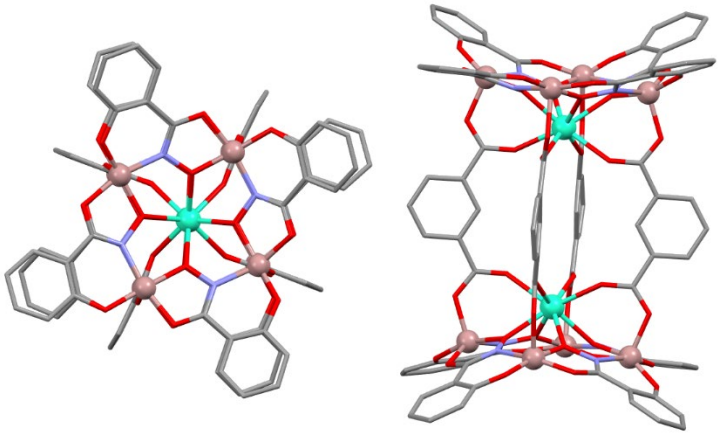

Figure S2. Top-down (left) and side-on (right) views of the Ln_2shi_8 complex. Color code: Ga, pink; Ln, green; O, red; N, blue; C, grey. Solvents, counter cations, and hydrogen atoms are omitted for clarity. The structure was solved previously for the Dy^{3+} analogue.[1]

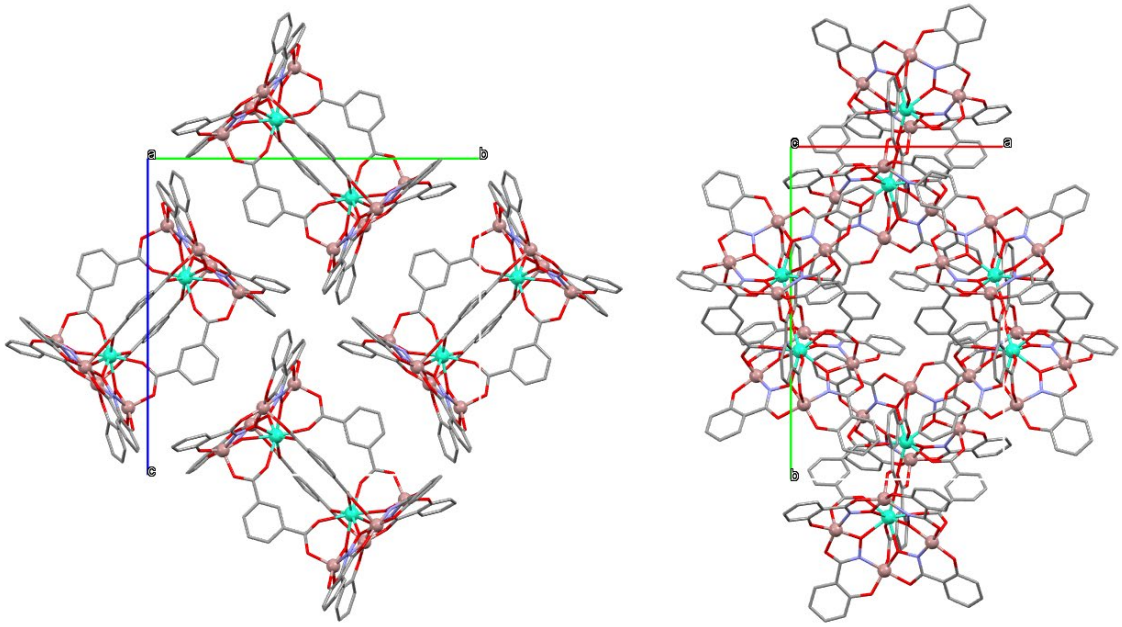

Figure S3. Unit cell packing for the Ln_2shi_8 complex as viewed along the crystallographic a-axis (left) and c-axis (right).

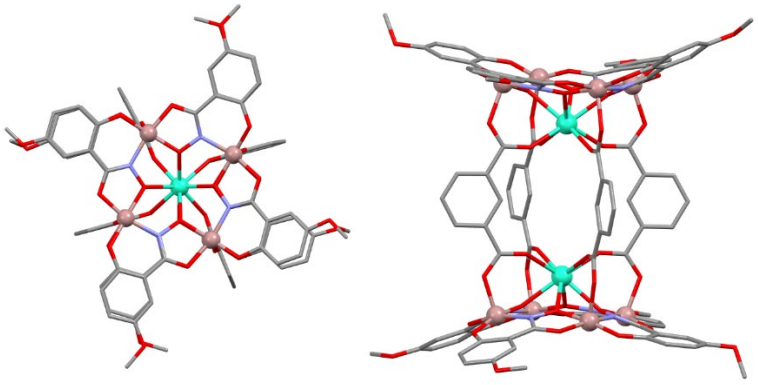

Figure S4. Top-down (left) and side-on (right) views of the Ln_2moshi_8 complex. Color code: Ga, pink; Ln, green; O, red; N, blue; C, grey. Solvents, counter cations, and hydrogen atoms are omitted for clarity. This structure was solved for the Dy^{3+} analogue.

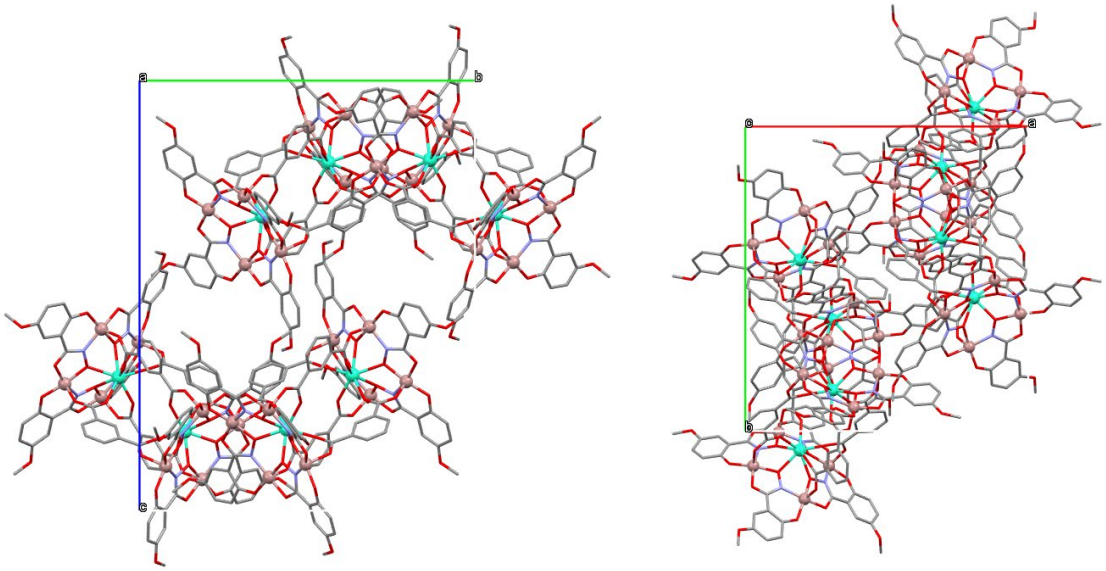

Figure S5. Unit cell packing for the Ln_2moshi_8 complex as viewed along the crystallographic a-axis (left) and c-axis (right).

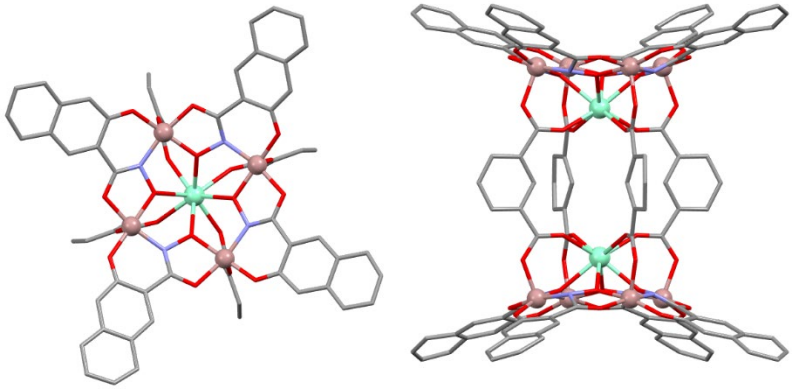

Figure S6. Top-down (left) and side-on (right) views of the Ln_2nha_8 complex. Color code: Ga, pink; Ln, green; O, red; N, blue; C, grey. Solvents, counter cations, and hydrogen atoms are omitted for clarity. The structure was solved for the Sm^{3+} analogue.

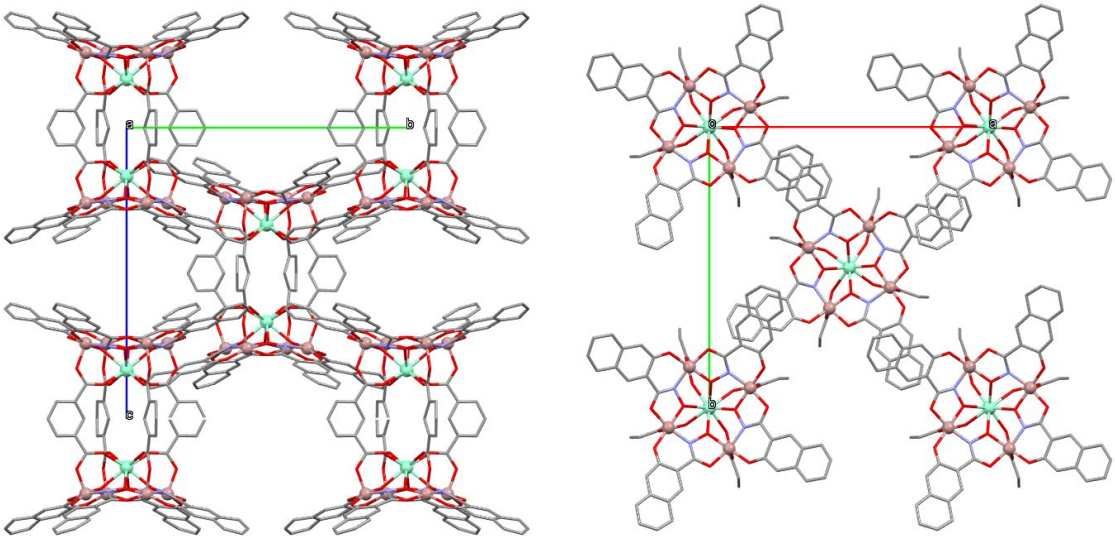

Figure S7. Unit cell packing for the Ln_2nha_8 complex as viewed along the crystallographic a-axis (left) and c-axis (right).

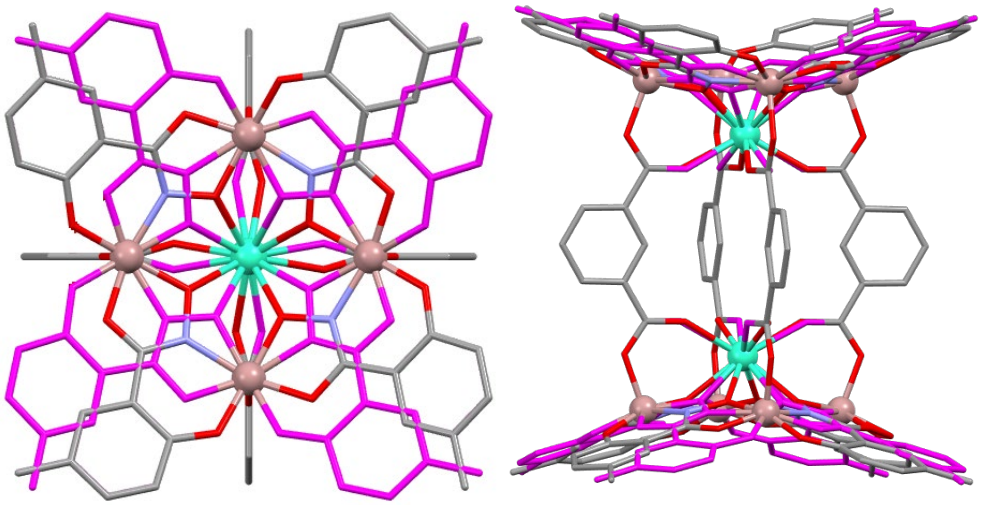

Figure S8. Top-down (left) and side-on (right) views of the Ln_2mshi_8 complex. Color code: Ga, pink sphere; Ln, green sphere; O, red; N, blue; C, grey. Solvents, counter cations, and hydrogen atoms are omitted for clarity. The structure was solved for the Tb^{3+} analogue. Multiple enantiomeric MC orientations are disordered within the crystal structure (**Figure S10**). The second isomer is shown in magenta. Positions of Ga, Dy, and (partially) bridging isophthalate ligands are shared between isomers.

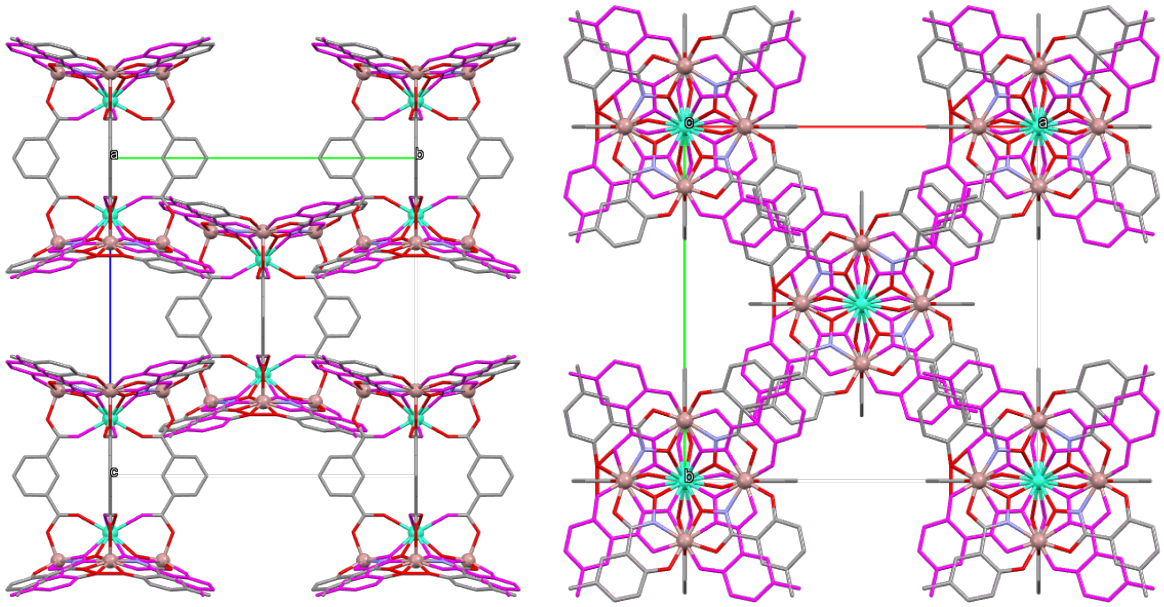

Figure S9. Unit cell packing for the Ln_2mshi_8 complex as viewed along the crystallographic a-axis (left) and c-axis (right). The second isomer is shown in magenta.

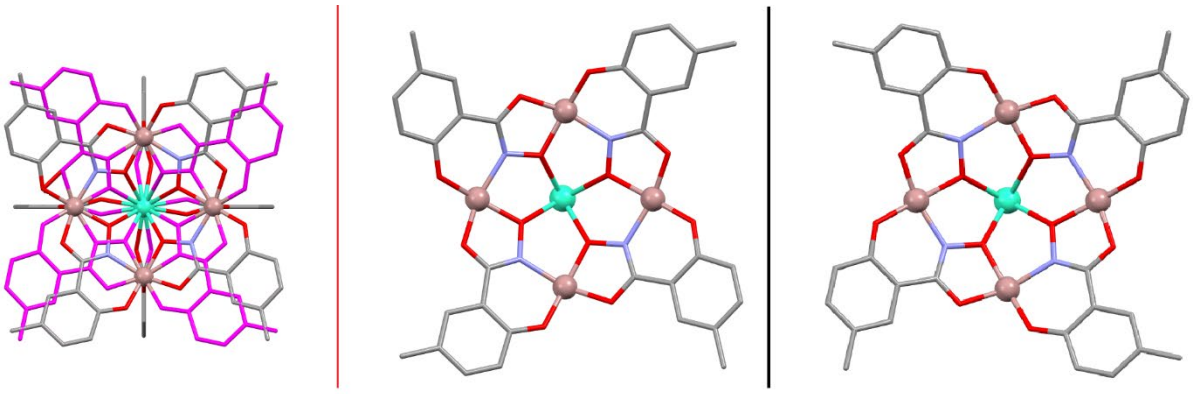

Figure S10. Representation of two distinct MC orientations in the crystal structure of Ln_2mshi_8. These are disordered across the crystal structure, here one isomer is shown in magenta (**left**). The first is a *C* (clockwise) MC ring of $[–Ga–N–O–]_4$ motif (when viewed with Ln^{3+} ion on the opposite side of the ring) (**center**). The second complex contains an *A* (anti-clockwise) MC ring of $[–Ga–O–N–]_4$ motif (**right**). The nature of these orientations is consistent with an enantiomeric (non-superimposable mirror-image) relationship between the two isomers such that the above structural description is applicable to both. Their physical properties will be generally identical.

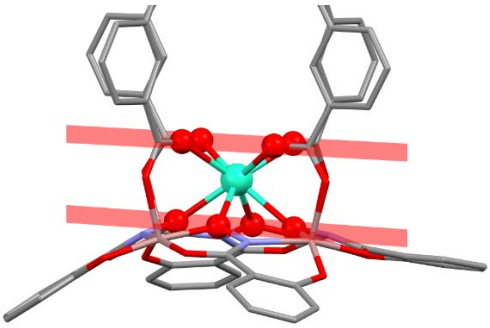

Figure S11. Example of the plane calculation for the Ln_2mshi_8 compound, corresponding to the measurements in **Table S2**. The upper is the Ln^{3+}-carboxylate O_4 plane and the lower is the Ln^{3+}-oxime O_4 plane.

Table S3. O_4–Ln^{3+} mean plane distance (Å) in each molecule, corresponding to the planes shown in **Figure S11**.

Distance (Å)	**Dy_2shi_8**	**Tb_2mshi_8**	**Dy_2moshi_8**	**Sm_2nha_8**
Ln^{3+}-oxime O_4 plane	1.408	1.474	1.487	1.546
Ln^{3+}-carboxylate O_4 plane	1.113	1.129	1.081	1.043

Table S4. Values of several closest (non-equivalent) Ln^{3+}-Ln^{3+} distances (Å) in each crystal structure

Ln^{3+}-Ln^{3+} Distance (Å)	**Dy_2shi_8**	**Tb_2mshi_8**	**Dy_2moshi_8**	**Sm_2nha_8**
Intramolecular	7.210	7.215	7.110	7.010
Closest intermolecular	12.805	13.924	13.385	14.752
2nd closest intermolecular	13.054	16.932	14.370	17.768
3rd closest intermolecular	14.820	19.283	15.005	20.270

SHAPE analysis for the crystal structures.[2,3] **Tables S5-S6** are related to the structure of Sm_2nha_8, for which all Ga^{3+} are crystallographically equivalent, and both Sm^{3+} are crystallographically equivalent. **Tables S7-S8** are related to the structure of Tb_2mshi_8, for which all Ga^{3+} are crystallographically equivalent, and both Tb^{3+} are crystallographically equivalent. **Tables S9-S18** are related to the structure of Dy_2moshi_8, for which 8 Ga^{3+} are in similar but non-equivalent environments, and for which 2 Dy^{3+} are in similar but non-equivalent environments.

Table S5. SHAPE Analysis for Sm1 in Sm_2nha_8

Geometry	Code	Point Group	CShM
Octahedron	OP-8	D_{8h}	30.32650
Heptagonal Pyramid	HPY-8	C_{7v}	23.94334
Hexagonal Bipyramid	HBPY-8	$D_{6hrystal}$	14.95499
Cube	CU-8	O_h	7.16208
Square Antiprism	SAPR-8	D_{4d}	0.84822
Trigonal Dodecahedron	TDD-8	D_{2d}	2.34601
Johnson Gyrobifastigium	JGBF-8	D_{2d}	16.48152
Johnson Elongated Triangular Bipyramid	JETBPY-8	D_{3h}	29.91867
Johnson Biaugmented Trigonal Prism	JBTPR-8	C_{2v}	3.35857
Biaugmented Trigonal Prism	BTPR-8	C_{2v}	2.09956
Johnson Snub Diphenoid	JSD-8	D_{2d}	5.84972
Triakis Tetrahedron	TT-8	T_d	8.04705
Elongated Trigonal Prism	ETBPY-8	D_{3h}	24.69338

Table S6. SHAPE Analysis for Ga1 in Sm_2nha_8

Shape	Shape Code	Point Group	CShM
Hexagon	HP-6	D_{6h}	31.76481
Pentagonal Pyramid	PPY-6	C_{5v}	27.95355
Octahedron	OC-6	O_h	0.99955
Trigonal Prism	TPR-6	D_{3h}	15.09858
Johnson Pentagonal Pyramid	JPPY-6	C_{5v}	31.63409

Table S7. SHAPE Analysis for Tb1 in Tb_2mshi_8

Geometry	Code	Point Group	CShM
Octahedron	OP-8	D_{8h}	30.65895
Heptagonal Pyramid	HPY-8	C_{7v}	23.82150
Hexagonal Bipyramid	HBPY-8	D_{6h}	15.62827
Cube	CU-8	O_h	7.89655
Square Antiprism	SAPR-8	D_{4d}	0.66048
Trigonal Dodecahedron	TDD-8	D_{2d}	2.37312
Johnson Gyrobifastigium	JGBF-8	D_{2d}	16.77068
Johnson Elongated Triangular Bipyramid	JETBPY-8	D_{3h}	29.94317
Johnson Biaugmented Trigonal Prism	JBTPR-8	C_{2v}	3.11306
Biaugmented Trigonal Prism	BTPR-8	C_{2v}	1.99780
Johnson Snub Diphenoid	JSD-8	D_{2d}	5.75595
Triakis Tetrahedron	TT-8	T_d	8.77460
Elongated Trigonal Prism	ETBPY-8	D_{3h}	24.92264

Table S8. SHAPE Analysis for Ga1 in Tb_2mshi_8

Shape	Shape Code	Point Group	CShM
Hexagon	HP-6	D_{6h}	32.31713
Pentagonal Pyramid	PPY-6	C_{5v}	27.75498
Octahedron	OC-6	O_h	0.96170
Trigonal Prism	TPR-6	D_{3h}	15.86193
Johnson Pentagonal Pyramid	JPPY-6	C_{5v}	31.38905

Table S9. SHAPE Analysis for Dy1 in Dy_2moshi_8

Geometry	Code	Point Group	CShM
Octahedron	OP-8	D_{8h}	30.98156
Heptagonal Pyramid	HPY-8	C_{7v}	23.46135
Hexagonal Bipyramid	HBPY-8	D_{6h}	16.19833
Cube	CU-8	O_h	8.95510
Square Antiprism	SAPR-8	D_{4d}	0.63790
Trigonal Dodecahedron	TDD-8	D_{2d}	2.50694
Johnson Gyrobifastigium	JGBF-8	D_{2d}	16.72578
Johnson Elongated Triangular Bipyramid	JETBPY-8	D_{3h}	29.55274
Johnson Biaugmented Trigonal Prism	JBTPR-8	C_{2v}	2.94697
Biaugmented Trigonal Prism	BTPR-8	C_{2v}	1.81433
Johnson Snub Diphenoid	JSD-8	D_{2d}	5.63831
Triakis Tetrahedron	TT-8	T_d	9.78331
Elongated Trigonal Prism	ETBPY-8	D_{3h}	25.03373

Table S10. SHAPE Analysis for Dy2 in Dy_2moshi_8

Geometry	Code	Point Group	CShM
Octahedron	OP-8	D_{8h}	30.62656
Heptagonal Pyramid	HPY-8	C_{7v}	23.60861
Hexagonal Bipyramid	HBPY-8	D_{6h}	15.99606
Cube	CU-8	O_h	8.86717
Square Antiprism	SAPR-8	D_{4d}	0.62800
Trigonal Dodecahedron	TDD-8	D_{2d}	2.49261
Johnson Gyrobifastigium	JGBF-8	D_{2d}	16.13797
Johnson Elongated Triangular Bipyramid	JETBPY-8	D_{3h}	29.16131
Johnson Biaugmented Trigonal Prism	JBTPR-8	C_{2v}	2.62131
Biaugmented Trigonal Prism	BTPR-8	C_{2v}	1.53792
Johnson Snub Diphenoid	JSD-8	D_{2d}	5.34228
Triakis Tetrahedron	TT-8	T_d	9.68935
Elongated Trigonal Prism	ETBPY-8	D_{3h}	24.76773

Table S11. SHAPE Analysis for Ga1 in Dy_2moshi_8

Shape	Shape Code	Point Group	CShM
Hexagon	HP-6	D_{6h}	31.02015
Pentagonal Pyramid	PPY-6	C_{5v}	27.43907
Octahedron	OC-6	O_h	0.44794
Trigonal Prism	TPR-6	D_{3h}	15.00979
Johnson Pentagonal Pyramid	JPPY-6	C_{5v}	30.91932

Table S12. SHAPE Analysis for Ga2 in Dy_2moshi_8

Shape	Shape Code	Point Group	CShM
Hexagon	HP-6	D_{6h}	31.22205
Pentagonal Pyramid	PPY-6	C_{5v}	28.56046
Octahedron	OC-6	O_h	0.65158
Trigonal Prism	TPR-6	D_{3h}	15.69996
Johnson Pentagonal Pyramid	JPPY-6	C_{5v}	31.23117

Table S13. SHAPE Analysis for Ga3 in Dy_2moshi_8

Shape	Shape Code	Point Group	CShM
Hexagon	HP-6	D_{6h}	31.27522
Pentagonal Pyramid	PPY-6	C_{5v}	28.60668
Octahedron	OC-6	O_h	0.48765
Trigonal Prism	TPR-6	D_{3h}	15.87419
Johnson Pentagonal Pyramid	JPPY-6	C_{5v}	31.59006

Table S14. SHAPE Analysis for Ga4 in Dy_2moshi_8

Shape	Shape Code	Point Group	CShM
Hexagon	HP-6	D_{6h}	31.98234
Pentagonal Pyramid	PPY-6	C_{5v}	28.64919
Octahedron	OC-6	O_h	0.91569
Trigonal Prism	TPR-6	D_{3h}	16.52504
Johnson Pentagonal Pyramid	JPPY-6	C_{5v}	31.61303

Table S15. SHAPE Analysis for Ga5 in Dy_2moshi_8

Shape	Shape Code	Point Group	CShM
Hexagon	HP-6	D_{6h}	30.84541
Pentagonal Pyramid	PPY-6	C_{5v}	28.05878
Octahedron	OC-6	O_h	0.46023
Trigonal Prism	TPR-6	D_{3h}	15.68476
Johnson Pentagonal Pyramid	JPPY-6	C_{5v}	31.30620

Table S16. SHAPE Analysis for Ga6 in Dy_2moshi_8

Shape	Shape Code	Point Group	CShM
Hexagon	HP-6	D_{6h}	32.05544
Pentagonal Pyramid	PPY-6	C_{5v}	28.64493
Octahedron	OC-6	O_h	0.94096
Trigonal Prism	TPR-6	D_{3h}	16.38985
Johnson Pentagonal Pyramid	JPPY-6	C_{5v}	31.78561

Table S17. SHAPE Analysis for Ga7 in Dy_2moshi_8

Shape	Shape Code	Point Group	CShM
Hexagon	HP-6	D_{6h}	31.16155
Pentagonal Pyramid	PPY-6	C_{5v}	28.09224
Octahedron	OC-6	O_h	0.62507
Trigonal Prism	TPR-6	D_{3h}	16.03971
Johnson Pentagonal Pyramid	JPPY-6	C_{5v}	31.44990

Table S18. SHAPE Analysis for Ga8 in Dy_2moshi_8

Shape	Shape Code	Point Group	CShM
Hexagon	HP-6	D_{6h}	31.77686
Pentagonal Pyramid	PPY-6	C_{5v}	28.62759
Octahedron	OC-6	O_h	0.62700
Trigonal Prism	TPR-6	D_{3h}	15.80307
Johnson Pentagonal Pyramid	JPPY-6	C_{5v}	31.29639

2. Thermogravimetric analysis

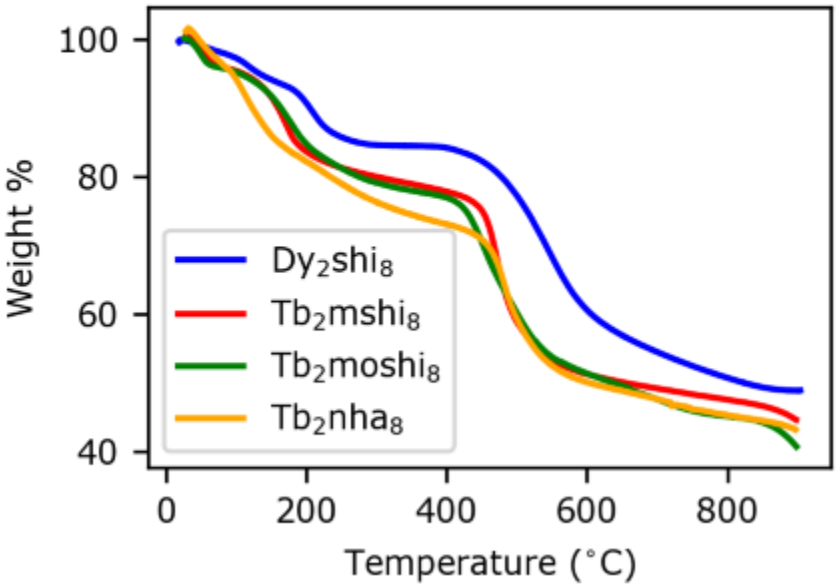

Figure S12. Thermogravimetric curves collected for $Tb_2L'_8$ MCs (L' = $moshi^{3-}$, $mshi^{3-}$, nha^{3-}) from 25 ºC to 900 ºC under N_2 atmosphere. The thermogravimetric curve for Dy_2shi_8 was collected previously and is included here for comparison.[1]

3. Photophysical Analysis

Table S19. Ln^{3+}-centered quantum yields (Q^L_{Ln}) in the near-infrared range measured for $Sm_2L'_8$ MCs (L' = shi^{3-}, $moshi^{3-}$, $mshi^{3-}$, nha^{3-}) in the solid state.[a]

MC	Q^L_{Ln} (%) : NIR
Sm_2shi_8	0.269(3) [b,c]
Sm_2mshi_8	0.116(2) [c]
Sm_2moshi_8	0.114(4) [c]
Sm_2nha_8	- [d]

[a] At room temperature, 2σ values between parentheses. [b] From Ref.[1] [c] Under excitation at 350 nm. [d] Could not be determined.

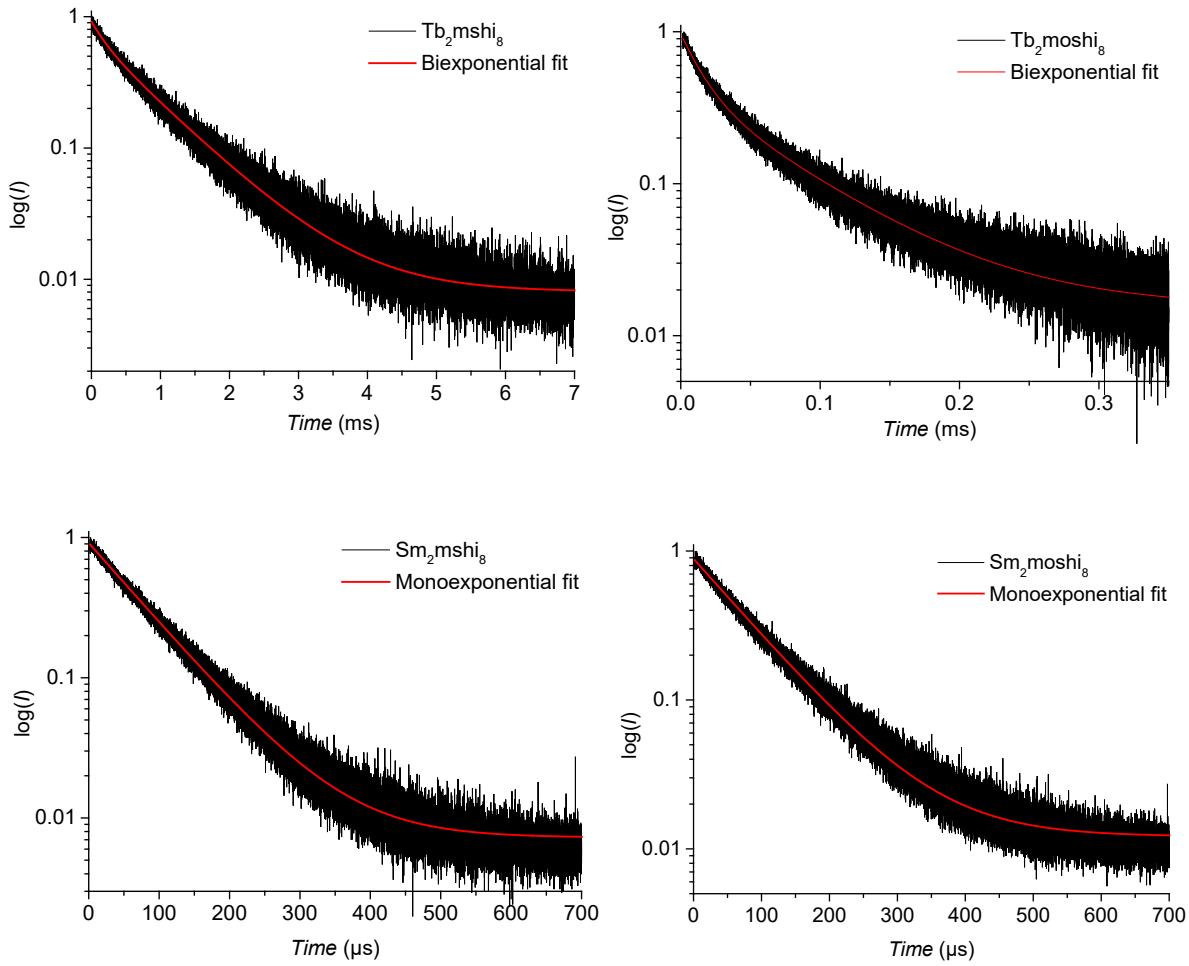

Figure S13. Experimental luminescence decay curves of Ln_2mshi_8 and Ln_2moshi_8 (Ln = Sm^{3+}, Tb^{3+}) in the solid state upon excitation at 355 nm and monitoring emission of Tb^{3+} at 545 nm or Sm^{3+} at 597 nm (black traces). Red traces correspond to mono- or bi-exponential fitting functions, $\chi^2 < 1.9 \cdot 10^{-4}$, $R^2 > 0.99$.

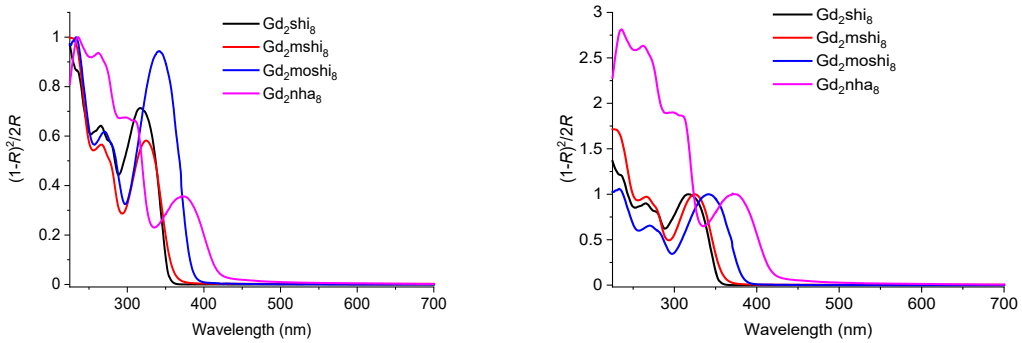

Figure S14. Diffuse reflectance spectra represented as a Kubelka–Munk function *vs.* wavelength of the $[Gd_2Ga_8(shi)_8(iph)_4](NH_4)_2$ and $[Gd_2Ga_8(L')_8(iph)_4]Na_2$ (L' = $mshi^{3-}$, $moshi^{3-}$, nha^{3-}) MCs (5 wt. % in MgO) at room temperature. Left: normalized to the maximum; right: normalized to the maximum of the lowest energy band at 317 nm, 325 nm, 341 nm or 375 nm for $[Gd_2Ga_8(shi)_8(iph)_4](NH_4)_2$, $[Gd_2Ga_8(mshi)_8(iph)_4]Na_2$, $[Gd_2Ga_8(moshi)_8(iph)_4]Na_2$ or $[Gd_2Ga_8(nap)_8(iph)_4]Na_2$, respectively. The spectra on the right is re-presented here (in addition to being provided in the main text) for clarity.

Table S20. Maxima of the lowest energy diffuse reflectance band (**Figure S14**) for $Gd_2L'_8$ MCs (L' = shi^{3-}, $moshi^{3-}$, $mshi^{3-}$, nha^{3-}).

MC	Maximum (nm)
Gd_2shi_8	317
Gd_2mshi_8	325
Gd_2moshi_8	341
Gd_2nha_8	375

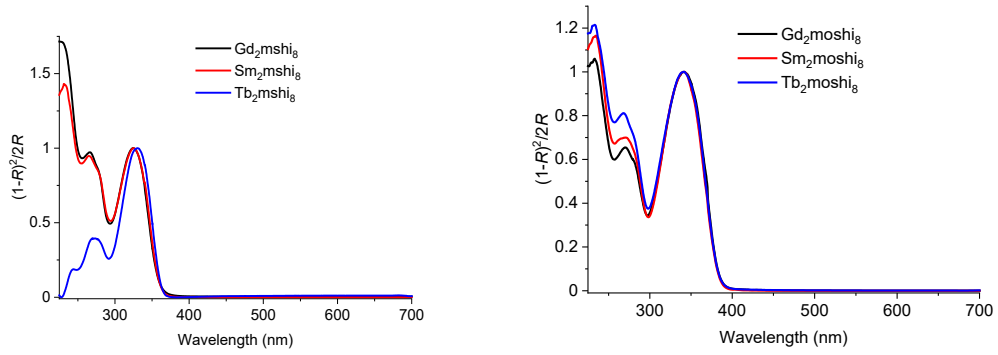

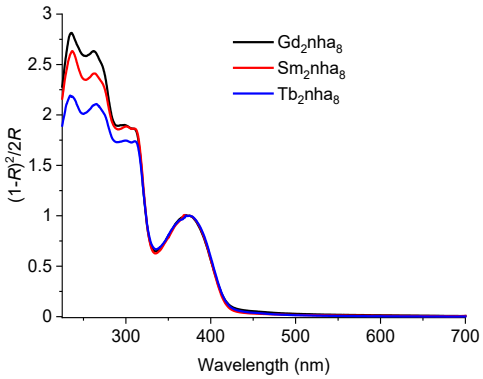

Figure S15. Diffuse reflectance spectra represented as a Kubelka–Munk function *vs.* wavelength of the $[Ln_2Ga_8(shi)_8(iph)_4](NH_4)_2$ and $[Ln_2Ga_8(L')_8(iph)_4]Na_2$ (L' = $mshi^{3-}$, $moshi^{3-}$, nha^{3-}) MCs (5 wt. % in MgO) normalized to the maximum of the lowest energy band at 317 nm, 325 nm, 341 nm or 375 nm for $[Ln_2Ga_8(shi)_8(iph)_4](NH_4)_2$, $[Ln_2Ga_8(mshi)_8(iph)_4]Na_2$, $[Ln_2Ga_8(moshi)_8(iph)_4]Na_2$ or $[Ln_2Ga_8(nap)_8(iph)_4]Na_2$, respectively, at room temperature. Ln = Gd^{3+}, Sm^{3+}, Tb^{3+}.

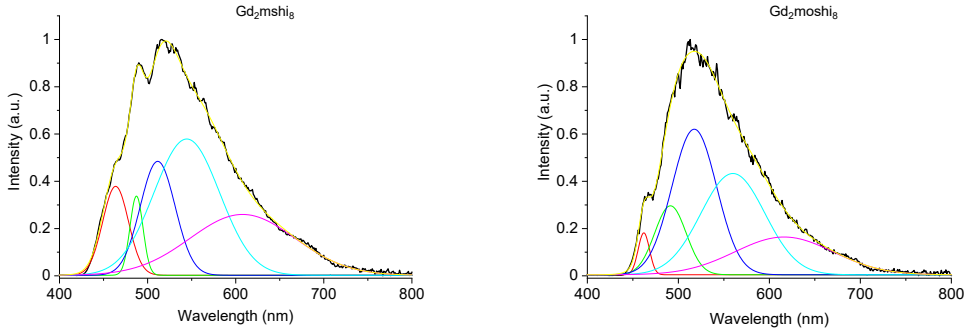

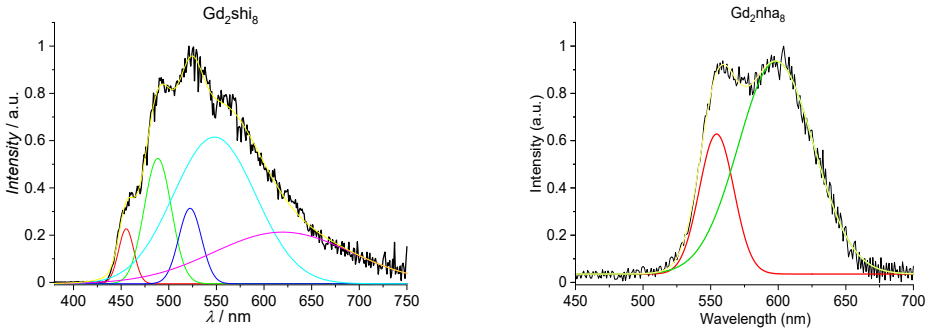

Figure S16. Phosphorescence spectra of $Gd_2L'_8$ MCs (L' = shi^{3-}, $moshi^{3-}$, $mshi^{3-}$, nha^{3-}) collected at 77K in the solid state.

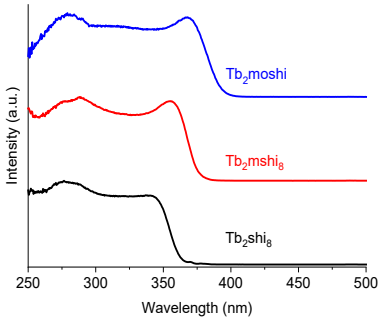

Figure S17. Corrected and normalized excitation spectra collected upon monitoring the emission at 545 nm ($^5D_4 \rightarrow {}^7F_5$ transition) upon excitation at 340 nm for $Tb_2L'_8$ MCs (L' = shi^{3-}, $moshi^{3-}$, $mshi^{3-}$) in the solid state at room temperature.

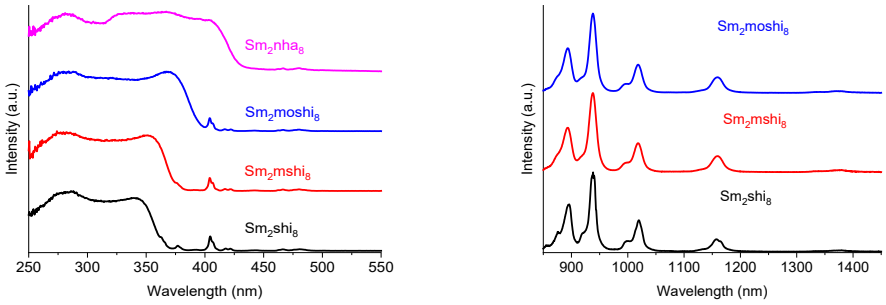

Figure S18. Corrected and normalized (left) excitation spectra upon monitoring emission at 597 nm ($^4G_{5/2} \rightarrow {}^6H_{7/2}$ transition) and (right) near-infrared emission spectra upon excitation at 340–370 nm for $Sm_2L'_8$ (L' = shi^{3-}, $mshi^{3-}$, $moshi^{3-}$, nha^{3-}) in the solid state at room temperature.

4. Thermal Dependence of Emission

Table S21. Luminescence lifetimes of Tb_2moshi_8, Sm_2moshi_8 and Tb_2moshi_8:Sm_2moshi_8 (1:1) in the solid state at several different temperatures. [a]

MC	*T*, K	Level	τ_1, µs	τ_2, µs	τ_{av}, µs[b]
Tb_2moshi_8	298	$^5D_4$	69.0(8): 75(2)%	16.2(5): 25(2)%	65.2
Tb_2moshi_8 : Sm_2moshi_8	298	$^5D_4$	54.3(1) : 72.0(3)%	9.6(2) : 28.0(3)%	51.5
Sm_2moshi_8	298	$^4G_{5/2}$	89(2)		
Tb_2moshi_8 : Sm_2moshi_8	298	$^4G_{5/2}$	79(1)		
Tb_2moshi_8	273	$^5D_4$	112(7) : 69(1)%	26(1) : 31(1)%	104
Tb_2moshi_8 : Sm_2moshi_8	273	$^5D_4$	56(1) : 81(1)%	10.2(1) : 19(1)%	53.8
Sm_2moshi_8	273	$^4G_{5/2}$	86.8(7)		
Tb_2moshi_8 : Sm_2moshi_8	273	$^4G_{5/2}$	95(1)		
Tb_2moshi_8	250	$^5D_4$	224(5) : 81(2)%	42.1(1) : 19(2)%	216
Tb_2moshi_8 : Sm_2moshi_8	250	$^5D_4$	143(7) : 83(3)%	23.8(1) : 17(3)%	139
Sm_2moshi_8	250	$^4G_{5/2}$	84.6(5)		
Tb_2moshi_8 : Sm_2moshi_8	250	$^4G_{5/2}$	95(1)		
Tb_2moshi_8	220	$^5D_4$	580(9) : 86(2)%	97(1) : 14(2)%	568
Tb_2moshi_8 : Sm_2moshi_8	220	$^5D_4$	422(3) : 82(2)%	64(4) : 18(2)%	411
Sm_2moshi_8	220	$^4G_{5/2}$	85(2)		
Tb_2moshi_8 : Sm_2moshi_8	220	$^4G_{5/2}$	96(2)		

Tb_2moshi_8	170	$^5D_4$	1040(1) : 88.3(2)%	150(1) : 11.7(2)%	1020
Tb_2moshi_8 : Sm_2moshi_8	170	$^5D_4$	979(3) : 86.5(8)%	134(3) : 13.5(8)%	961
Sm_2moshi_8	170	$^4G_{5/2}$	83.1(8)		
Tb_2moshi_8 : Sm_2moshi_8	170	$^4G_{5/2}$	92.4(5)		
Tb_2moshi_8	120	$^5D_4$	1110(40) : 88.8(8)%	167(8) : 11.2(8)%	1090
Tb_2moshi_8 : Sm_2moshi_8	120	$^5D_4$	1170(20) : 90(1)%	180(6) : 10(1)%	1160
Sm_2moshi_8	120	$^4G_{5/2}$	80.7(8)		
Tb_2moshi_8 : Sm_2moshi_8	120	$^4G_{5/2}$	91(1)		

[a] Under excitation at 355 nm; 2σ values between parentheses. Estimated experimental error: τ_{obs}, ±2%. If a biexponential decay was observed, population parameters $P_i = \frac{B_i\tau_i}{\sum_{i=1}^{n} B_i\tau_i}$ in % are given after the colon. [b] Average lifetime calculated using the formula: $\tau_{av} = \frac{\sum_i B_i\tau_i^2}{\sum_i B_i\tau_i}$. [c]

For measurements of luminescence lifetimes of Ln_2moshi_8 MCs at different temperatures, samples were placed into a closed-cycle Sumitomo cryostat (Janis Research CCS-500/204). The temperature was controlled by a LakeShore temperature controller (Model 331). Luminescence lifetimes were determined under excitation at 355 nm provided by a Nd:YAG laser (YG 980; Quantel), the signals in the visible at 490 nm (Tb, $^5D_4$ level) and at 700 nm (Sm, $^4G_{5/2}$ level) were detected by a Hamamatsu R928 PMT connected to an iHR320 monochromator (Horiba Scientific). The output signals from the detector were fed into a 500 MHz bandpass digital oscilloscope (TDS 754C; Tektronix) and transferred to a PC for data processing using Origin 8® software. Luminescence lifetimes are averages of three independent measurements.

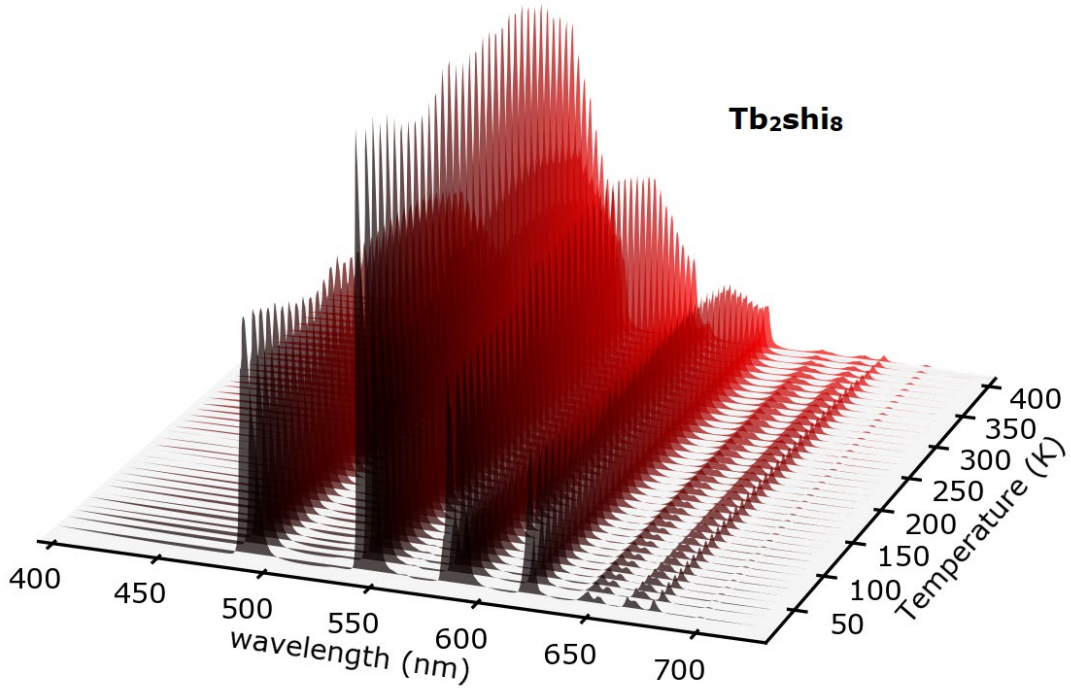

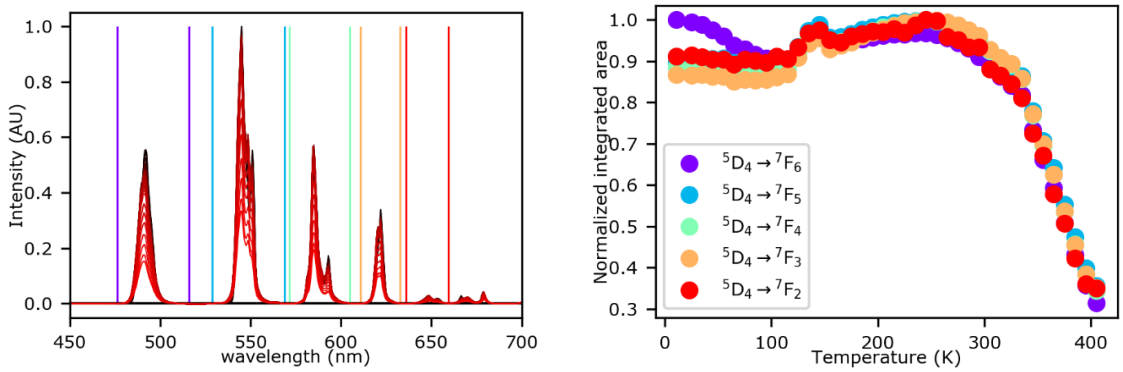

Figure S19. Temperature-dependent emission spectra of Tb_2shi_8 upon excitation at 340 nm. The data are presented as a 3D plot in the top panel, and as a 2D plot in the bottom left panel. Black = 11 K and red = 400 K. The bottom left panel also shows integration bounds (colored vertical lines) corresponding to the figure in the bottom right panel. Bottom right: Normalized integrated intensities of Tb^{3+} $^5D_4 \rightarrow {}^7F_J$ (J = 6–0) transitions *vs*. temperature. Integration bounds for each transition of Tb^{3+} are presented as colored vertical lines in the bottom left panel.

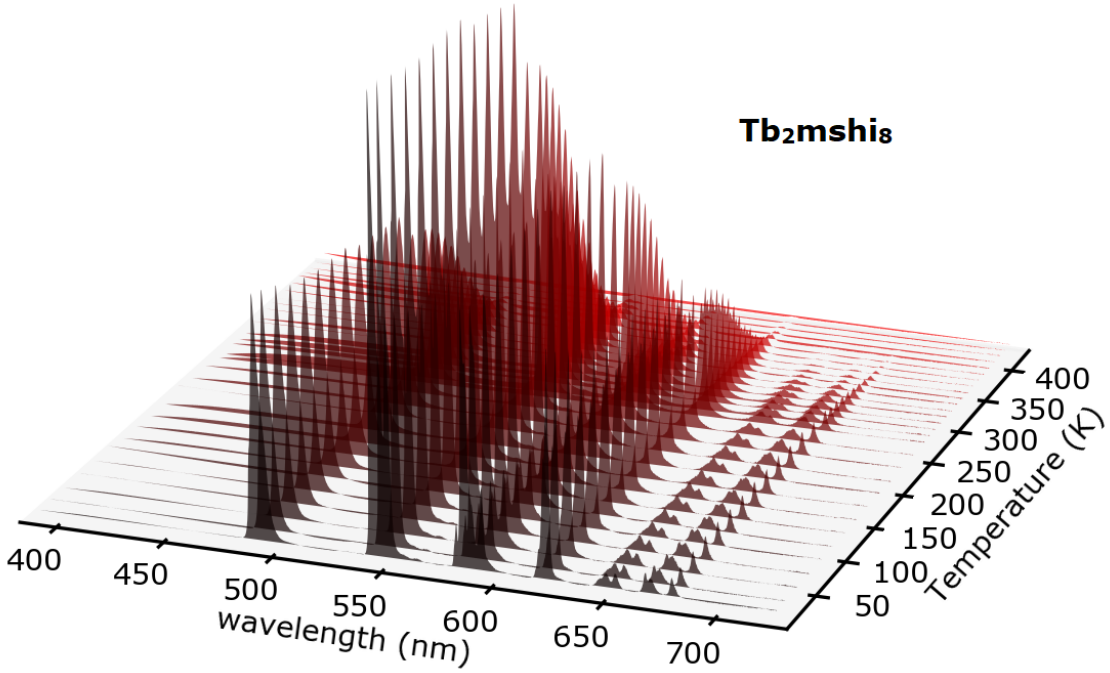

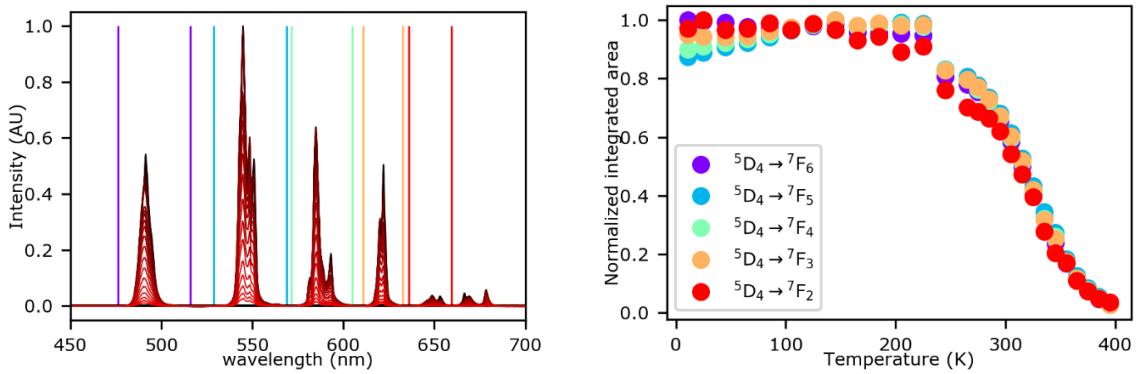

Figure S20. Temperature-dependent emission spectra of Tb_2mshi_8 upon excitation at 350 nm. The data are presented as a 3D plot in the top panel, and as a 2D plot in the bottom left panel. Black = 11 K and red = 400 K. The bottom left panel also shows integration bounds (colored vertical lines) corresponding to the figure in the bottom right panel. Bottom right: Normalized integrated intensities of Tb^{3+} $^5D_4 \rightarrow {}^7F_J$ (J = 6–0) transitions *vs*. temperature. Integration bounds for each transition of Tb^{3+} are presented as colored vertical lines in the bottom left panel.

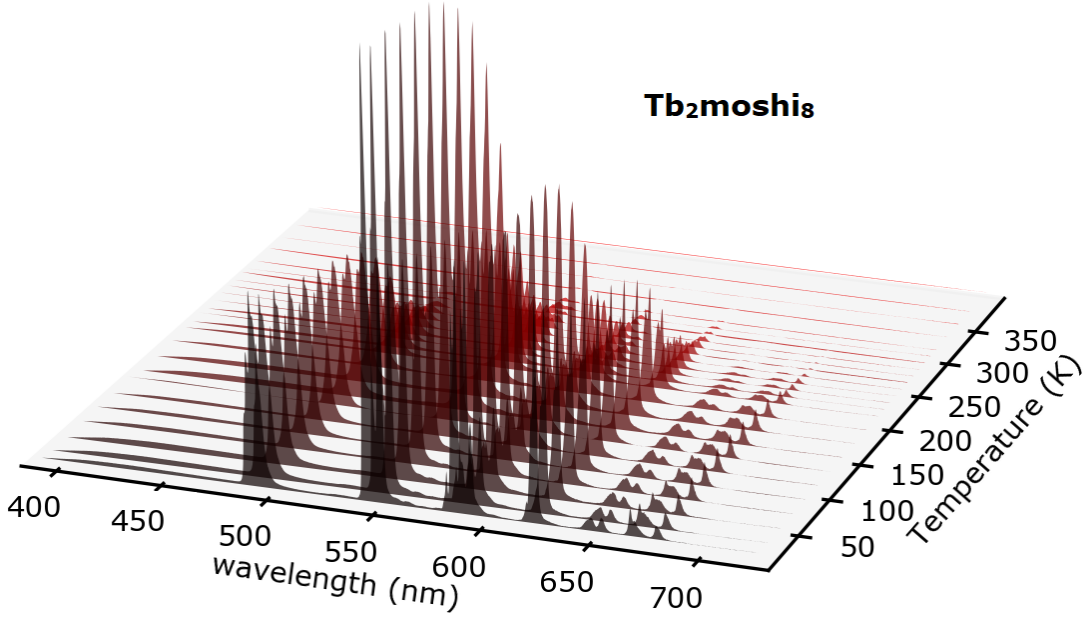

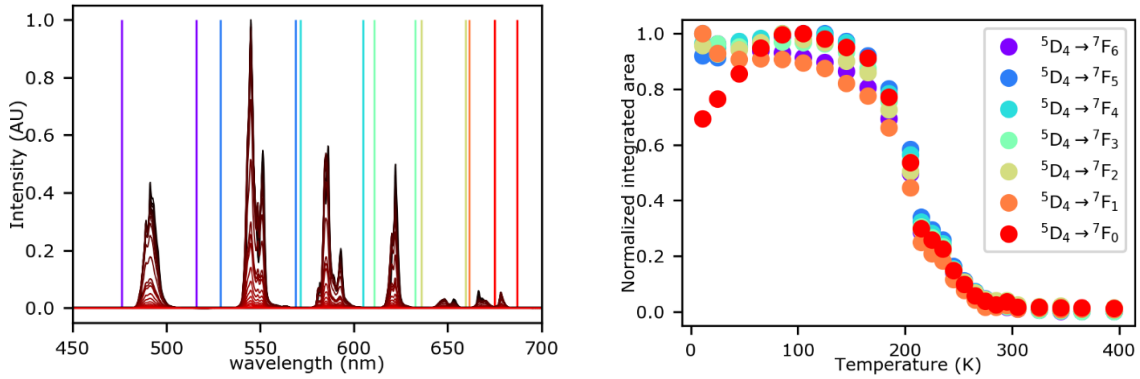

Figure S21. Temperature-dependent emission spectra for Tb_2moshi_8 collected under excitation at 370 nm. The data are presented as a 3D plot in the top panel, and as a 2D plot in the bottom left panel. Black = 11 K and red = 400 K. The bottom left panel also shows integration bounds (colored vertical lines) corresponding to the figure in the bottom right panel. Bottom right: Normalized integrated intensities of Tb^{3+} $^5D_4 \rightarrow {}^7F_J$ (J = 6–0) transitions *vs.* temperature. Integration bounds for each transition of Tb^{3+} are presented as colored vertical lines in the bottom left panel.

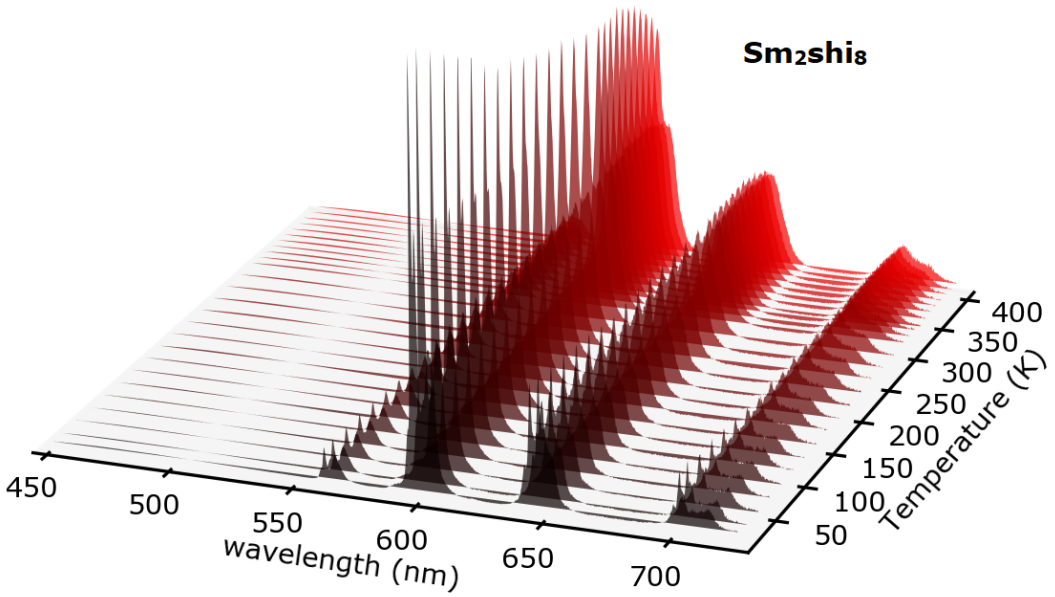

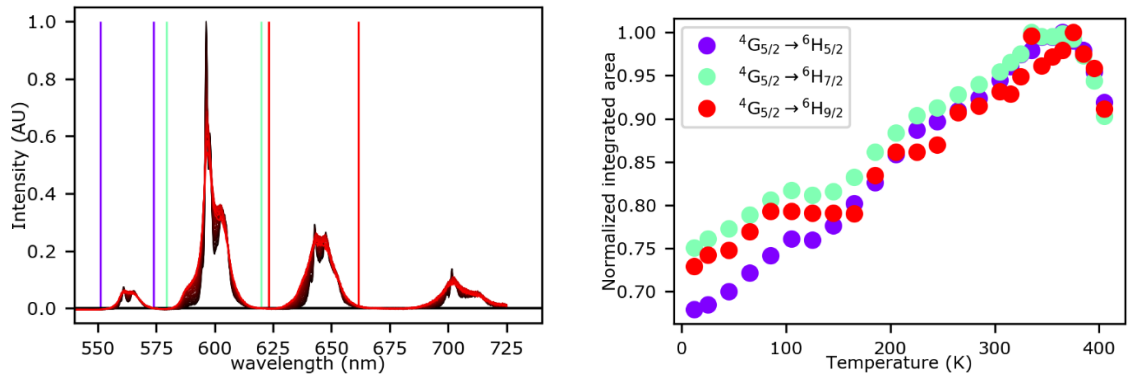

Figure S22. Temperature-dependent emission spectra for Sm_2shi_8 collected upon excitation at 340 nm. The data are presented as a 3D plot in the top panel, and as a 2D plot in the bottom left panel. Black = 11 K and red = 400 K. The bottom left panel also shows integration bounds (colored vertical lines) corresponding to the figure in the bottom right panel. Bottom right: Normalized integrated intensities of Sm^{3+} $^4G_{5/2} \rightarrow {}^6H_J$ (J = 9/2–5/2) transitions *vs.* temperature. Integration bounds for each transition of Sm^{3+} are presented as colored vertical lines in the bottom left panel.

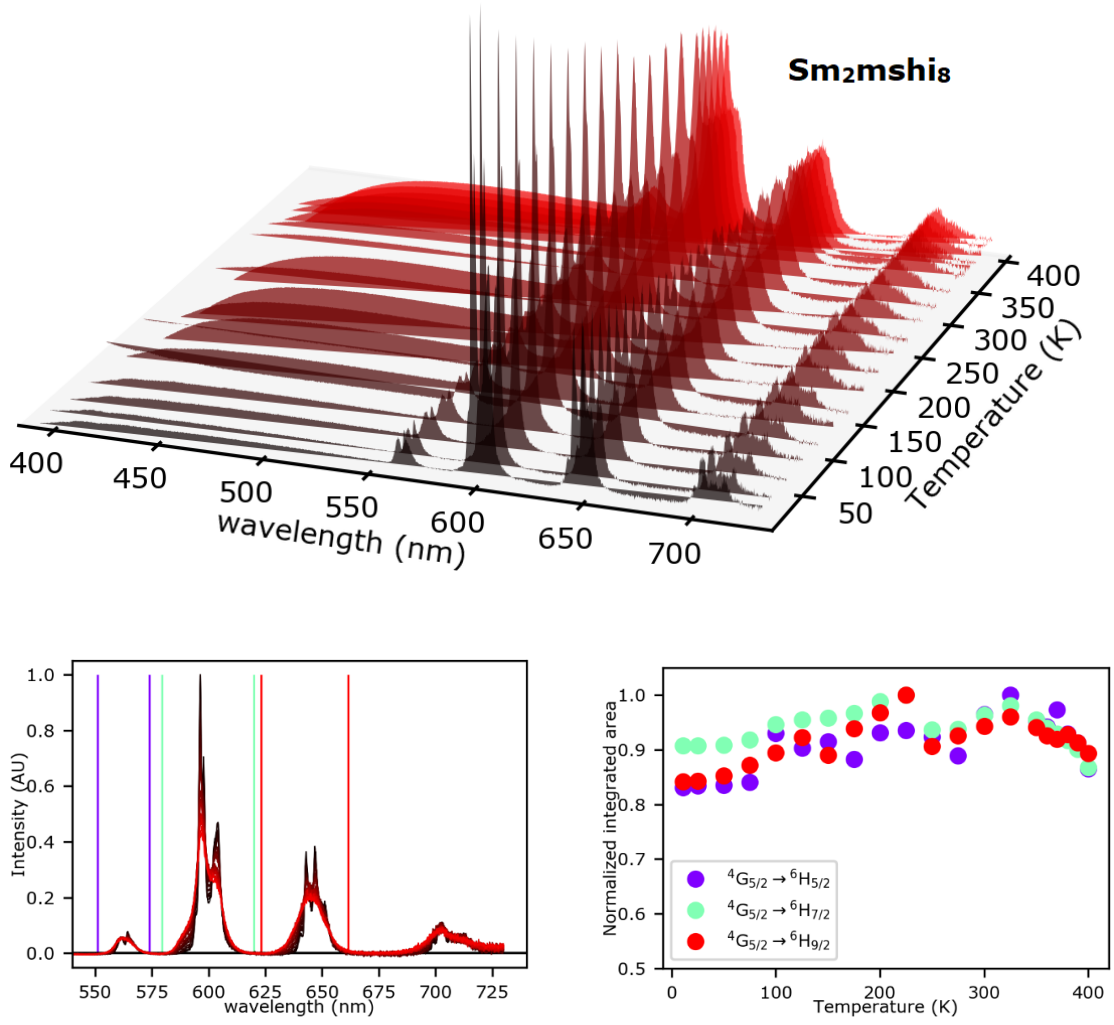

Figure S23. Temperature-dependent emission spectra for Sm_2mshi_8 collected upon excitation at 350 nm. The data are presented as a 3D plot in the top panel, and as a 2D plot in the bottom left panel. Black = 11 K and red = 400 K. The bottom left panel also shows integration bounds (colored vertical lines) corresponding to the figure in the bottom right panel. Bottom right: Normalized integrated intensities of Sm^{3+} $^4G_{5/2} \rightarrow {}^6H_J$ ($J = 9/2–5/2$) transitions *vs.* temperature. Integration bounds for each transition of Sm^{3+} are presented as colored vertical lines in the bottom left panel.

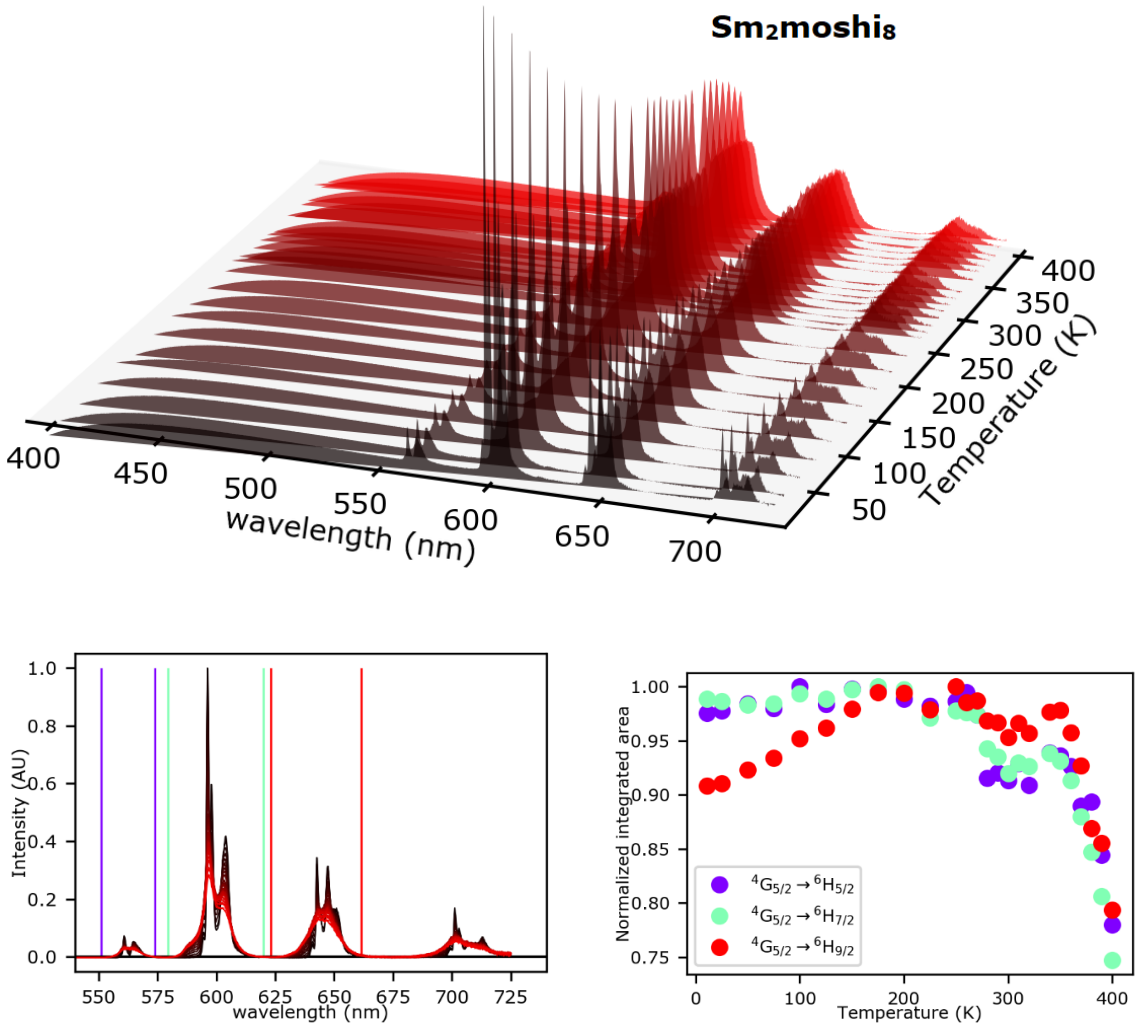

Figure S24. Temperature-dependent emission spectra for Sm_2moshi_8 collected upon excitation at 370 nm. The data are presented as a 3D plot in the top panel, and as a 2D plot in the bottom left panel. Black = 11 K and red = 400 K. The bottom left panel also shows integration bounds (colored vertical lines) corresponding to the figure in the bottom right panel. Bottom right: Normalized integrated intensities of Sm^{3+} $^4G_{5/2} \rightarrow {}^6H_J$ ($J = 9/2–5/2$) transitions *vs.* temperature. Integration bounds for each transition of Sm^{3+} are presented as colored vertical lines in the bottom left panel.

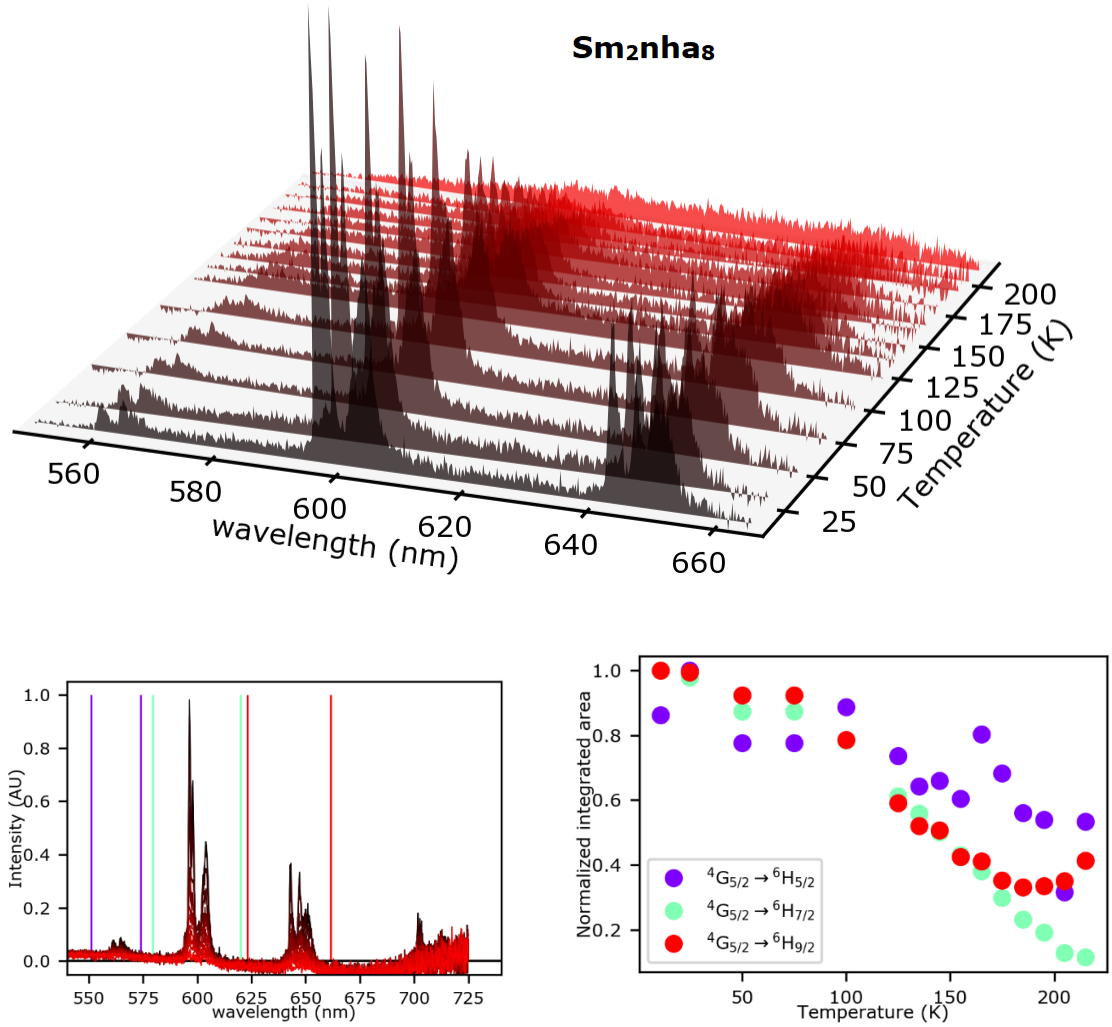

Figure S25. Temperature-dependent emission spectra for Sm_2nha_8 collected upon excitation at 380 nm. The data are presented as a 3D plot in the top panel, and as a 2D plot in the bottom left panel. Black = 11 K and red = 400 K. The bottom left panel also shows integration bounds (colored vertical lines) corresponding to the figure in the bottom right panel. Bottom right: Normalized integrated intensities of Sm^{3+} $^4G_{5/2} \rightarrow {}^6H_J$ ($J = 9/2–5/2$) transitions *vs.* temperature. Integration bounds for each transition of Sm^{3+} are presented as colored vertical lines in the bottom left panel. All transitions are expected to have similar thermal dependence, the discrepancies are likely due to the difficulty in establishing an ideal background due to the low signal-to-noise ratio (**Figure S26**). The presented data are truncated for these reasons.

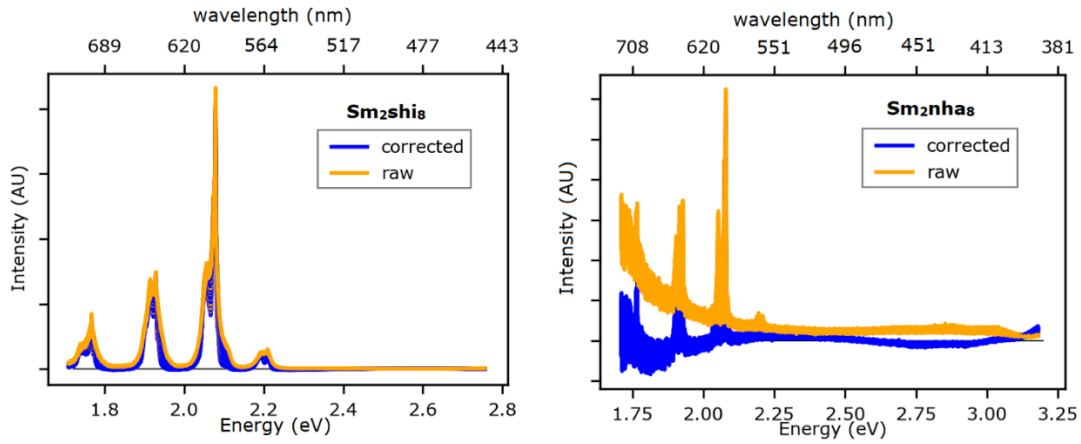

Figure S26. An example of the emission spectra prior (orange) and after (blue) correcting data for the baseline drift. Data are converted to eV for the baseline correction and integration because it is a linear scale to energy. All the thermal traces are provided as an overlay. Left: data for Sm_2shi_8 are provided as a typical baseline correction example. Right: Owing to the low-intensity of Sm^{3+} emission in the Sm_2nha_8 sample and the relatively low signal to noise ratio, correcting this dataset is more difficult than for the other ones. The procedure was optimized to create a flat baseline around Sm^{3+} transitions in the range 550–660 nm, and in particular around the $^4G_{5/2} \rightarrow {}^6H_{7/2}$ transition at ca. 600 nm.

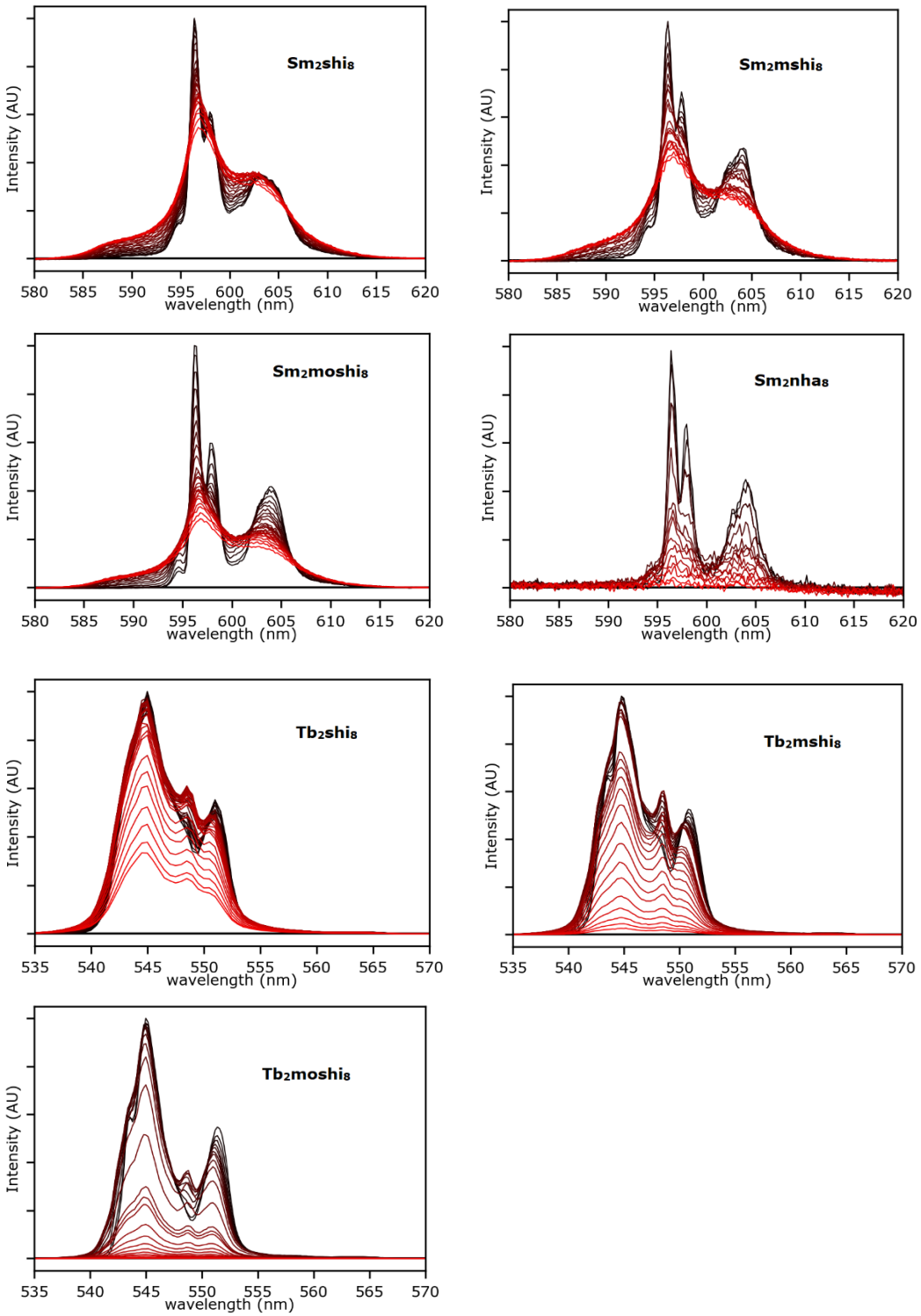

Figure S27. Temperature-dependent emission spectra focusing on the Tb^{3+} $^5D_4 \rightarrow {}^7F_5$ transition for $Tb_2L'_8$ MCs and the Sm^{3+} $^4G_{5/2} \rightarrow {}^6H_{7/2}$ transition for $Sm_2L'_8$ MCs. Black = 11 K → red = 400 K (210 K for Sm_2nha_8).

5. Thermometric behavior

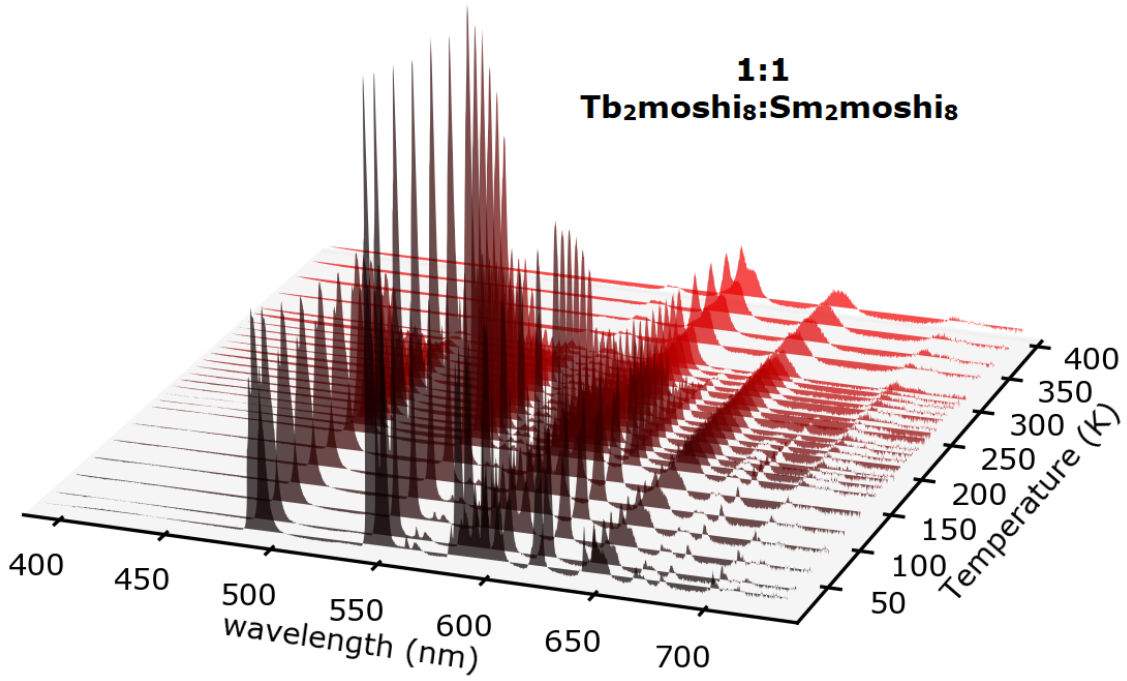

Figure S28. Temperature-dependent emission spectra collected for a 1:1 mixture of Tb_2moshi_8:Sm_2moshi_8 upon excitation at 370 nm.

Table S22. Parameters obtained by fitting the single-pathway component Mott–Seitz function (**eqn 1**) to the Δ parameters specified in a 1:1 mixture of Tb_2moshi_8:Sm_2moshi_8.

	Δ [$^5D_4 \rightarrow {}^7F_5/{}^4G_{5/2} \rightarrow {}^6H_{9/2}$]	Δ [$^5D_4 \rightarrow {}^7F_6/{}^4G_{5/2} \rightarrow {}^6H_{9/2}$]	Δ [$^5D_4 \rightarrow {}^7F_3/{}^4G_{5/2} \rightarrow {}^6H_{9/2}$]
a_1	14908.52	3715.91	15475.61
E_1	1407.4 cm^{-1}	1160.57 cm^{-1}	1396.23 cm^{-1}
Δ_o	6.22	3.61	1.36
r^2	0.992	0.987	0.993

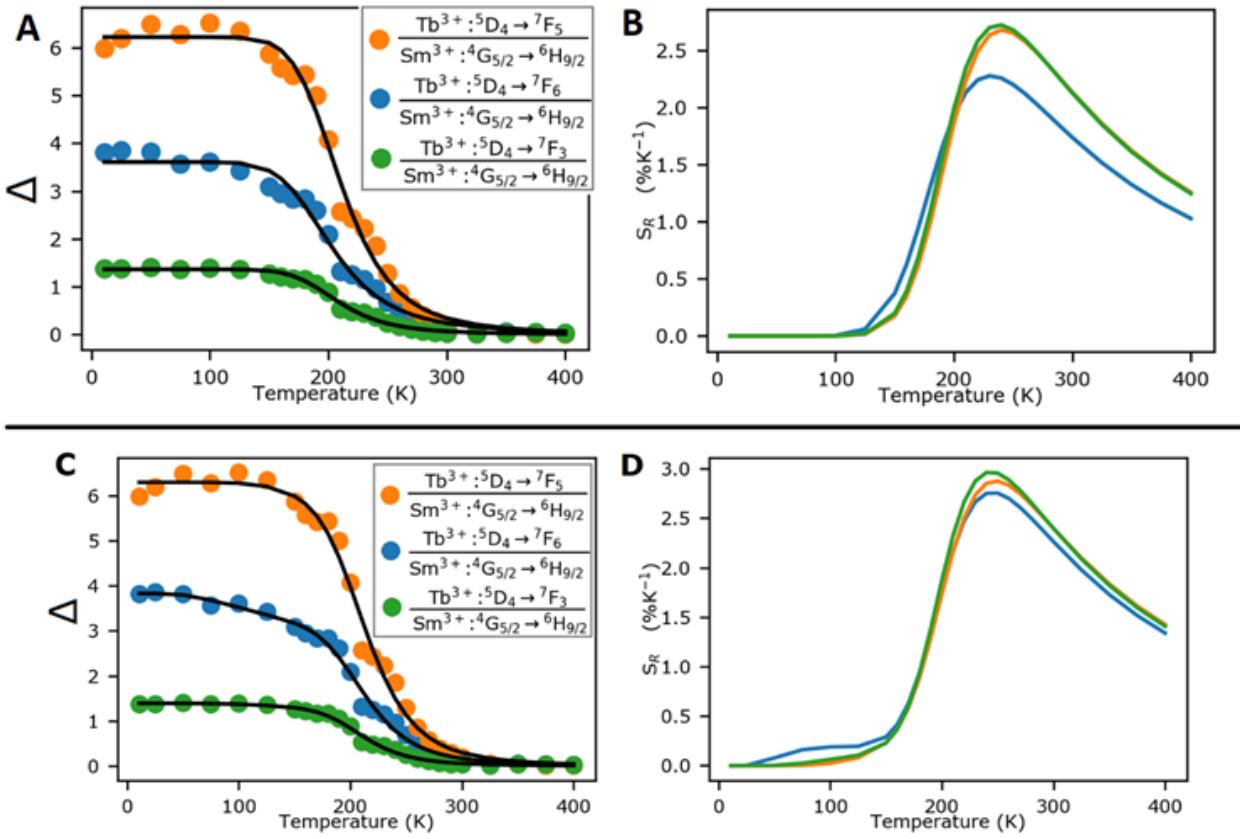

Figure S29. Comparison between two fitting models for the thermal dependence of the emission intensity of a 1:1 mixture of Tb_2moshi_8:Sm_2moshi_8. The top one is a single component model (**eqn 1**) while the bottom one is a dual component model (**eqn S1**). **A**: The Δ parameter is obtained by taking the fraction specified in the legend for each temperature with an integration corresponding to **Figure 7 B.** The fit for each curve is overlaid in black (**eqn 1**). This is identical to **Figure 7 C. B**: The relative sensitivity for each Δ parameter in panel A calculated from **eqn 2**. This is identical to **Figure 7 D. C**: The Δ parameter is obtained by taking the fraction specified in the legend for each temperature with an integration corresponding to **Figure 7 B.** The fit for each curve is overlaid in black (dual Mott–Seitz model, **eqn S1**). **D**: The relative sensitivity for each Δ parameter in panel C calculated from **eqn 2**.

Dual-component Mott–Seitz equation:

$$\Delta = \frac{\Delta_o}{1 + a_1 * e^{\frac{-E_1}{k_B T}} + a_2 * e^{\frac{-E_2}{k_B T}}} \qquad \textbf{eqn S1}$$

Table S23. Parameters obtained by fitting the dual-pathway component Mott–Seitz function (**eqn S1**) to the Δ parameters specified in a 1:1 mixture of Tb_2moshi_8:Sm_2moshi_8.

	Δ [$^5D_4 \rightarrow {}^7F_5/{}^4G_{5/2} \rightarrow {}^6H_{9/2}$]	Δ [$^5D_4 \rightarrow {}^7F_6/{}^4G_{5/2} \rightarrow {}^6H_{9/2}$]	Δ [$^5D_4 \rightarrow {}^7F_3/{}^4G_{5/2} \rightarrow {}^6H_{9/2}$]
a_1	43469.04	29395.31	44647.20
E_1	1601.42 cm^{-1}	1502.01 cm^{-1}	1574.93 cm^{-1}
a_2	9.36	0.91	1.29
E_2	560.39 cm^{-1}	162.48 cm^{-1}	312.66 cm^{-1}
Δ_o	6.29	3.83	1.39
r^2	0.992	0.994	0.994

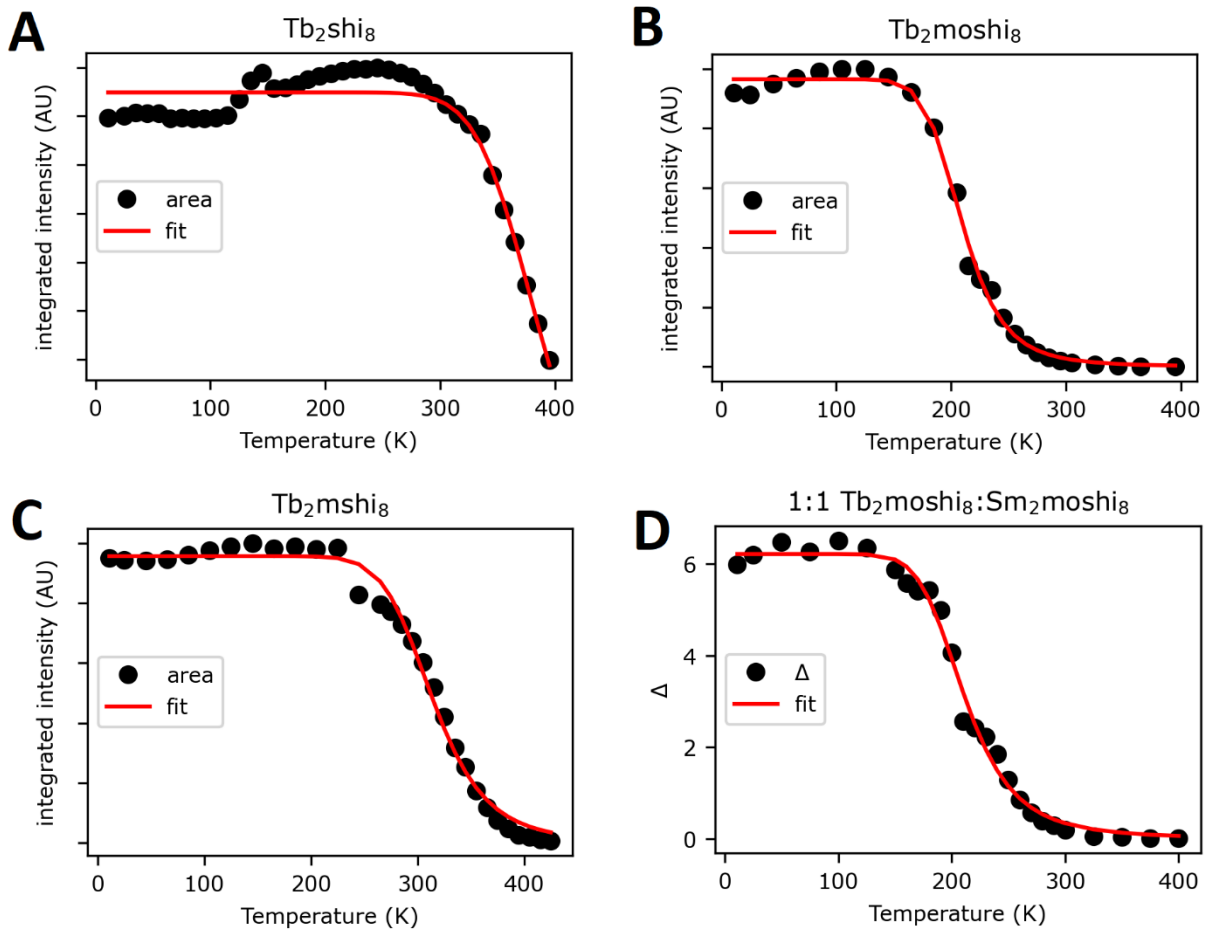

Figure S30. A, B, C: The integrated intensity area of the Tb^{3+} $^5D_4 \rightarrow {}^7F_5$ transition in $Tb_2L'_8$ ($L' = shi^{3-}$, $mshi^{3-}$, $moshi^{3-}$) compounds (black circles) as a function of temperature, together with a single-component Mott-Seitz function fitting (**eqn 1**). These are compared with the Δ parameter of 1:1 Tb_2moshi_8:Sm_2moshi_8 (**D**) as dictated in **Figure 7**, where $\Delta = I_{Tb}/I_{Sm}$, I_{Tb} is the integrated intensity of the Tb^{3+} $^5D_4 \rightarrow {}^7F_5$ transition and I_{Sm} is the integrated intensity of the Sm^{3+} $^4G_{5/2} \rightarrow {}^6H_{9/2}$ transition. The behavior of the thermometer is dictated mostly by the thermal response of Tb^{3+}. These fitting parameters are gathered in **Table S24**.

Table S24. Parameters obtained by fitting the single-pathway component Mott–Seitz function (**eqn 1**) to the Δ parameters specified in $Tb_2L'_8$, and in a 1:1 mixture of Tb_2moshi_8:Sm_2moshi_8.

	Tb_2shi_8 $^5D_4 \rightarrow {}^7F_5$	Tb_2mshi_8 $^5D_4 \rightarrow {}^7F_5$	Tb_2moshi_8 $^5D_4 \rightarrow {}^7F_5$	Tb_2moshi_8:Sm_2moshi_8 Δ [$^5D_4 \rightarrow {}^7F_5/{}^4G_{5/2} \rightarrow {}^6H_{9/2}$]
a_1	1201017.43	275446.58	134935.67	14908.52
E_1	3742.08 cm^{-1}	2737.56 cm^{-1}	1721.39 cm^{-1}	1407.4 cm^{-1}
Δ_o	1.90	0.96	0.96	6.22
r^2	0.937	0.991	0.996	0.992

6. Theoretical modeling methodology

6.1 Theoretical intensity parameters

The forced electric dipole (FED–Judd–Ofelt theory) and dynamic coupling (DC) are the dominant mechanisms controlling the emission intensities related to the 4*f*–4*f* transitions when the Ln^{3+} occupies a non-centrosymmetric coordination site.[4–6] The theoretical expressions here used for the intensity parameters, Ω_λ^{theo}, have been described in detail in several references.[7–9]

$$\Omega_\lambda^{theo} = (2\lambda+1)\sum_{t,p}\frac{|B_{\lambda tp}|^2}{2t+1} \quad , \quad B_{\lambda tp} = B_{\lambda tp}^{FED} + B_{\lambda tp}^{DC} \qquad \textbf{eqn S2}$$

where,

$$B_{\lambda tp}^{FED} = \frac{2}{\Delta E}\langle r^{t+1}\rangle\Theta(t,\lambda)\left(\frac{4\pi}{2t+1}\right)^{\frac{1}{2}}\sum_j \frac{e^2\rho_j g_j(2\beta_j)^{t+1}}{R_j^{t+1}}\left(Y_p^{t*}\right)_j \qquad \textbf{eqn S3}$$

$$B_{\lambda tp}^{DC} = -\left[\frac{(\lambda+1)(2\lambda+3)}{(2\lambda+1)}\right]^{\frac{1}{2}}\langle r^\lambda\rangle\langle f\|C^{(\lambda)}\|f\rangle\left(\frac{4\pi}{2t+1}\right)^{\frac{1}{2}} \times\sum_j \frac{\left[(2\beta_j)^{t+1}\alpha_{OP,j}+\alpha'_j\right]}{R_j^{t+1}}\left(Y_p^{t*}\right)_j\delta_{t,\lambda+1} \qquad \textbf{eqn S4}$$

being t and p the ranks and components of the spherical harmonics $\left(Y_p^{t*}\right)$, $\langle f\|C^{(2)}\|f\rangle = -1.366$, $\langle f\|C^{(4)}\|f\rangle = 1.128$, and $\langle f\|C^{(6)}\|f\rangle = -1.27$. The ρ is the overlap integral between the valence subshells of the ligating atom and the 4*f* subshell of the lanthanide ion in the case of Ln^{3+}–O chemical bonds. These values have been obtained using the parametric approach from Ref.[10] $\beta = 1/(1\pm\rho)$ is a parameter that defines the centroid of the electronic density of the chemical bond Ln–X (X = ligating atom), α' is the effective polarizability from each ligand around the Ln^{3+}, and g is the charge factor. The **eqn S3** is the expression of the Simple Overlap Model (SOM) for the odd-ranked ligand field[11,12] while **eqn S4** is related to the Bond Overlap Model (BOM) for the Dynamic Coupling mechanism.[13,14]

The overlap polarizabilities α_{OP} are quantities related to the covalent fraction of a chemical bond,[13,15–17] defined as:

$$\alpha_{OP} = \frac{e^2 \rho^2 R^2}{2\Delta\varepsilon}$$ **eqn S5**

where e is the electron charge, R (equal to 2.40 Å in all cases) is the length of the bond Ln–O, and $\Delta\varepsilon$ is excitation energy associated with the chemical bond. The ρ and Δε values were obtained using the approach described in Ref.[10] Thus, we obtain values of α_{OP} = 4.28×10^{-3} and 3.82×10^{-3} Å^3 for Tb–O and Sm–O bonds, respectively.

The Ω_λ values, as well as the input data for the JOYSpectra program [18] (α' and g), are presented in **Table S25**. Each ligating atom label is the same as illustrated in **Figure S31**.

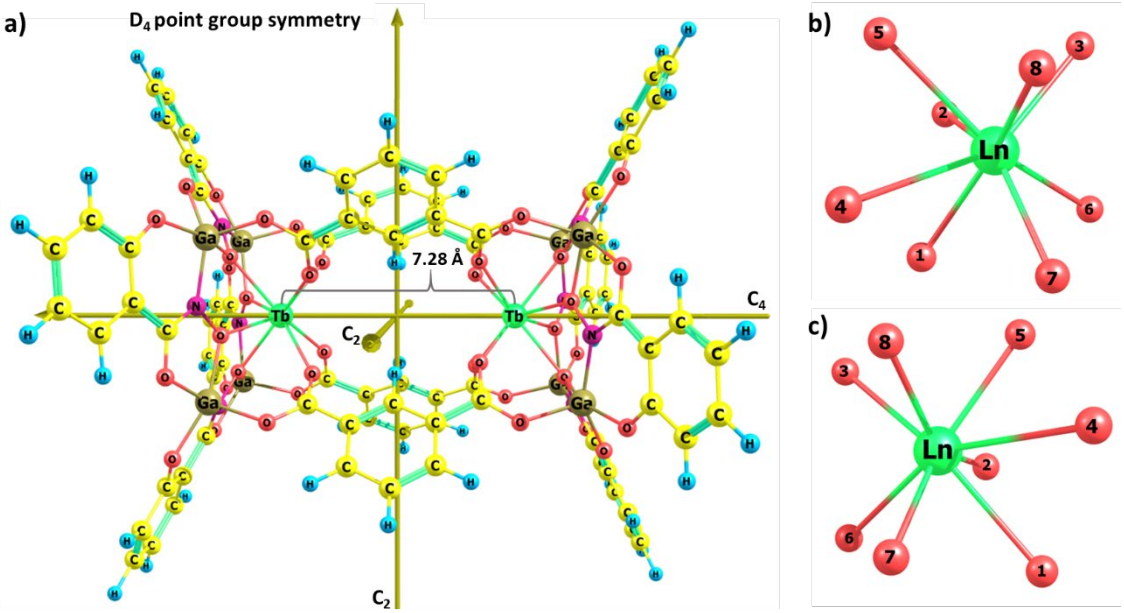

Figure S31. a) Tb_2shi_8 structure presenting a D_4 point group symmetry. The coordination spheres showing the arrangements of the ligating oxygen atoms for the b) left and c) right Ln^{3+} as presented in a). The labels follow the same indication as **Table S25.**

Table S25. Values of α' (in Å^3) and g (dimensionless) used for the calculation of Ω_λ (in 10^{-20} cm^2) for the Sm_2shi_8 and Tb_2shi_8 complexes. The FED contributions (which are the important ones for the energy transfer rates for the dipole–dipole mechanism) values are in parentheses. Due to the distinct chemical environments of the two ligands groups (O–Ga and O–C), the values of α' and g must differ.

LIGATING ATOM	LIGAND GROUP	α'	g
O_1	O–Ga	4.32	0.99
O_2	O–Ga	4.17	0.98
O_3	O–C	2.99	0.86
O_4	O–Ga	4.01	1.15
O_5	O–Ga	4.48	1.05
O_6	O–C	2.99	0.81
O_7	O–C	2.84	0.89
O_8	O–C	2.87	0.88
Sm_2shi_8		$\boldsymbol{\Omega_2}$ ($\boldsymbol{\Omega_2^{FED}}$)	2.30 (0.36)
		$\boldsymbol{\Omega_4}$ ($\boldsymbol{\Omega_4^{FED}}$)	10.34 (1.29)
		$\boldsymbol{\Omega_6}$ ($\boldsymbol{\Omega_6^{FED}}$)	6.71 (4.80)
Tb_2shi_8		$\boldsymbol{\Omega_2}$ ($\boldsymbol{\Omega_2^{FED}}$)	0.99 (0.20)
		$\boldsymbol{\Omega_4}$ ($\boldsymbol{\Omega_4^{FED}}$)	51.18 (0.46)
		$\boldsymbol{\Omega_6}$ ($\boldsymbol{\Omega_6^{FED}}$)	9.19 (1.46)

The calculated Ω_λ values in **Table S25** can be used for the other $Ln_2L'_8$ MCs with different ligands (L' = $mshi^{3-}$, $moshi^{3-}$, and nha^{3-}). This can be assumed once the theoretical intensity parameters depend mainly on the properties of the atoms in the first coordination sphere (sum over j in **eqns S3** and **S4**). Effects of long-range interactions in the intensity parameters are rarely observed.[19,20]

6.2 Ligand-to-Ln^{3+} energy transfer

The intramolecular energy transfer rates (IET) from the excited states S_1 and T_1 to the Ln^{3+} ion were calculated taking into account the dipole-dipole (W_{d-d}), dipole–multipole (W_{d-m}), and exchange (W_{ex}) mechanisms,[9,21]

$$W_{d-d} = \frac{S_L(1-\sigma_1)^2}{(2J+1)G}\frac{4\pi}{\hbar}\frac{e^2}{R_L^6}\sum_{\lambda}\Omega_K^{FED}\langle\psi' J'\|U^{(K)}\|\psi J\rangle^2 F \qquad \textbf{eqn S6}$$

$$W_{d-m} = \frac{S_L}{(2J+1)G}\frac{2\pi e^2}{\hbar}\sum_{K}(K+1)\frac{\langle r^K\rangle^2}{(R_L^{K+2})^2}\langle f\|C^{(K)}\|f\rangle^2(1-\sigma_K)^2 \times\langle\psi' J'\|U^{(K)}\|\psi J\rangle^2 F \qquad \textbf{eqn S7}$$

$$W_{ex} = \frac{(1-\sigma_0)^2}{(2J+1)G}\frac{8\pi}{\hbar}\frac{e^2}{R_L^4}\langle\psi' J'\|S\|\psi J\rangle^2\sum_{m}\left|\langle\phi|\sum_j\mu_z(j)s_m(j)|\phi^*\rangle\right|^2 F \qquad \textbf{eqn S8}$$

where $R_L = 4.53$ Å is the donor–acceptor states distance, Ω_K^{FED} (in **eqn S6**) are the intensity parameters with the contribution of the forced electric dipole mechanism (values in parentheses in **Table S25**). The quantities $\langle \psi' J' \| U^{(K)} \| \psi J \rangle$ are reduced matrix elements and their values are tabulated in Ref.[22] S_L is the dipole strength of the donor state involved in IET (S_1 or T_1). The $\langle r^K \rangle$ are the $4f$ radial integrals,[23,24] G is the state degeneracy (1 for S_1 and 3 for T_1), and $(1 - \sigma_K)$ are the shielding factors.[10,25,26]

In **eqn S8**, s_m is the spin operator in the ligand, μ_z is the dipole operator (its z-component), and $\langle \psi' J' \| S \| \psi J \rangle$ is the reduced matrix elements of the spin operator for the Ln^{3+} side, which were calculated using free-ion wavefunctions in the intermediate coupling scheme.[27,28]

The F (in **eqns S6-S8**) is the spectral overlap factor that contains the energy mismatch conditions. Once the bandwidth at half-height for the ligands (γ_L) is much larger than the lanthanides (γ_{Ln}), $\gamma_L \gg \gamma_{Ln}$, this factor can simply be obtained as follows:[9]

$$F = \frac{1}{\hbar \gamma_L} \sqrt{\frac{\ln(2)}{\pi}} e^{-\left(\frac{\delta}{\hbar \gamma_L}\right)^2 \ln(2)} \qquad \textbf{eqn S9}$$

where the δ is the band maximum energy difference between donor state (D) and lanthanide ion acceptor state, $\delta = E_D - E_{Ln}$. The forward energy transfer rates (W) involving the Ln^{3+} as acceptor are calculated by the sum over all mechanisms in the same pathway:

$$W = W_{d-d} + W_{d-m} + W_{ex} \qquad \textbf{eqn S10}$$

When δ is negative, the energy transfer rate is obtained multiplying F (***eqn S9***) by the Boltzmann's factor,

$$F^b = F e^{-\left(\frac{|\delta|}{k_B T}\right)} \qquad \textbf{eqn S11}$$

where T is the temperature and k_B is Boltzmann's constant. Therefore, the thermal behavior of the energy transfer rates is calculated using an energy barrier described by a Boltzmann distribution.

6.3. Tb^{3+}-to-Sm^{3+} energy transfer

The non-radiative energy transfer rates between lanthanide ions were calculated taking into account the dipole–dipole (W_{d-d}), the dipole–quadrupole (W_{d-q}), the quadrupole–quadrupole (W_{q-q}), and the exchange (W_{ex}) mechanisms:[2]

$$W_{d-d} = \frac{(1-\sigma_1^D)^2 (1-\sigma_1^A)^2}{[J_D^*][J_A]} \frac{4\pi}{3\hbar} \frac{e^4}{{R_L}^6} \times \left(\sum_\lambda \Omega_\lambda^D \langle \psi_D J_D \| U^{(\lambda)} \| \psi_D^* J_D^* \rangle^2 \right) \times \left(\sum_\lambda \Omega_\lambda^A \langle \psi_A^* J_A^* \| U^{(\lambda)} \| \psi_A J_A \rangle^2 \right) F \qquad \textbf{eqn S12}$$

$$W_{d-q,\ q-d} = \frac{\left(1-\sigma_1^{D,A}\right)^2\left(1-\sigma_2^{A,D}\right)^2}{[J_D^*][J_A]}\frac{\pi}{\hbar}\frac{e^4}{R_L{}^8}\langle f\|C^{(2)}\|f\rangle^2 \times\left[\left(\sum_\lambda \Omega_\lambda^D\,\langle\psi_D J_D\|U^{(\lambda)}\|\psi_D^* J_D^*\rangle^2\right)\langle r^2\rangle_A^2\langle\psi_A^* J_A^*\|U^{(2)}\|\psi_A J_A\rangle^2 + \left(\sum_\lambda \Omega_\lambda^A\,\langle\psi_A J_A\|U^{(\lambda)}\|\psi_A^* J_A^*\rangle^2\right)\langle r^2\rangle_D^2\langle\psi_D^* J_D^*\|U^{(2)}\|\psi_D J_D\rangle^2\right]F \quad \textbf{eqn S13}$$

$$W_{q-q} = \frac{(1-\sigma_2^D)^2\left(1-\sigma_2^A\right)^2}{[J_D^*][J_A]}\frac{28\pi}{5\hbar}\frac{e^4}{R_L{}^{10}}\langle r^2\rangle_D^2\langle r^2\rangle_A^2\langle f\|C^{(2)}\|f\rangle^4\langle\psi_D J_D\|U^{(2)}\|\psi_D^* J_D^*\rangle^2 \times\langle\psi_A^* J_A^*\|U^{(2)}\|\psi_A J_A\rangle^2 F \quad \textbf{eqn S14}$$

$$W_{ex} = \frac{2\pi}{\hbar}\left[\left(\frac{e^2}{R_L}\right)\rho_{f-f}^2\right]^2 F \quad \textbf{eqn S15}$$

where the intensity parameters Ω_λ are related to the FED contribution (Ω_λ^{FED} values in **Table S25**). The W_{q-q} and W_{ex} mechanisms are independent of the Judd-Ofelt parameters. ρ_{f-f} is the overlap integral between the 4*f* subshells of the donor and acceptor lanthanide ions. The values of ρ_{f-f} for the pair Tb^{3+}–Sm^{3+} as a function of distance were calculated in Ref.[3], where the ADF (Amsterdam Density Functional) program[4] with the GGA BP86 functional,[5,6] TZ2P Slater-Type basis set,[7] and the inclusion of ZORA scalar relativistic effects[8–10] were employed.

An important quantity to determine the ET transfer rates is the *F*-factor, which includes contributions from the nuclear wavefunctions and the density of states. In the case of energy transfer between two lanthanide ions the following expression for F has been used:[2]

$$F = \frac{\ln(2)}{\sqrt{\pi}}\frac{1}{\hbar^2\gamma_D\gamma_A}\left\{\left[\left(\frac{1}{\hbar\gamma_D}\right)^2+\left(\frac{1}{\hbar\gamma_A}\right)^2\right]\ln(2)\right\}^{-\frac{1}{2}} \times\exp\left[\frac{1}{4}\frac{\left(\frac{2\delta}{(\hbar\gamma_D)^2}\ln 2\right)^2}{\left[\left(\frac{1}{\hbar\gamma_A}\right)^2+\left(\frac{1}{\hbar\gamma_D}\right)^2\right]\ln 2}-\left(\frac{\delta}{\hbar\gamma_D}\right)^2\ln(2)\right] \quad \textbf{eqn S16}$$

where $\hbar\gamma_D$ and $\hbar\gamma_A$ correspond to the bandwidths at half-height (in erg) of the donor and acceptor. For the present analysis, we considered $\gamma_D = \gamma_A = 400$ cm^{-1}. Δ is the energy difference between baricenters of donor and acceptor transitions, $\delta = E_D - E_A$. Notice that the *F*-factor is given in erg^{-1} and ***eqn* S9** is a simplified form of ***eqn S16*** once the bandwidths at half-height of the donor transitions is (S_1 and T_1 states in the case of Ligand-to-Ln^{3+} energy transfer) are larger than the Ln^{3+} transitions.

The energy transfer mechanisms, pathways and their respective donor and acceptor states were selected according to energy mismatch conditions (**Figure S32**) and selection rules on the J quantum numbers. These selection rules are $|J-J'| \le K \le J+J'$ for the multipolar mechanisms (W_{d-d}, W_{d-q} and W_{q-q}). For the exchange mechanism (W_{ex}), the isotropic contribution, no defined selection rules on *J* appear.

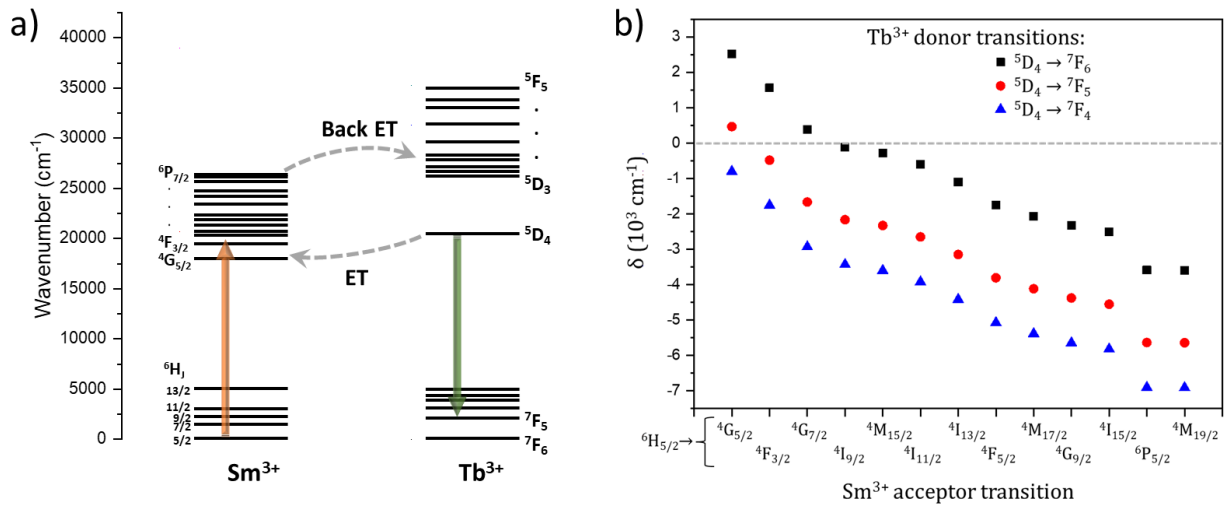

Figure S32. a) Simplified energy level diagram showing the energy levels of Tb^{3+} and Sm^{3+} ions. b) The energy difference (δ) between donor (Tb^{3+}) and acceptor (Sm^{3+}) transitions involved in the energy transfer process. The energy transfer pathways close to the dashed gray line (δ = 0) are those in good resonance conditions (e.g., Tb^{3+} [$^5D_4 \rightarrow {}^7F_6$] → Sm^{3+} [$^6H_{5/2} \rightarrow {}^4I_{9/2}$] pathway has δ ≈ – 115 cm^{-1}).

As emphasized through this work, the case of the mixture Sm_2moshi_8:Tb_2moshi_8 presents a minimal Sm^{3+}–Tb^{3+} distance of R_L = 7 Å, leading to a very low value of $\rho_{f-f} = 3.2 \times 10^{-9}$, and we anticipate that at this distance, the calculated exchange mechanism is $W_{ex} = 8.9 \times 10^{-9}$ s^{-1} and could be neglected. Thus, we will focus on the multipolar mechanisms (W_{d-d}, W_{d-q}, and W_{q-q}) in the evaluation of the Tb-to-Sm energy transfer rates. Therefore, the energy transfer rate of a given pathway is obtained by the sum over ***eqns S12, S13, and S14*** $\left(W = W_{d-d} + W_{d-q} + W_{q-q}\right)$ multiplying by the barrier factor $e^{-\left(\frac{|\Delta|}{k_B T}\right)}$ if δ is negative (**Figure S32b**). k_B is Boltzmann's constant and T is the temperature (300 K).

7. Theoretical results

7.1 Energy transfer rates

All pathways listed in **Tables S26**–**S33** take into account the selection rules on J quantum number ($|J - J'| \leq \lambda \leq J + J'$ for the dipole–dipole and the dipole–multipole mechanisms, $\Delta J = 0, \pm 1$ for the exchange mechanism)[9] and they represent the rates for 300 K for the MCs with shi, mshi, moshi, and nha ligands. **Tables S26**, **S28**, **S30**, and **S32** display the rates for Tb-based MCs while the rates for Sm-based ones are recorded in **Tables S27**, **S29**, **S31**, and **S33**. Considering the non-zero contributions, 76 energy transfer pathways (42 for Ligand-to-Tb^{3+} and 34 for Ligand-to-Sm^{3+}) were analyzed for each system (Ln–shi, –mshi, –moshi, and –nha) at a given constant temperature. Considering the overall procedure (including the 22 different temperatures in the range of 11–425 K), 1672 IET rates were calculated.

It is important to mention that some rates cannot be considered in the overall IET once a high barrier ($|\delta| \gg k_B T$) from the singlet to the Ln^{3+} level is present. For example, in **Table S26** we have not been considered the IET involving the levels above $^5H_6$ because the $S_1 \rightarrow (^7F_5 \rightarrow {}^5H_6)$ has $\delta = -3043$ cm^{-1} (pathway 19), meaning that this level will not be effectively populated and, consequently, does not make sense as a backward IET rate $(^7F_5 \rightarrow {}^5H_6) \rightarrow S_1$ of 2.62×10^3 s^{-1} (by the exchange mechanism). Using the same logic, the next level $^5H_5$, will also not contribute with a backward IET rate $(^7F_5 \rightarrow {}^5H_5) \rightarrow S_1$ of 2.56×10^5 s^{-1} (pathway 20) which is faster than the overall rate at 300 K. This analysis is similar to the procedure described in Ref.[29]

Table S26. shi^{3-}-to-Tb^{3+} energy transfer rates at 300 K. δ is the donor–acceptor energy difference (in cm^{-1}). W_{d-d}, W_{d-m}, and W_{ex} are the dipole–dipole, dipole–multipole, and exchange rates (in s^{-1}), respectively. W and W^b are the forward and backward IET.

PATHWAY LABEL	DONOR	ACCEPTOR	δ	W_{d-d}	W_{d-m}	W_{ex}	W (FORWARD)	W^b (BACKWARD)
1	S_1	$^7F_6 \rightarrow {}^5D_4$	7356	1.39E+01	4.91E+02	0.00E+00	5.05E+02	2.41E–13
2	S_1	$^7F_6 \rightarrow {}^5D_3$	1564	6.52E+02	1.83E+01	0.00E+00	6.70E+02	3.71E–01
3	S_1	$^7F_6 \rightarrow {}^5G_6$	1377	5.47E+04	4.91E+04	1.11E+07	1.12E+07	1.52E+04
4	S_1	$^7F_6 \rightarrow {}^5L_{10}$	829	2.97E+04	6.59E+01	0.00E+00	2.97E+04	5.58E+02
5	S_1	$^7F_6 \rightarrow {}^5G_5$	33	7.44E+03	4.24E+04	6.07E+04	1.11E+05	9.44E+04
6	S_1	$^7F_6 \rightarrow {}^5G_4$	–487	4.66E+03	3.49E+03	0.00E+00	7.88E+02	8.14E+03
7	S_1	$^7F_6 \rightarrow {}^5L_6$	–1810	0.00E+00	0.00E+00	2.60E+03	4.42E–01	2.60E+03
8	S_1	$^7F_6 \rightarrow {}^5H_7$	–3579	0.00E+00	0.00E+00	1.55E+03		
9	S_1	$^7F_6 \rightarrow {}^5H_6$	–5091	0.00E+00	0.00E+00	3.68E+04		
10	S_1	$^7F_6 \rightarrow {}^5H_5$	–5967	0.00E+00	0.00E+00	2.13E–12		
11	S_1	$^7F_6 \rightarrow {}^5F_5$	–7134	0.00E+00	0.00E+00	2.26E+04		
12	S_1	$^7F_5 \rightarrow {}^5D_4$	9404	3.18E+00	6.50E+02	1.42E+02	7.95E+02	2.06E–17
13	S_1	$^7F_5 \rightarrow {}^5D_3$	3612	5.93E+02	7.73E+03	0.00E+00	8.33E+03	2.50E–04
14	S_1	$^7F_5 \rightarrow {}^5G_6$	3425	2.76E+03	6.75E+04	1.06E+05	1.77E+05	1.30E–02
15	S_1	$^7F_5 \rightarrow {}^5L_{10}$	2877	5.04E+02	6.08E-01	0.00E+00	5.05E+02	5.14E–04
16	S_1	$^7F_5 \rightarrow {}^5G_5$	2081	3.00E+03	3.00E+03	2.09E+06	2.10E+06	9.71E+01
17	S_1	$^7F_5 \rightarrow {}^5G_4$	1561	1.14E+03	1.72E+04	3.89E+04	5.72E+04	3.21E+01
18	S_1	$^7F_5 \rightarrow {}^5L_6$	238	0.00E+00	0.00E+00	7.33E+01	7.33E+01	2.34E+01
19	S_1	$^7F_5 \rightarrow {}^5H_6$	–3043	0.00E+00	0.00E+00	2.62E+03		
20	S_1	$^7F_5 \rightarrow {}^5H_5$	–3919	0.00E+00	0.00E+00	2.56E+05		
21	S_1	$^7F_5 \rightarrow {}^5F_5$	–5086	0.00E+00	0.00E+00	2.00E+05		
						W_S	1.37×10^7	
						W_S^b		1.21×10^5
22	T_1	$^7F_6 \rightarrow {}^5D_4$	1536	7.51	2.65E+2	0.00	2.72E+02	1.72E–01
23	T_1	$^7F_6 \rightarrow {}^5D_3$	–4256	1.95	5.49E-2	0.00	2.74E-09	2.01E+00
24	T_1	$^7F_6 \rightarrow {}^5G_6$	–4443	1.38E+2	1.24E+2	2.82E+6	1.57E–03	2.82E+06
25	T_1	$^7F_6 \rightarrow {}^5L_{10}$	–4991	4.59E+1	1.02E-1	0.00	1.85E–09	4.60E+01
26	T_1	$^7F_6 \rightarrow {}^5G_5$	–5787	5.64	3.21E+1	4.61E+3	4.11E–09	4.64E+03
27	T_1	$^7F_6 \rightarrow {}^5G_4$	–6307	2.22	1.66	0.00	2.83E–13	3.87E+00
28	T_1	$^7F_6 \rightarrow {}^5L_6$	–7630	0.00	0.00	3.78E+1	4.85E–15	3.78E+01
29	T_1	$^7F_6 \rightarrow {}^5H_7$	–9399	0.00	0.00	4.62		
30	T_1	$^7F_6 \rightarrow {}^5H_6$	–10911	0.00	0.00	2.83E+1		
31	T_1	$^7F_6 \rightarrow {}^5H_5$	–11787	0.00	0.00	7.44E-16		
32	T_1	$^7F_6 \rightarrow {}^5F_5$	–12954	0.00	0.00	2.78		
33	T_1	$^7F_5 \rightarrow {}^5D_4$	3584	9.07	1.86E+3	4.80E+4	4.99E+04	1.71E-03
34	T_1	$^7F_5 \rightarrow {}^5D_3$	–2208	9.41	1.23E+2	0.00	3.33E-03	1.32E+02
35	T_1	$^7F_5 \rightarrow {}^5G_6$	–2395	3.71E+1	9.06E+2	1.69E+5	1.74E+00	1.70E+05
36	T_1	$^7F_5 \rightarrow {}^5L_{10}$	–2943	4.14	4.99E-3	0.00	3.08E–06	4.15E+00
37	T_1	$^7F_5 \rightarrow {}^5G_5$	–3739	1.21E+1	1.21E+1	9.95E+5	1.62E–02	9.95E+05
38	T_1	$^7F_5 \rightarrow {}^5G_4$	–4259	2.89	4.35E+1	1.16E+4	1.57E–05	1.16E+04
39	T_1	$^7F_5 \rightarrow {}^5L_6$	–5582	0.00	0.00	6.68	1.58E–11	6.68E+00
40	T_1	$^7F_5 \rightarrow {}^5H_6$	–8863	0.00	0.00	1.26E+1		
41	T_1	$^7F_5 \rightarrow {}^5H_5$	–9739	0.00	0.00	5.62E+2		
42	T_1	$^7F_5 \rightarrow {}^5F_5$	–10906	0.00	0.00	1.54E+2		
						W_T	5.01×10^4	
						W_T^b		4.00×10^6

Table S27. shi^{3-}-to-Sm^{3+} energy transfer rates at 300 K. δ is the donor–acceptor energy difference (in cm^{-1}). W_{d-d}, W_{d-m}, and W_{ex} are the dipole–dipole, dipole–multipole, and exchange rates (in s^{-1}), respectively. W and W^b are the forward and backward IET.

PATHWAY LABEL	DONOR	ACCEPTOR	δ	W_{d-d}	W_{d-m}	W_{ex}	W (FORWARD)	W^b (BACKWARD)
1	S_1	$^6H_{5/2}\rightarrow{}^4G_{5/2}$	9870	0.00E+00	0.00E+00	7.81E+05	7.81E+05	2.16E-15
2	S_1	$^6H_{5/2}\rightarrow{}^4G_{7/2}$	7740	1.06E+02	2.30E+02	1.01E+07	1.01E+07	7.65E-10
3	S_1	$^6H_{5/2}\rightarrow{}^4I_{9/2}$	7241	1.15E+02	2.96E+03	0.00E+00	3.07E+03	2.54E-12
4	S_1	$^6H_{5/2}\rightarrow{}^4M_{15/2}$	7076	2.59E+03	9.48E-01	0.00E+00	2.59E+03	4.74E-12
5	S_1	$^6H_{5/2}\rightarrow{}^4I_{11/2}$	6754	1.27E+03	4.65E-01	0.00E+00	1.27E+03	1.09E-11
6	S_1	$^6H_{5/2}\rightarrow{}^4I_{13/2}$	6257	4.62E+03	3.77E+01	0.00E+00	4.66E+03	4.33E-10
7	S_1	$^6H_{5/2}\rightarrow{}^4F_{5/2}$	5600	0.00E+00	0.00E+00	1.27E+08	1.27E+08	2.74E-04
8	S_1	$^6H_{5/2}\rightarrow{}^4M_{17/2}$	5289	2.40E+03	8.80E-01	0.00E+00	2.41E+03	2.32E-08
9	S_1	$^6H_{5/2}\rightarrow{}^4G_{9/2}$	5028	1.61E+03	3.01E+01	0.00E+00	1.64E+03	5.53E-08
10	S_1	$^6H_{5/2}\rightarrow{}^6P_{5/2}$	3769	8.42E+03	1.88E+03	0.00E+00	1.03E+04	1.45E-04
11	S_1	$^6H_{5/2}\rightarrow{}^4L_{13/2}$	3225	1.96E+04	8.32E+02	0.00E+00	2.04E+04	3.91E-03
12	S_1	$^6H_{5/2}\rightarrow{}^4F_{7/2}$	2906	1.62E+03	8.08E+03	0.00E+00	9.70E+03	8.59E-03
13	S_1	$^6H_{5/2}\rightarrow{}^6P_{3/2}$	2837	9.03E+04	2.02E+04	0.00E+00	1.10E+05	1.36E-01
14	S_1	$^6H_{5/2}\rightarrow{}^4K_{11/2}$	2700	5.49E+03	5.44E+01	0.00E+00	5.55E+03	1.32E-02
15	S_1	$^6H_{5/2}\rightarrow{}^4L_{15/2}$	2234	1.46E+04	5.36E+00	0.00E+00	1.46E+04	3.26E-01
16	S_1	$^6H_{5/2}\rightarrow{}^4G_{11/2}$	2072	2.83E+03	1.75E+01	0.00E+00	2.85E+03	1.38E-01
17	S_1	$^6H_{5/2}\rightarrow{}^6P_{7/2}$	1115	2.33E+05	3.98E+02	0.00E+00	2.33E+05	1.11E+03
						W_S	1.38×10^8	
						W_S^b		1.11×10^3
18	T_1	$^6H_{5/2}\rightarrow{}^4G_{5/2}$	4050	0.00	0.00	4.00×10^8	4.00E+08	1.47E+00
19	T_1	$^6H_{5/2}\rightarrow{}^4G_{7/2}$	1920	8.03E+1	1.75E+2	7.68E+8	7.68E+08	7.69E+04
20	T_1	$^6H_{5/2}\rightarrow{}^4I_{9/2}$	1421	5.58E+1	1.44E+3	0.00	1.49E+03	1.64E+00
21	T_1	$^6H_{5/2}\rightarrow{}^4M_{15/2}$	1256	1.08E+3	3.97E-1	0.00	1.09E+03	2.63E+00
22	T_1	$^6H_{5/2}\rightarrow{}^4I_{11/2}$	934	3.99E+2	1.46E-1	0.00	3.99E+02	4.52E+00
23	T_1	$^6H_{5/2}\rightarrow{}^4I_{13/2}$	437	9.29E+2	7.58	0.00	9.37E+02	1.15E+02
24	T_1	$^6H_{5/2}\rightarrow{}^4F_{5/2}$	-220	0.00	0.00	1.41E+9	4.91E+08	1.41E+09
25	T_1	$^6H_{5/2}\rightarrow{}^4M_{17/2}$	-531	2.03E+2	7.42E-2	0.00	1.59E+01	2.03E+02
26	T_1	$^6H_{5/2}\rightarrow{}^4G_{9/2}$	-792	1.08E+2	2.01	0.00	2.46E+00	1.10E+02
27	T_1	$^6H_{5/2}\rightarrow{}^6P_{5/2}$	-2051	1.82E+2	4.06E+1	0.00	1.19E-02	2.22E+02
28	T_1	$^6H_{5/2}\rightarrow{}^4L_{13/2}$	-2595	2.59E+2	1.10E+1	0.00	1.06E-03	2.70E+02
29	T_1	$^6H_{5/2}\rightarrow{}^4F_{7/2}$	-2914	1.62E+1	8.05E+1	0.00	8.24E-05	9.67E+01
30	T_1	$^6H_{5/2}\rightarrow{}^6P_{3/2}$	-2983	8.46E+2	1.89E+2	0.00	6.34E-04	1.03E+03
31	T_1	$^6H_{5/2}\rightarrow{}^4K_{11/2}$	-3120	4.55E+1	4.51E-1	0.00	1.46E-05	4.59E+01
32	T_1	$^6H_{5/2}\rightarrow{}^4L_{15/2}$	-3586	7.99E+1	2.92E-2	0.00	2.71E-06	7.99E+01
33	T_1	$^6H_{5/2}\rightarrow{}^4G_{11/2}$	-3748	1.34E+1	8.27E-2	0.00	2.10E-07	1.34E+01
34	T_1	$^6H_{5/2}\rightarrow{}^6P_{7/2}$	-4705	4.66E+2	7.96E-1	0.00	7.40E-08	4.66E+02
						W_T	1.66×10^9	
						W_T^b		1.41×10^9

Table S28. mshi^{3-}-to-Tb^{3+} energy transfer rates at 300 K. δ is the donor–acceptor energy difference (in cm^{-1}). W_{d-d}, W_{d-m}, and W_{ex} are the dipole–dipole, dipole–multipole, and exchange rates (in s^{-1}), respectively. W and W^b are the forward and backward IET.

PATHWAY LABEL	DONOR	ACCEPTOR	Δ	W_{d-d}	W_{d-m}	W_{ex}	W (FORWARD)	W^b (BACKWARD)
1	S_1	$^7F_6 \rightarrow {}^5D_4$	6456	3.63E+01	1.28E+03	0.00E+00	1.32E+03	4.71E-11
2	S_1	$^7F_6 \rightarrow {}^5D_3$	664	7.61E+02	2.14E+01	0.00E+00	7.82E+02	3.24E+01
3	S_1	$^7F_6 \rightarrow {}^5G_6$	477	6.22E+04	5.58E+04	1.27E+07	1.28E+07	1.30E+06
4	S_1	$^7F_6 \rightarrow {}^5L_{10}$	-71	3.13E+04	6.94E+01	0.00E+00	2.23E+04	3.13E+04
5	S_1	$^7F_6 \rightarrow {}^5G_5$	-867	7.02E+03	4.00E+04	5.73E+04	1.63E+03	1.04E+05
6	S_1	$^7F_6 \rightarrow {}^5G_4$	-1387	4.09E+03	3.06E+03	0.00E+00	9.24E+00	7.15E+03
7	S_1	$^7F_6 \rightarrow {}^5L_6$	-2710	0.00E+00	0.00E+00	1.90E+03	4.32E-03	1.90E+03
8	S_1	$^7F_6 \rightarrow {}^5H_7$	-4479	0.00E+00	0.00E+00	8.89E+02		
9	S_1	$^7F_6 \rightarrow {}^5H_6$	-5991	0.00E+00	0.00E+00	1.71E+04		
10	S_1	$^7F_6 \rightarrow {}^5H_5$	-6867	0.00E+00	0.00E+00	8.73E-13		
11	S_1	$^7F_6 \rightarrow {}^5F_5$	-8034	0.00E+00	0.00E+00	7.90E+03		
12	S_1	$^7F_5 \rightarrow {}^5D_4$	8504	1.10E+01	2.25E+03	4.92E+02	2.75E+03	5.34E-15
13	S_1	$^7F_5 \rightarrow {}^5D_3$	2712	9.18E+02	1.20E+04	0.00E+00	1.29E+04	2.90E-02
14	S_1	$^7F_5 \rightarrow {}^5G_6$	2525	4.17E+03	1.02E+05	1.61E+05	2.67E+05	1.47E+00
15	S_1	$^7F_5 \rightarrow {}^5L_{10}$	1977	7.06E+02	8.51E-01	0.00E+00	7.07E+02	5.39E-02
16	S_1	$^7F_5 \rightarrow {}^5G_5$	1181	3.76E+03	3.76E+03	2.62E+06	2.63E+06	9.12E+03
17	S_1	$^7F_5 \rightarrow {}^5G_4$	661	1.33E+03	2.01E+04	4.54E+04	6.68E+04	2.80E+03
18	S_1	$^7F_5 \rightarrow {}^5L_6$	-662	0.00E+00	0.00E+00	7.11E+01	2.97E+00	7.11E+01
19	S_1	$^7F_5 \rightarrow {}^5H_6$	-3943	0.00E+00	0.00E+00	1.61E+03		
20	S_1	$^7F_5 \rightarrow {}^5H_5$	-4819	0.00E+00	0.00E+00	1.40E+05		
21	S_1	$^7F_5 \rightarrow {}^5F_5$	-5986	0.00E+00	0.00E+00	9.26E+04		
						W_S	1.58×10^{7}	
						W_S^b		1.45×10^{6}
22	T_1	$^7F_6 \rightarrow {}^5D_4$	1126	8.17	2.88E+2	0.00	2.96E+2	1.34
23	T_1	$^7F_6 \rightarrow {}^5D_3$	-4666	1.47	4.14E-2	0.00	2.89E-10	1.51
24	T_1	$^7F_6 \rightarrow {}^5G_6$	-4853	1.03E+2	9.26E+1	2.10E+6	1.64E-4	2.10E+6
25	T_1	$^7F_6 \rightarrow {}^5L_{10}$	-5401	3.31E+1	7.34E-2	0.00	1.87E-10	3.31E+1
26	T_1	$^7F_6 \rightarrow {}^5G_5$	-6197	3.87	2.20E+1	3.15E+3	3.94E-10	3.18E+3
27	T_1	$^7F_6 \rightarrow {}^5G_4$	-6717	1.47	1.10	0.00	2.63E-14	2.57
28	T_1	$^7F_6 \rightarrow {}^5L_6$	-8040	0.00	0.00	2.31E+1	4.14E-16	2.31E+1
29	T_1	$^7F_6 \rightarrow {}^5H_7$	-9809	0.00	0.00	2.52	9.35E-21	2.52
30	T_1	$^7F_6 \rightarrow {}^5H_6$	-11321	0.00	0.00	1.40E+1	3.69E-23	1.40E+1
31	T_1	$^7F_6 \rightarrow {}^5H_5$	-12197	0.00	0.00	3.49E-16	1.37E-41	3.49E-16
32	T_1	$^7F_6 \rightarrow {}^5F_5$	-13364	0.00	0.00	1.21	1.77E-28	1.21
33	T_1	$^7F_5 \rightarrow {}^5D_4$	3174	1.12E+1	2.30E+3	5.94E+4	6.17E+4	1.51E-2
34	T_1	$^7F_5 \rightarrow {}^5D_3$	-2618	8.08	1.05E+2	0.00	4.00E-4	1.14E+2
35	T_1	$^7F_5 \rightarrow {}^5G_6$	-2805	3.15E+1	7.69E+2	1.43E+5	2.07E-1	1.44E+5
36	T_1	$^7F_5 \rightarrow {}^5L_{10}$	-3353	3.40	4.09E-3	0.00	3.53E-7	3.40
37	T_1	$^7F_5 \rightarrow {}^5G_5$	-4149	9.40	9.40	7.75E+5	1.77E-3	7.75E+5
38	T_1	$^7F_5 \rightarrow {}^5G_4$	-4669	2.18	3.28E+1	8.75E+3	1.66E-6	8.79E+3
39	T_1	$^7F_5 \rightarrow {}^5L_6$	-5992	0.00	0.00	4.63	1.53E-12	4.63
40	T_1	$^7F_5 \rightarrow {}^5H_6$	-9273	0.00	0.00	7.11		
41	T_1	$^7F_5 \rightarrow {}^5H_5$	-10149	0.00	0.00	3.00E+2		
42	T_1	$^7F_5 \rightarrow {}^5F_5$	-11316	0.00	0.00	7.62E+1		
						W_T	6.20×10^{4}	
						W_T^b		3.03×10^{6}

Table S29. mshi^{3-}-to-Sm^{3+} energy transfer rates at 300 K. δ is the donor–acceptor energy difference (in cm^{-1}). W_{d-d}, W_{d-m}, and W_{ex} are the dipole–dipole, dipole–multipole, and exchange rates (in s^{-1}), respectively. W and W^b are the forward and backward IET.

PATHWAY LABEL	DONOR	ACCEPTOR	δ	W_{d-d}	W_{d-m}	W_{ex}	W (FORWARD)	W^b (BACKWARD)
1	S_1	$^6H_{5/2}\rightarrow{}^4G_{5/2}$	8970	0.00E+00	0.00E+00	2.88E+06	2.88E+06	5.98E-13
2	S_1	$^6H_{5/2}\rightarrow{}^4G_{7/2}$	6840	2.91E+02	6.33E+02	2.78E+07	2.78E+07	1.57E-07
3	S_1	$^6H_{5/2}\rightarrow{}^4I_{9/2}$	6341	2.95E+02	7.58E+03	0.00E+00	7.87E+03	4.88E-10
4	S_1	$^6H_{5/2}\rightarrow{}^4M_{15/2}$	6176	6.49E+03	2.37E+00	0.00E+00	6.49E+03	8.89E-10
5	S_1	$^6H_{5/2}\rightarrow{}^4I_{11/2}$	5854	3.04E+03	1.11E+00	0.00E+00	3.05E+03	1.95E-09
6	S_1	$^6H_{5/2}\rightarrow{}^4I_{13/2}$	5357	1.03E+04	8.44E+01	0.00E+00	1.04E+04	7.25E-08
7	S_1	$^6H_{5/2}\rightarrow{}^4F_{5/2}$	4700	0.00E+00	0.00E+00	2.58E+08	2.58E+08	4.20E-02
8	S_1	$^6H_{5/2}\rightarrow{}^4M_{17/2}$	4389	4.70E+03	1.72E+00	0.00E+00	4.71E+03	3.40E-06
9	S_1	$^6H_{5/2}\rightarrow{}^4G_{9/2}$	4128	3.04E+03	5.67E+01	0.00E+00	3.10E+03	7.82E-06
10	S_1	$^6H_{5/2}\rightarrow{}^6P_{5/2}$	2869	1.33E+04	2.98E+03	0.00E+00	1.63E+04	1.72E-02
11	S_1	$^6H_{5/2}\rightarrow{}^4L_{13/2}$	2325	2.87E+04	1.22E+03	0.00E+00	3.00E+04	4.30E-01
12	S_1	$^6H_{5/2}\rightarrow{}^4F_{7/2}$	2006	2.28E+03	1.14E+04	0.00E+00	1.36E+04	9.05E-01
13	S_1	$^6H_{5/2}\rightarrow{}^6P_{3/2}$	1937	1.26E+05	2.81E+04	0.00E+00	1.54E+05	1.42E+01
14	S_1	$^6H_{5/2}\rightarrow{}^4K_{11/2}$	1800	7.50E+03	7.43E+01	0.00E+00	7.58E+03	1.35E+00
15	S_1	$^6H_{5/2}\rightarrow{}^4L_{15/2}$	1334	1.88E+04	6.86E+00	0.00E+00	1.88E+04	3.12E+01
16	S_1	$^6H_{5/2}\rightarrow{}^4G_{11/2}$	1172	3.55E+03	2.20E+01	0.00E+00	3.57E+03	1.29E+01
17	S_1	$^6H_{5/2}\rightarrow{}^6P_{7/2}$	215	2.55E+05	4.37E+02	0.00E+00	2.56E+05	9.12E+04
						W_S	2.90×10^8	
						W_S^b		9.12×10^4
18	T_1	$^6H_{5/2}\rightarrow{}^4G_{5/2}$	3640	0.00	0.00	5.11E+8	5.11E+8	1.34E+1
19	T_1	$^6H_{5/2}\rightarrow{}^4G_{7/2}$	1510	8.95E+1	1.95E+2	8.56E+8	8.56E+8	6.13E+5
20	T_1	$^6H_{5/2}\rightarrow{}^4I_{9/2}$	1011	6.03E+1	1.55E+3	0.00	1.61E+3	1.26E+1
21	T_1	$^6H_{5/2}\rightarrow{}^4M_{15/2}$	846	1.16E+3	4.24E-1	0.00	1.16E+3	2.01E+1
22	T_1	$^6H_{5/2}\rightarrow{}^4I_{11/2}$	524	4.17E+2	1.53E-1	0.00	4.18E+2	3.38E+1
23	T_1	$^6H_{5/2}\rightarrow{}^4I_{13/2}$	27	9.43E+2	7.69	0.00	9.51E+2	8.35E+2
24	T_1	$^6H_{5/2}\rightarrow{}^4F_{5/2}$	-630	0.00	0.00	1.37E+9	6.69E+7	1.37E+9
25	T_1	$^6H_{5/2}\rightarrow{}^4M_{17/2}$	-941	1.94E+2	7.09E-2	0.00	2.12	1.94E+2
26	T_1	$^6H_{5/2}\rightarrow{}^4G_{9/2}$	-1202	1.01E+2	1.89	0.00	3.23E-1	1.03E+2
27	T_1	$^6H_{5/2}\rightarrow{}^6P_{5/2}$	-2461	1.58E+2	3.52E+1	0.00	1.44E-3	1.93E+2
28	T_1	$^6H_{5/2}\rightarrow{}^4L_{13/2}$	-3005	2.17E+2	9.24	0.00	1.25E-4	2.27E+2
29	T_1	$^6H_{5/2}\rightarrow{}^4F_{7/2}$	-3324	1.33E+1	6.61E+1	0.00	9.47E-6	7.94E+1
30	T_1	$^6H_{5/2}\rightarrow{}^6P_{3/2}$	-3393	6.92E+2	1.54E+2	0.00	7.25E-5	8.46E+2
31	T_1	$^6H_{5/2}\rightarrow{}^4K_{11/2}$	-3530	3.69E+1	3.65E-1	0.00	1.65E-6	3.72E+1
32	T_1	$^6H_{5/2}\rightarrow{}^4L_{15/2}$	-3996	6.29E+1	2.30E-2	0.00	2.99E-7	6.29E+1
33	T_1	$^6H_{5/2}\rightarrow{}^4G_{11/2}$	-4158	1.04E+1	6.44E-2	0.00	2.29E-8	1.05E+1
34	T_1	$^6H_{5/2}\rightarrow{}^6P_{7/2}$	-5115	3.42E+2	5.84E-1	0.00	7.59E-9	3.42E+2
						W_T	1.43×10^9	
						W_T^b		1.37×10^9

Table S30. moshi^{3-}-to-Tb^{3+} energy transfer rates at 300 K. δ is the donor–acceptor energy difference (in cm^{-1}). W_{d-d}, W_{d-m}, and W_{ex} are the dipole–dipole, dipole–multipole, and exchange rates (in s^{-1}), respectively. W and W^b are the forward and backward IET.

PATHWAY LABEL	DONOR	ACCEPTOR	δ	W_{d-d}	W_{d-m}	W_{ex}	W (FORWARD)	W^b (BACKWARD)
1	S_1	$^7F_6 \rightarrow {}^5D_4$	4956	1.36E+02	4.78E+03	0.00E+00	4.92E+03	2.34E-07
2	S_1	$^7F_6 \rightarrow {}^5D_3$	-836	7.46E+02	2.10E+01	0.00E+00	1.39E+01	7.67E+02
3	S_1	$^7F_6 \rightarrow {}^5G_6$	-1023	5.84E+04	5.24E+04	1.19E+07	8.88E+04	1.20E+07
4	S_1	$^7F_6 \rightarrow {}^5L_{10}$	-1571	2.59E+04	5.74E+01	0.00E+00	1.38E+01	2.59E+04
5	S_1	$^7F_6 \rightarrow {}^5G_5$	-2367	4.83E+03	2.75E+04	3.94E+04		
6	S_1	$^7F_6 \rightarrow {}^5G_4$	-2887	2.50E+03	1.87E+03	0.00E+00		
7	S_1	$^7F_6 \rightarrow {}^5L_6$	-4210	0.00E+00	0.00E+00	8.56E+02		
8	S_1	$^7F_6 \rightarrow {}^5H_7$	-5979	0.00E+00	0.00E+00	2.66E+02		
9	S_1	$^7F_6 \rightarrow {}^5H_6$	-7491	0.00E+00	0.00E+00	3.60E+03		
10	S_1	$^7F_6 \rightarrow {}^5H_5$	-8367	0.00E+00	0.00E+00	1.50E-13		
11	S_1	$^7F_6 \rightarrow {}^5F_5$	-9534	0.00E+00	0.00E+00	1.04E+03		
12	S_1	$^7F_5 \rightarrow {}^5D_4$	7004	6.59E+01	1.35E+04	2.95E+03	1.65E+04	4.26E-11
13	S_1	$^7F_5 \rightarrow {}^5D_3$	1212	1.45E+03	1.89E+04	0.00E+00	2.03E+04	6.07E+01
14	S_1	$^7F_5 \rightarrow {}^5G_6$	1025	6.29E+03	1.54E+05	2.42E+05	4.02E+05	2.95E+03
15	S_1	$^7F_5 \rightarrow {}^5L_{10}$	477	9.38E+02	1.13E+00	0.00E+00	9.39E+02	9.53E+01
16	S_1	$^7F_5 \rightarrow {}^5G_5$	-319	4.15E+03	4.15E+03	2.90E+06		
17	S_1	$^7F_5 \rightarrow {}^5G_4$	-839	1.31E+03	1.97E+04	4.44E+04		
18	S_1	$^7F_5 \rightarrow {}^5L_6$	-2162	0.00E+00	0.00E+00	5.13E+01		
19	S_1	$^7F_5 \rightarrow {}^5H_6$	-5443	0.00E+00	0.00E+00	5.46E+02		
20	S_1	$^7F_5 \rightarrow {}^5H_5$	-6319	0.00E+00	0.00E+00	3.86E+04		
21	S_1	$^7F_5 \rightarrow {}^5F_5$	-7486	0.00E+00	0.00E+00	1.95E+04		
						W_S	5.34×10^5	
						W_S^b		1.20×10^7
22	T_1	$^7F_6 \rightarrow {}^5D_4$	1196	8.06	2.84E+2	0.00	2.92E+02	9.43E-01
23	T_1	$^7F_6 \rightarrow {}^5D_3$	-4596	1.55	4.35E-2	0.00	4.26E-10	1.59E+00
24	T_1	$^7F_6 \rightarrow {}^5G_6$	-4783	1.09E+2	9.75E+1	2.21E+6	2.41E-04	2.21E+06
25	T_1	$^7F_6 \rightarrow {}^5L_{10}$	-5331	3.50E+1	7.78E-2	0.00	2.77E-10	3.51E+01
26	T_1	$^7F_6 \rightarrow {}^5G_5$	-6127	4.13	2.35E+1	3.37E+3		
27	T_1	$^7F_6 \rightarrow {}^5G_4$	-6647	1.58	1.18	0.00		
28	T_1	$^7F_6 \rightarrow {}^5L_6$	-7970	0.00	0.00	2.52E+1		
29	T_1	$^7F_6 \rightarrow {}^5H_7$	-9739	0.00	0.00	2.80		
30	T_1	$^7F_6 \rightarrow {}^5H_6$	-11251	0.00	0.00	1.58E+1		
31	T_1	$^7F_6 \rightarrow {}^5H_5$	-12127	0.00	0.00	3.98E-16		
32	T_1	$^7F_6 \rightarrow {}^5F_5$	-13294	0.00	0.00	1.40		
33	T_1	$^7F_5 \rightarrow {}^5D_4$	3244	1.08E+1	2.22E+3	5.74E+4	5.96E+04	1.04E-02
34	T_1	$^7F_5 \rightarrow {}^5D_3$	-2548	8.31	1.08E+2	0.00	5.76E-04	1.17E+02
35	T_1	$^7F_5 \rightarrow {}^5G_6$	-2735	3.24E+1	7.92E+2	1.48E+5	2.99E-01	1.49E+05
36	T_1	$^7F_5 \rightarrow {}^5L_{10}$	-3283	3.52	4.24E-3	0.00	5.12E-07	3.52E+00
37	T_1	$^7F_5 \rightarrow {}^5G_5$	-4079	9.83	9.83	8.11E+5		
38	T_1	$^7F_5 \rightarrow {}^5G_4$	-4599	2.29	3.45E+1	9.20E+3		
39	T_1	$^7F_5 \rightarrow {}^5L_6$	-5922	0.00	0.00	4.94		
40	T_1	$^7F_5 \rightarrow {}^5H_6$	-9203	0.00	0.00	7.86		
41	T_1	$^7F_5 \rightarrow {}^5H_5$	-10079	0.00	0.00	3.34E+2		
42	T_1	$^7F_5 \rightarrow {}^5F_5$	-11246	0.00	0.00	8.61E+1		
						W_T	5.99×10^4	
						W_T^b		2.36×10^6

Table S31. moshi^{3-}-to-Sm^{3+} energy transfer rates at 300 K. δ is the donor–acceptor energy difference (in cm^{-1}). W_{d-d}, W_{d-m}, and W_{ex} are the dipole–dipole, dipole–multipole, and exchange rates (in s^{-1}), respectively. W and W^b are the forward and backward IET.

PATHWAY LABEL	DONOR	ACCEPTOR	δ	W_{d-d}	W_{d-m}	W_{ex}	W (FORWARD)	W^b (BACKWARD)
1	S_1	$^6H_{5/2}\rightarrow{}^4G_{5/2}$	7470	0.00E+00	0.00E+00	1.93E+07	1.93E+07	2.73E-13
2	S_1	$^6H_{5/2}\rightarrow{}^4G_{7/2}$	5340	1.19E+03	2.59E+03	1.13E+08	1.13E+08	7.48E-8
3	S_1	$^6H_{5/2}\rightarrow{}^4I_{9/2}$	4841	1.07E+03	2.76E+04	0.00E+00	2.87E+04	2.34E-10
4	S_1	$^6H_{5/2}\rightarrow{}^4M_{15/2}$	4676	2.27E+04	8.32E+00	0.00E+00	2.27E+04	4.28E-10
5	S_1	$^6H_{5/2}\rightarrow{}^4I_{11/2}$	4354	9.90E+03	3.62E+00	0.00E+00	9.90E+03	9.46E-10
6	S_1	$^6H_{5/2}\rightarrow{}^4I_{13/2}$	3857	3.00E+04	2.45E+02	0.00E+00	3.02E+04	3.55E-8
7	S_1	$^6H_{5/2}\rightarrow{}^4F_{5/2}$	3200	0.00E+00	0.00E+00	6.44E+08	6.44E+08	2.08E-2
8	S_1	$^6H_{5/2}\rightarrow{}^4M_{17/2}$	2889	1.09E+04	3.99E+00	0.00E+00	1.09E+04	1.69E-6
9	S_1	$^6H_{5/2}\rightarrow{}^4G_{9/2}$	2628	6.64E+03	1.24E+02	0.00E+00	6.76E+03	3.92E-6
10	S_1	$^6H_{5/2}\rightarrow{}^6P_{5/2}$	1369	2.18E+04	4.86E+03	0.00E+00	2.66E+04	8.86E-3
11	S_1	$^6H_{5/2}\rightarrow{}^4L_{13/2}$	825	4.13E+04	1.76E+03	0.00E+00	4.31E+04	2.23E-1
12	S_1	$^6H_{5/2}\rightarrow{}^4F_{7/2}$	506	3.05E+03	1.52E+04	0.00E+00	1.82E+04	4.73E-1
13	S_1	$^6H_{5/2}\rightarrow{}^6P_{3/2}$	437	1.65E+05	3.69E+04	0.00E+00	2.02E+05	7.43
14	S_1	$^6H_{5/2}\rightarrow{}^4K_{11/2}$	300	9.56E+03	9.47E+01	0.00E+00	9.66E+03	7.08E-1
15	S_1	$^6H_{5/2}\rightarrow{}^4L_{15/2}$	-166	2.15E+04	7.85E+00	0.00E+00	9.68E+03	1.65E+1
16	S_1	$^6H_{5/2}\rightarrow{}^4G_{11/2}$	-328	3.91E+03	2.42E+01	0.00E+00	8.16E+02	6.86
17	S_1	$^6H_{5/2}\rightarrow{}^6P_{7/2}$	-1285	2.26E+05	3.86E+02	0.00E+00		
						W_S	7.77×10^8	
						W_S^b		5.52×10^4
18	T_1	$^6H_{5/2}\rightarrow{}^4G_{5/2}$	3710	0.00	0.00	4.91E+8	4.91E+8	9.19
19	T_1	$^6H_{5/2}\rightarrow{}^4G_{7/2}$	1580	8.80E+1	1.92E+2	8.41E+8	8.41E+8	4.31E+5
20	T_1	$^6H_{5/2}\rightarrow{}^4I_{9/2}$	1081	5.96E+1	1.53E+3	0.00	1.59E+3	8.92
21	T_1	$^6H_{5/2}\rightarrow{}^4M_{15/2}$	916	1.15E+3	4.20E-1	0.00	1.15E+3	1.42E+1
22	T_1	$^6H_{5/2}\rightarrow{}^4I_{11/2}$	594	4.15E+2	1.52E-1	0.00	4.15E+2	2.40E+1
23	T_1	$^6H_{5/2}\rightarrow{}^4I_{13/2}$	97	9.42E+2	7.69	0.00	9.50E+2	5.97E+2
24	T_1	$^6H_{5/2}\rightarrow{}^4F_{5/2}$	-560	0.00	0.00	1.38E+9	9.43E+7	1.38E+9
25	T_1	$^6H_{5/2}\rightarrow{}^4M_{17/2}$	-871	1.96E+2	7.16E-2	0.00	3.00	1.96E+2
26	T_1	$^6H_{5/2}\rightarrow{}^4G_{9/2}$	-1132	1.02E+2	1.91	0.00	4.57E-1	1.04E+2
27	T_1	$^6H_{5/2}\rightarrow{}^6P_{5/2}$	-2391	1.62E+2	3.61E+1	0.00	2.07E-3	1.98E+2
28	T_1	$^6H_{5/2}\rightarrow{}^4L_{13/2}$	-2935	2.24E+2	9.54	0.00	1.80E-4	2.34E+2
29	T_1	$^6H_{5/2}\rightarrow{}^4F_{7/2}$	-3254	1.38E+1	6.85E+1	0.00	1.37E-5	8.23E+1
30	T_1	$^6H_{5/2}\rightarrow{}^6P_{3/2}$	-3323	7.17E+2	1.60E+2	0.00	1.05E-4	8.77E+2
31	T_1	$^6H_{5/2}\rightarrow{}^4K_{11/2}$	-3460	3.83E+1	3.79E-1	0.00	2.40E-6	3.87E+1
32	T_1	$^6H_{5/2}\rightarrow{}^4L_{15/2}$	-3926	6.56E+1	2.40E-2	0.00	4.36E-7	6.56E+1
33	T_1	$^6H_{5/2}\rightarrow{}^4G_{11/2}$	-4088	1.09E+1	6.74E-2	0.00	3.35E-8	1.10E+1
34	T_1	$^6H_{5/2}\rightarrow{}^6P_{7/2}$	-5045	3.61E+2	6.17E-1	0.00		
						W_T	1.43×10^9	
						W_T^b		1.38×10^9

Table S32. nha^{3-}-to-Tb^{3+} energy transfer rates at 300 K. δ is the donor–acceptor energy difference (in cm^{-1}). W_{d-d}, W_{d-m}, and W_{ex} are the dipole–dipole, dipole–multipole, and exchange rates (in s^{-1}), respectively. W and W^b are the forward and backward IET.

PATHWAY LABEL	DONOR	ACCEPTOR	δ	W_{d-d}	W_{d-m}	W_{ex}	W (FORWARD)	W^b (BACKWARD)
1	S_1	$^7F_6 \rightarrow {}^5D_4$	2956	4.59E+02	1.62E+04	0.00E+00	1.66E+04	1.16E-02
2	S_1	$^7F_6 \rightarrow {}^5D_3$	-2836	4.24E+02	1.19E+01	0.00E+00	5.40E-04	4.36E+02
3	S_1	$^7F_6 \rightarrow {}^5G_6$	-3023	3.13E+04	2.81E+04	6.37E+06		
4	S_1	$^7F_6 \rightarrow {}^5L_{10}$	-3571	1.17E+04	2.60E+01	0.00E+00		
5	S_1	$^7F_6 \rightarrow {}^5G_5$	-4367	1.71E+03	9.76E+03	1.40E+04		
6	S_1	$^7F_6 \rightarrow {}^5G_4$	-4887	7.53E+02	5.65E+02	0.00E+00		
7	S_1	$^7F_6 \rightarrow {}^5L_6$	-6210	0.00E+00	0.00E+00	1.72E+02		
8	S_1	$^7F_6 \rightarrow {}^5H_7$	-7979	0.00E+00	0.00E+00	3.09E+01		
9	S_1	$^7F_6 \rightarrow {}^5H_6$	-9491	0.00E+00	0.00E+00	2.63E+02		
10	S_1	$^7F_6 \rightarrow {}^5H_5$	-10367	0.00E+00	0.00E+00	8.39E-15		
11	S_1	$^7F_6 \rightarrow {}^5F_5$	-11534	0.00E+00	0.00E+00	4.04E+01		
12	S_1	$^7F_5 \rightarrow {}^5D_4$	5004	4.19E+02	8.58E+04	1.88E+04	1.05E+05	3.97E-06
13	S_1	$^7F_5 \rightarrow {}^5D_3$	-788	1.54E+03	2.01E+04	0.00E+00	4.95E+02	2.17E+04
14	S_1	$^7F_5 \rightarrow {}^5G_6$	-975	6.34E+03	1.55E+05	2.44E+05		
15	S_1	$^7F_5 \rightarrow {}^5L_{10}$	-1523	7.98E+02	9.61E-01	0.00E+00		
16	S_1	$^7F_5 \rightarrow {}^5G_5$	-2319	2.76E+03	2.77E+03	1.93E+06		
17	S_1	$^7F_5 \rightarrow {}^5G_4$	-2839	7.41E+02	1.12E+04	2.52E+04		
18	S_1	$^7F_5 \rightarrow {}^5L_6$	-4162	0.00E+00	0.00E+00	1.94E+01		
19	S_1	$^7F_5 \rightarrow {}^5H_6$	-7443	0.00E+00	0.00E+00	7.50E+01		
20	S_1	$^7F_5 \rightarrow {}^5H_5$	-8319	0.00E+00	0.00E+00	4.05E+03		
21	S_1	$^7F_5 \rightarrow {}^5F_5$	-9486	0.00E+00	0.00E+00	1.43E+03		
						W_S	1.22×10^5	
						W_S^b		2.21×10^4
22	T_1	$^7F_6 \rightarrow {}^5D_4$	-2294	6.00	2.12E+2	0.00	3.63E-3	2.18E+2
23	T_1	$^7F_6 \rightarrow {}^5D_3$	-8086	5.12E-2	1.44E-3	0.00	7.58E-19	5.26E-2
24	T_1	$^7F_6 \rightarrow {}^5G_6$	-8273	3.25	2.92	6.62E+4		
25	T_1	$^7F_6 \rightarrow {}^5L_{10}$	-8821	7.81E-1	1.73E-3	0.00		
26	T_1	$^7F_6 \rightarrow {}^5G_5$	-9617	6.00E-2	3.42E-1	4.90E+1		
27	T_1	$^7F_6 \rightarrow {}^5G_4$	-10137	1.73E-2	1.30E-2	0.00		
28	T_1	$^7F_6 \rightarrow {}^5L_6$	-11460	0.00	0.00	1.36E-1		
29	T_1	$^7F_6 \rightarrow {}^5H_7$	-13229	0.00	0.00	5.84E-3		
30	T_1	$^7F_6 \rightarrow {}^5H_6$	-14741	0.00	0.00	1.46E-2		
31	T_1	$^7F_6 \rightarrow {}^5H_5$	-15617	0.00	0.00	2.29E-19		
32	T_1	$^7F_6 \rightarrow {}^5F_5$	-16784	0.00	0.00	4.31E-4		
33	T_1	$^7F_5 \rightarrow {}^5D_4$	-246	2.43E+1	4.97E+3	1.29E+5	4.10E+4	1.34E+5
34	T_1	$^7F_5 \rightarrow {}^5D_3$	-6038	8.26E-1	1.08E+1	0.00	3.08E-12	1.16E+1
35	T_1	$^7F_5 \rightarrow {}^5G_6$	-6225	2.92	7.13E+1	1.33E+4		
36	T_1	$^7F_5 \rightarrow {}^5L_{10}$	-6773	2.36E-1	2.84E-4	0.00		
37	T_1	$^7F_5 \rightarrow {}^5G_5$	-7569	4.29E-1	4.29E-1	3.54E+4		
38	T_1	$^7F_5 \rightarrow {}^5G_4$	-8089	7.56E-2	1.14	3.04E+2		
39	T_1	$^7F_5 \rightarrow {}^5L_6$	-9412	0.00	0.00	8.01E-2		
40	T_1	$^7F_5 \rightarrow {}^5H_6$	-12693	0.00	0.00	2.18E-2		
41	T_1	$^7F_5 \rightarrow {}^5H_5$	-13569	0.00	0.00	5.80E-1		
42	T_1	$^7F_5 \rightarrow {}^5F_5$	-14736	0.00	0.00	7.98E-2		
						W_T	4.10×10^4	
						W_T^b		1.34×10^5

Table S33. nha^{3-}-to-Sm^{3+} energy transfer rates at 300 K. δ is the donor–acceptor energy difference (in cm^{-1}). W_{d-d}, W_{d-m}, and W_{ex} are the dipole–dipole, dipole–multipole, and exchange rates (in s^{-1}), respectively. W and W^b are the forward and backward IET.

PATHWAY LABEL	DONOR	ACCEPTOR	δ	W_{d-d}	W_{d-m}	W_{ex}	W (FORWARD)	W^b (BACKWARD)
1	S_1	$^6H_{5/2}\rightarrow{}^4G_{5/2}$	5470	0.00E+00	0.00E+00	1.41E+08	1.41E+08	5.72E-04
2	S_1	$^6H_{5/2}\rightarrow{}^4G_{7/2}$	3340	4.52E+03	9.84E+03	4.32E+08	4.32E+08	4.77E+01
3	S_1	$^6H_{5/2}\rightarrow{}^4I_{9/2}$	2841	3.50E+03	9.01E+04	0.00E+00	9.36E+04	1.13E-01
4	S_1	$^6H_{5/2}\rightarrow{}^4M_{15/2}$	2676	7.06E+04	2.58E+01	0.00E+00	7.06E+04	1.88E-01
5	S_1	$^6H_{5/2}\rightarrow{}^4I_{11/2}$	2354	2.78E+04	1.02E+01	0.00E+00	2.78E+04	3.48E-01
6	S_1	$^6H_{5/2}\rightarrow{}^4I_{13/2}$	1857	7.23E+04	5.90E+02	0.00E+00	7.29E+04	9.88E+00
7	S_1	$^6H_{5/2}\rightarrow{}^4F_{5/2}$	1200	0.00E+00	0.00E+00	1.27E+09	1.27E+09	4.01E+06
8	S_1	$^6H_{5/2}\rightarrow{}^4M_{17/2}$	889	1.95E+04	7.14E+00	0.00E+00	1.95E+04	2.75E+02
9	S_1	$^6H_{5/2}\rightarrow{}^4G_{9/2}$	628	1.10E+04	2.04E+02	0.00E+00	1.12E+04	5.49E+02
10	S_1	$^6H_{5/2}\rightarrow{}^6P_{5/2}$	-631	2.44E+04	5.44E+03	0.00E+00	1.45E+03	2.98E+04
11	S_1	$^6H_{5/2}\rightarrow{}^4L_{13/2}$	-1175	3.92E+04	1.67E+03	0.00E+00		
12	S_1	$^6H_{5/2}\rightarrow{}^4F_{7/2}$	-1494	2.62E+03	1.30E+04	0.00E+00		
13	S_1	$^6H_{5/2}\rightarrow{}^6P_{3/2}$	-1563	1.39E+05	3.11E+04	0.00E+00		
14	S_1	$^6H_{5/2}\rightarrow{}^4K_{11/2}$	-1700	7.71E+03	7.63E+01	0.00E+00		
15	S_1	$^6H_{5/2}\rightarrow{}^4L_{15/2}$	-2166	1.50E+04	5.48E+00	0.00E+00		
16	S_1	$^6H_{5/2}\rightarrow{}^4G_{11/2}$	-2328	2.60E+03	1.61E+01	0.00E+00		
17	S_1	$^6H_{5/2}\rightarrow{}^6P_{7/2}$	-3285	1.12E+05	1.91E+02	0.00E+00		
						W_S	1.84×10^9	
						W_S^b		4.04×10^6
18	T_1	$^6H_{5/2}\rightarrow{}^4G_{5/2}$	220	0.00	0.00	1.41E+9	1.41E+9	4.91E+8
19	T_1	$^6H_{5/2}\rightarrow{}^4G_{7/2}$	-1910	8.06E+1	1.75E+2	7.70E+8	8.10E+4	7.70E+8
20	T_1	$^6H_{5/2}\rightarrow{}^4I_{9/2}$	-2409	4.17E+1	1.07E+3	0.00	1.07E-2	1.11E+3
21	T_1	$^6H_{5/2}\rightarrow{}^4M_{15/2}$	-2574	7.35E+2	2.69E-1	0.00	3.20E-3	7.36E+2
22	T_1	$^6H_{5/2}\rightarrow{}^4I_{11/2}$	-2896	2.23E+2	8.17E-2	0.00	2.08E-4	2.24E+2
23	T_1	$^6H_{5/2}\rightarrow{}^4I_{13/2}$	-3393	3.89E+2	3.17	0.00	3.36E-5	3.92E+2
24	T_1	$^6H_{5/2}\rightarrow{}^4F_{5/2}$	-4050	0.00	0.00	4.00E+8	1.47	4.00E+8
25	T_1	$^6H_{5/2}\rightarrow{}^4M_{17/2}$	-4361	4.79E+1	1.75E-2	0.00	3.96E-8	4.80E+1
26	T_1	$^6H_{5/2}\rightarrow{}^4G_{9/2}$	-4622	2.18E+1	4.07E-1	0.00	5.24E-9	2.22E+1
27	T_1	$^6H_{5/2}\rightarrow{}^6P_{5/2}$	-5881	1.75E+1	3.91	0.00	1.21E-11	2.14E+1
28	T_1	$^6H_{5/2}\rightarrow{}^4L_{13/2}$	-6425	1.81E+1	7.71E-1	0.00		
29	T_1	$^6H_{5/2}\rightarrow{}^4F_{7/2}$	-6744	9.37E-1	4.66	0.00		
30	T_1	$^6H_{5/2}\rightarrow{}^6P_{3/2}$	-6813	4.70E+1	1.05E+1	0.00		
31	T_1	$^6H_{5/2}\rightarrow{}^4K_{11/2}$	-6950	2.33	2.31E-2	0.00		
32	T_1	$^6H_{5/2}\rightarrow{}^4L_{15/2}$	-7416	3.11	1.14E-3	0.00		
33	T_1	$^6H_{5/2}\rightarrow{}^4G_{11/2}$	-7578	4.73E-1	2.93E-3	0.00		
34	T_1	$^6H_{5/2}\rightarrow{}^6P_{7/2}$	-8535	9.37	1.60E-2	0.00		
						W_T	1.41×10^9	
						W_T^b		1.66×10^9

Table S34. **Tb^{3+}-to-Sm^{3+}** energy transfer rates (s^{-1}) at 300 K considering the crystallographic closest distance $R_L = 7$ Å. δ is the donor–acceptor energy difference (in cm^{-1}). W is the sum over all mechanisms considering the barrier factor (if applicable). One should notice that the energy transfer $Tb^{3+}[^5D_4 \rightarrow {}^7F_6] \rightarrow Sm^{3+}[^6H_{5/2} \rightarrow {}^4I_{9/2}]$ has the highest contribution (pathway 4, highlighted in bold).

pathway Label	Donor ($^5D_4 \rightarrow$)	Acceptor ($^6H_{5/2} \rightarrow$)	δ	W_{d-d}	W_{d-q}	W_{q-q}	W
1	$^7F_6$	$^4G_{5/2}$	2514	0	0	0	1.04E-14
2	$^7F_6$	$^4F_{3/2}$	1563	0	0	0	4.62E-11
3	$^7F_6$	$^4G_{7/2}$	384	8.02E-04	2.14E-02	3.11E-01	3.33E-01
4	**$^7F_6$**	**$^4I_{9/2}$**	**-115**	**6.56E-04**	**3.27E-02**	**3.05**	**1.78**
5	$^7F_6$	$^4M_{15/2}$	-280	1.07E-02	2.63E-01	0	7.14E-02
6	$^7F_6$	$^4I_{11/2}$	-602	2.01E-03	4.95E-02	0	2.87E-03
7	$^7F_6$	$^4I_{13/2}$	-1099	7.13E-04	1.75E-02	0	9.38E-05
8	$^7F_6$	$^4F_{5/2}$	-1756	0	0	0	2.54E-15
9	$^7F_6$	$^4M_{17/2}$	-2067	2.05E-07	5.05E-06	0	2.60E-10
10	$^7F_6$	$^4G_{9/2}$	-2328	9.32E-09	2.29E-07	0	3.38E-12
11	$^7F_6$	$^4I_{15/2}$	-2503	0	0	0	7.17E-20
12	$^7F_6$	$^6P_{5/2}$	-3587	2.05E-15	5.04E-14	0	1.77E-21
13	$^7F_6$	$^4M_{19/2}$	-3593	0	0	0	2.16E-28
14	$^7F_5$	$^4G_{5/2}$	466	0	0	0	5.73E-09
15	$^7F_5$	$^4F_{3/2}$	-485	0	0	0	5.38E-10
16	$^7F_5$	$^4G_{7/2}$	-1664	7.46E-06	1.08E-03	1.68E-02	6.11E-06
17	$^7F_5$	$^4I_{9/2}$	-2163	7.29E-08	1.22E-05	1.97E-03	6.18E-08
18	$^7F_5$	$^4M_{15/2}$	-2328	2.75E-07	3.92E-05	0	5.59E-10
19	$^7F_5$	$^4I_{11/2}$	-2650	2.97E-09	4.24E-07	0	1.29E-12
20	$^7F_5$	$^4I_{13/2}$	-3147	1.28E-11	1.83E-09	0	5.13E-16
21	$^7F_5$	$^4F_{5/2}$	-3804	0	0	0	2.67E-30
22	$^7F_5$	$^4M_{17/2}$	-4115	6.86E-19	9.79E-17	0	2.65E-25
23	$^7F_5$	$^4G_{9/2}$	-4376	3.08E-21	4.39E-19	0	3.39E-28
24	$^7F_5$	$^4I_{15/2}$	-4551	0	0	0	9.99E-38
25	$^7F_5$	$^6P_{5/2}$	-5635	9.54E-33	1.36E-30	0	2.51E-42
26	$^7F_5$	$^4M_{19/2}$	-5641	0	0	0	1.90E-50
27	$^7F_4$	$^4G_{5/2}$	-801	0	0	0	4.90E-11
28	$^7F_4$	$^4F_{3/2}$	-1752	0	0	0	2.67E-15
29	$^7F_4$	$^4G_{7/2}$	-2931	1.16E-11	7.45E-11	7.88E-10	6.87E-16
30	$^7F_4$	$^4I_{9/2}$	-3430	7.32E-15	2.17E-13	5.97E-12	4.44E-19
31	$^7F_4$	$^4M_{15/2}$	-3595	1.12E-14	4.81E-14	0	1.93E-21
32	$^7F_4$	$^4I_{11/2}$	-3917	2.06E-17	8.88E-17	0	7.60E-25
33	$^7F_4$	$^4I_{13/2}$	-4414	5.80E-21	2.50E-20	0	1.97E-29
34	$^7F_4$	$^4F_{5/2}$	-5071	0	0	0	1.62E-43
35	$^7F_4$	$^4M_{17/2}$	-5382	1.53E-30	6.61E-30	0	5.02E-41
36	$^7F_4$	$^4G_{9/2}$	-5643	1.64E-33	7.07E-33	0	1.54E-44
37	$^7F_4$	$^4I_{15/2}$	-5818	0	0	0	1.00E-52
38	$^7F_4$	$^6P_{5/2}$	-6902	5.07E-48	2.19E-47	0	1.13E-61
39	$^7F_4$	$^4M_{19/2}$	-6908	0	0	0	4.82E-68
						$W_{total} = \sum W$	**2.18**

To avoid a very large number of tables with all IET pathways for each temperature, **Table S35** summarizes the W_S, W_S^b, W_T, and W_T^b values (or range of calculated values). **Figure S33** shows the relevant rates for each Ln-based MC.

Table S35. Calculated forward and backward IET rates (in s^{-1}) via S_1 and T_1 for the studied $Ln_2L'_8$ MCs. For the quantities which present temperature dependence, the first number corresponds to the rate at 11 K while the last corresponds to the rate at 425 K.

Ln	L'	W_S	W_S^b	W_T	W_T^b
Tb	shi^{3-}	7.78×10^{6}	$6.43\times10^{3} - 7.22\times10^{3}$	5.01×10^{4}	4.00×10^{6}
	$mshi^{3-}$	1.10×10^{7}	$3.08\times10^{3} - 1.97\times10^{4}$	6.20×10^{4}	3.03×10^{6}
	$moshi^{3-}$	1.56×10^{7}	$1.15\times10^{5} - 1.81\times10^{6}$	5.99×10^{4}	3.19×10^{6}
	nha^{3-}	$3.27\times10^{6} - 1.23\times10^{7}$	$1.31\times10^{7} - 1.36\times10^{7}$	$10^{-9} - 5.81\times10^{4}$	2.49×10^{5}
Sm	shi^{3-}	2.73×10^{7}	$0 - 1.42\times10^{1}$	$1.17\times10^{9} - 1.84\times10^{9}$	1.41×10^{9}
	$mshi^{3-}$	6.65×10^{7}	$0 - 3.30\times10^{2}$	$1.37\times10^{9} - 1.53\times10^{9}$	1.37×10^{9}
	$moshi^{3-}$	2.63×10^{8}	$0 - 8.02\times10^{4}$	$1.33\times10^{9} - 1.54\times10^{9}$	1.38×10^{9}
	nha^{3-}	4.41×10^{8}	$0 - 4.71\times10^{3}$	1.41×10^{9}	$1.17\times10^{9} - 1.84\times10^{9}$

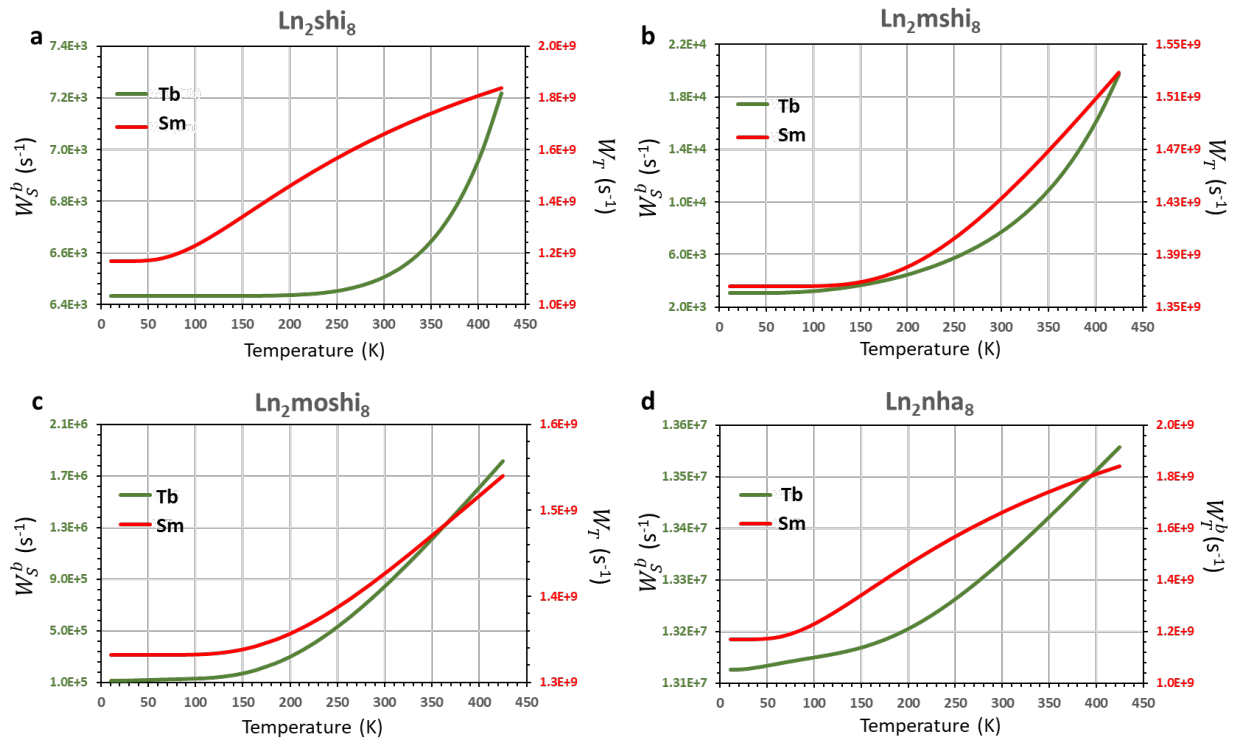

Figure S33. Temperature-dependent behavior for the relevant IET rates for $Ln_2L'_8$ MCs with L' = shi^{3-} (a), L' = $mshi^{3-}$ (b), L' = $moshi^{3-}$ (c), and L' = nha^{3-} (d). The left-side axis corresponds to the $Tb_2L'_8$ (green curves) while the right one is for the $Sm_2L'_8$ (red curves) MCs. Only the most relevant temperature-dependent rates are displayed. See **Table S35** for further details.

All forward rates via S_1 (W_S) for $Sm_2L'_8$ MCs are orders of magnitudes higher than the backward ones (W_S^b) while the rates via T_1 are in the same order of magnitude $W_T \approx W_T^b$. These circumstances imply the presence of a population equilibrium between the emitting Sm^{3+} $^4G_{5/2}$ and the T_1 levels, and once they have similar decay lifetimes (in the order of milliseconds), the emission of Sm^{3+} is dependent on its intrinsic lifetime.

For the $Tb_2L'_8$ MCs, we observed the trend $W_T^b > W_T$ for any case and, specifically, the Tb_2moshi_8 also presents a higher backward energy transfer via S_1, $W_S^b > W_S$. This means that the luminescence of Tb_2moshi_8 is very dependent on the S_1 and T_1 lifetimes.

In addition, the Tb_2moshi_8 is a special case, presenting the smaller energy gap between S_1 and T_1 states (ΔE_{S-T} = 3760 cm^{-1}) among the other MCs (ΔE_{S-T} > 5200 cm^{-1}). This may allow the up-conversion (or reverse) intersystem crossing (UISC or rISC) rates which is a thermally-activated energy transfer from the T_1 to the S_1 states [30,31]. Thus, based on Fermi's golden rule, we can estimate this quantity as [32]:

$$W_{rISC} = \frac{2\pi}{\hbar}|\langle S_1|H_{SO}|T_1\rangle|^2 \rho_{FC} \qquad \textbf{eqn S17}$$

where $\langle S_1|H_{SO}|T_1\rangle$ is the spin-orbit coupling matrix element and expresses the magnitude of the spin–orbit interaction between S_1 and T_1 states. ρ_{FC} is the Franck–Condon-weighted density of states, which in the context of Marcus–Levich–Jortner theory, can be estimated by [30,32,33]:

$$\rho_{FC} = \frac{1}{\sqrt{4\pi\lambda_M k_B T}} \sum_{n=0}^{\infty} e^{-S} \frac{S^n}{n!} e^{-\left[\frac{(\Delta E_{S-T} + n\hbar\omega + \lambda_M)^2}{4\lambda_M k_B T}\right]} \quad \textbf{eqn S18}$$

where $\hbar\omega$, S, and λ_M are the energy of high-frequency intramolecular vibrations, the Huang–Rhys factors (the average number of phonons produced by a vertical transition, related to the $\hbar\omega$ mode), and the reorganization energy induced by the energy transfer (also called Marcus reorganization energy). For the pursuit of simplification, we considered only the first term of this summation ($n = 0$), leading to:

$$W_{rISC} = \frac{2\pi}{\hbar} |\langle S_1 | H_{SO} | T_1 \rangle|^2 \frac{1}{\sqrt{4\pi\lambda_M k_B T}} e^{-\left[\frac{(\Delta E_{S-T} + \lambda_M)^2}{4\lambda_M k_B T} + S\right]} \quad \textbf{eqn S19}$$

We estimated the W_{rISC} (**Figure S34**) using the values $|\langle S_1 | H_{SO} | T_1 \rangle| = 0.16$ cm^{-1}, $S = 5$, and $\lambda_M = 0.124$ eV $\cong 1000$ cm^{-1}. This will lead to different population kinetics as a function of the temperature, as we will present in the next section.

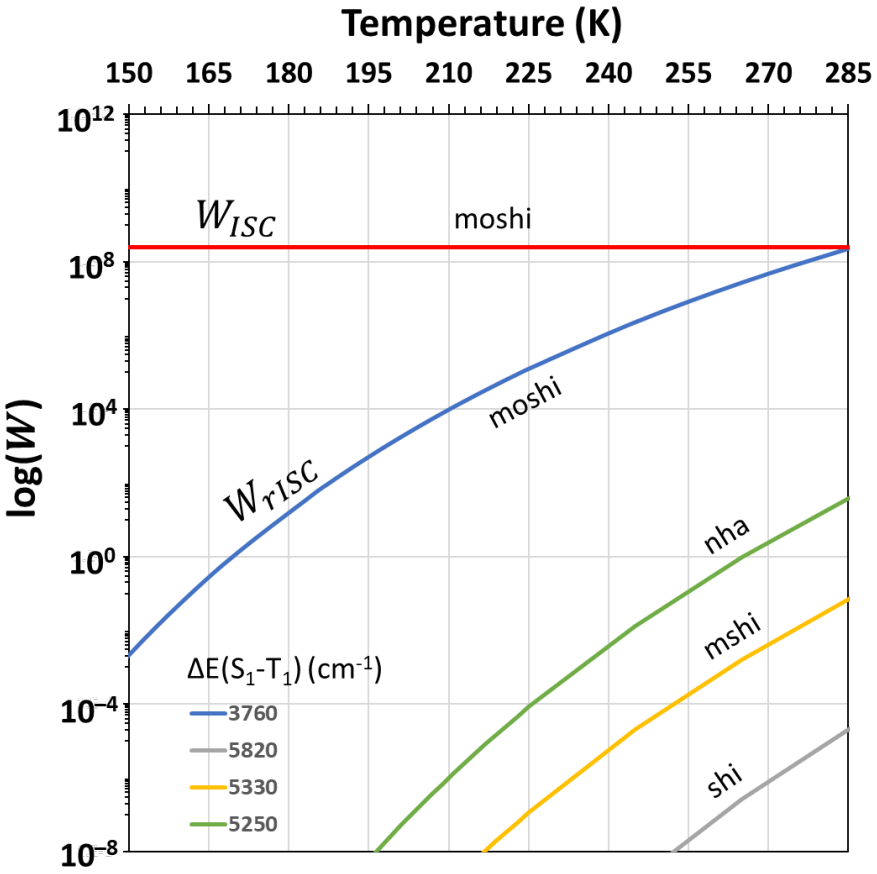

Figure S34. Log scale of the direct (red line) and reverse (curved lines) ISC rates as a function of the temperature for $Ln_2L'_8$ MCs. For the Ln_2moshi_8, the W_{ISC} is considered as being constant (2.5×10^8 s^{-1}) for any temperature while the W_{rISC} reached 2.5×10^8 s^{-1} from temperatures that are higher than 285 K. For the other $Ln_2L'_8$ MCs (L' = nha^{3-}, mshi^{3-}, and shi^{3-}), the W_{rISC} can be negligible due to high values of ΔE_{S-T}.

7.2 Populations rate equations

The kinetics of the IET process includes an equilibrium between the rates of absorption, IET (both forward and backward energy transfer) rates, radiative and non-radiative decay rates. This kinetics can be defined by an appropriate set of ordinary differential equations (ODEs). However, sometimes it is difficult to describe and include the population of all levels of the Ln^{3+} ion. To simplify the setup of the rate equations, groups of levels will be represented by |n⟩ (as depicted in **Figure 8**) and their respective populations as P_n. Thus, based on the IET rates and the schematic energy level diagram, a 5-level set of ODEs with initial conditions (when t = 0 s) is given by:

ODE	Initial condition	Level (or Levels)	
$\frac{d}{dt}P_0(t) = -\phi P_0(t) + \frac{1}{\tau_T}P_1(t) + \frac{1}{\tau_S}P_2(t) + \frac{1}{\tau}P_4(t)$	$P_0(0) = 1$	S_0 and Ln^{3+} ground levels	**eqn S20**
$\frac{d}{dt}P_1(t) = -\left(\frac{1}{\tau_T} + W_T + W_{rISC}\right)P_1(t) + W_{ISC}P_2(t) + W_T^b P_3(t)$	$P_1(0) = 0$	T_1	**eqn S21**
$\frac{d}{dt}P_2(t) = -\left(\frac{1}{\tau_S} + W_{ISC} + W_S\right)P_2(t) + \phi P_0(t) + W_S^b P_3(t) + W_{rISC}P_1(t)$	$P_2(0) = 0$	S_1	**eqn S22**
$\frac{d}{dt}P_3(t) = -(W_{3\to4} + W_T^b + W_S^b)P_3(t) + W_S P_2(t)$	$P_3(0) = 0$	$^5D_3$ to $^5F_5$ (Tb^{3+}) $^4F_{3/2}$ to $^6P_{7/2}$ (Sm^{3+})	**eqn S23**
$\frac{d}{dt}P_4(t) = -\left(\frac{1}{\tau}\right)P_4(t) + W_{3\to4}P_3(t) + W_T P_1(t)$	$P_4(0) = 0$	$^5D_4$ (Tb^{3+}) $^4G_{5/2}$ (Sm^{3+})	**eqn S24**

where τ_T ($\sim 10^{-3}$s), τ_S ($\sim 10^{-9}$s), and τ (see **Table 1**) are the lifetimes of the T_1, S_1, and emitting levels ($^4G_{5/2}$ and $^5D_4$), respectively. W_{ISC} and W_{rISC} are the intersystem crossing rate $S_1 \rightarrow T_1$ and the reversed one $T_1 \rightarrow S_1$, which are both sensitive to the energy gap between the S_1 and T_1 states ΔE_{S-T} [30,31,34] and such an energy gap around 5200–5800 cm^{-1} (for MCs with shi, mshi, and nha) may lead to a reasonable value of $W_{ISC} \sim 10^6$ s^{-1} whereas the $W_{rISC} \sim 0$ s^{-1} [35,36]. Due to its small ΔE_{S-T}, only the Ln_2moshi$_8$ presented relevant W_{rISC} rates, as discussed before. $W_{3\to4}$ is the nonradiative energy decay from the upper levels of Ln^{3+} to the emitting ones ($^5D_4$ and $^4G_{5/2}$) that is in the order of $\sim 10^6$ s^{-1} for Ln^{3+} chelates.[9]

The pumping rate $\phi \sim 10^2$ s^{-1} was estimated using

$$\phi = \frac{\sigma \rho \lambda_{exc}}{hc} \qquad \textbf{eqn S25}$$

where σ ($\sim 10^{-16}$ cm^2) is the typical average absorption cross-section of the organic sensitizers, ρ ($\sim$ 1 W/cm^{-2}) is the power density of the excitation source at λ_{exc} = 340, 350, 370, and 380 nm for shi, mshi, moshi, and nha Ln-based MCs, respectively. If the power density is increased (*e.g.* $\rho = 10$ W/cm^{-2}, leading to $\phi \sim 10^3\ s^{-1}$), it will reflect in a higher depopulation of the ground-level (P_0, **eqn S20**) and increasing mainly the populations in the T_1 and Ln^{3+} emitting levels. Thus, to standardize our population analysis, we adopt the value of $\rho = 1$ W/cm^{-2} for all simulations. The ODEs (**eqns S20**–**S24**) were numerically solved using the Radau method.[37]

As an example, **Figure S35** shows the transient behavior of the population fractions of the Tb^{3+} $^5D_4$ excited level vs. the temperature for the Tb_2moshi_8. In this specific case, each curve represents a fixed temperature, and it is observed a strong tendency in decreasing the Tb^{3+} $^5D_4$ population due to the competition between W_T and W_{rISC}. Thus, at lower temperatures, we have $W_T > W_{rISC}$. The W_{rISC} becomes dominating at temperatures above 220 K and this promotes a fast depopulation of the Tb^{3+} $^5D_4$ level, quenching the emission signal arising from the $^5D_4 \rightarrow {}^7F_J$ transition, as we observed in the temperature-dependent emission spectra (**Figure S21**). **Table S36** shows the populations in the steady-state regime (when $\frac{d}{dt}P_4(t) = 0$) for all samples in this work.

Table S36. Values for the emitting level population fraction P_4 (in 10^{-3}) for all studied $Ln_2L'_8$ MCs .

	Ln = Tb^{3+}				**Ln = Sm^{3+}**			
T (K)	L' = shi^{3-}	$mshi^{3-}$	$moshi^{3-}$	nha^{3-}	L' = shi^{3-}	$mshi^{3-}$	$moshi^{3-}$	nha^{3-}
11	1.92	2.77	3.84	0.05	0.58	0.90	5.24	2.06
25	1.92	2.77	3.84	0.06	0.58	0.90	5.24	1.82
45	1.92	2.77	3.84	0.08	0.58	0.90	5.24	1.76
65	1.92	2.77	3.84	0.21	0.58	0.90	5.24	1.71
85	1.92	2.77	3.84	0.35	0.58	0.90	5.24	1.59
105	1.92	2.77	3.84	0.42	0.58	0.90	5.24	1.47
125	1.92	2.77	3.76	0.46	0.58	0.90	5.24	1.29
145	1.92	2.77	3.61	0.49	0.58	0.90	5.24	1.18
165	1.92	2.77	3.45	0.51	0.58	0.90	5.24	1.06
185	1.92	2.77	3.26	0.52	0.58	0.90	5.24	0.88
205	1.92	2.77	2.93	0.54	0.58	0.90	5.24	0.65
225	1.90	2.55	1.15	0.55	0.58	0.90	5.24	0.53
245	1.87	2.11	0.13	0.56	0.58	0.90	5.23	0.29
265	1.85	2.05	0.05	0.56	0.58	0.90	5.17	0.18
285	1.82	2.00	0.04	0.57	0.58	0.90	4.74	0.12
305	1.79	1.94	0.04	0.58	0.58	0.90	4.74	0.06
325	1.77	1.89	0.04	0.58	0.58	0.90	4.74	0.06
345	1.74	1.83	0.04	0.59	0.58	0.90	4.74	0.06
365	1.72	1.77	0.04	0.59	0.58	0.90	4.74	0.06
385	1.69	1.72	0.04	0.59	0.58	0.90	4.74	0.06
405	1.67	1.66	0.04	0.60	0.58	0.90	4.74	0.06
425	1.64	1.62	0.13	0.60	0.58	0.90	4.74	0.06

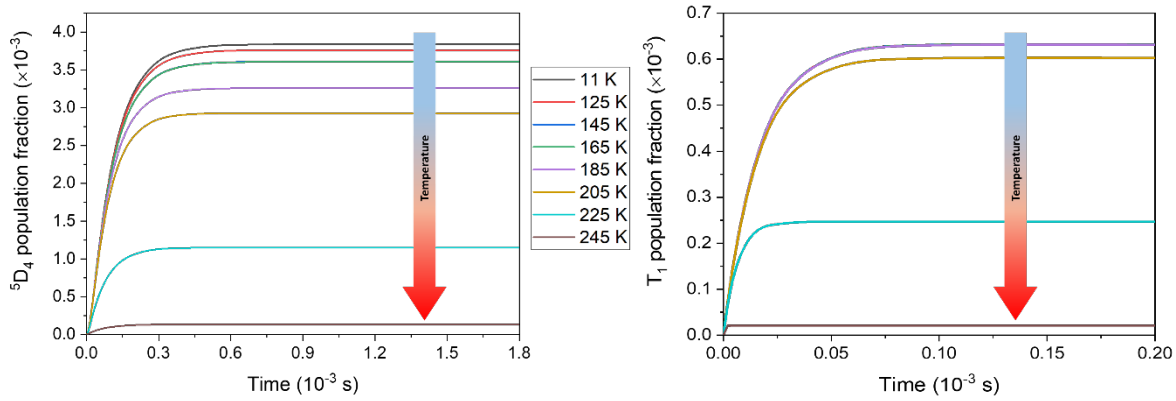

Figure S35. Transient curves of the Tb^{3+} $^5D_4$ emitting level (left panel) and T_1 (right panel) population fractions as a function of the time when the temperature is increased (from top to bottom) for the Tb_2moshi_8 MC.

7.3 Radiative rates and thermometric parameter

Once the theoretical intensity parameters Ω_λ were determined (see section *6.1 Theoretical intensity parameters*), it is possible to calculate the individual radiative rate $A_{J\to J'}$:

$$A_{J\to J'} = \frac{4e^2(\omega_{J\to J'})^3}{3\hbar c^3(2J+1)}\left[\frac{n(n^2+2)^2}{9}S_{ed} + n^3 S_{md}\right] \qquad \textbf{eqn S26}$$

where,

$$S_{ed} = \sum_{\lambda=2,4,6} \Omega_\lambda \langle l^N \psi J \| U^{(\lambda)} \| l^N \psi' J' \rangle^2 \qquad \textbf{eqn S27}$$

$$S_{md} = \frac{\hbar}{4m_e^2 c^2}\langle l^N \psi J \| L + 2S \| l^N \psi' J' \rangle^2 \qquad \textbf{eqn S28}$$

are the electric and magnetic dipole strength, respectively. The squared matrix elements $\langle l^N \psi J \| U^{(\lambda)} \| l^N \psi' J' \rangle^2$ can be found in Ref. [38] and the $\langle l^N \psi J \| L + 2S \| l^N \psi' J' \rangle$ for the Tb^{3+} $^5D_4 \to {}^7F_5$ can be calculated from the date in Ref. [27]. Due to the selection rules on J quantum number, the $\langle l^N \psi J \| L + 2S \| l^N \psi' J' \rangle$ matrix elements for the Tb^{3+} $^5D_4 \to {}^7F_6$ and Sm^{3+} $^4G_{5/2} \to {}^6H_{9/2}$ are equal to zero. The ω is the angular frequency of the transition $|l^N \psi J\rangle \to |l^N \psi' J'\rangle$, m_e is the electron mass, n is the refractive index of the medium (we consider equal to 1.5). The set of radiative rates obtained are: $A_{4\to 6} = 140\ s^{-1}$ ($^5D_4 \to {}^7F_6$); $A_{4\to 5} = 304\ s^{-1}$ ($^5D_4 \to {}^7F_5$); $A_{4\to 3} = 77\ s^{-1}$ ($^5D_4 \to {}^7F_3$); and $A_{5/2\to 9/2} = 35\ s^{-1}$ ($^4G_{5/2} \to {}^6H_{9/2}$).

The emissions of interest may be calculated by:

$$I_{J\to J'} = A_{J\to J'} P_4 \qquad \textbf{eqn S29}$$

using the values of the emitting levels populations P_4 (in the steady-state regime) (**Table S36**), we can estimate the intensities I_{Eu} and I_{Tb} and, subsequently, the theoretical thermometric parameter $\Delta = \frac{I_{Tb}}{I_{Eu}}$. Thus,

$$\Delta = \frac{I_{Tb}\left({}^5\mathrm{D}_4 \rightarrow {}^7\mathrm{F}_{J'}\right)}{I_{Sm}\left({}^4\mathrm{G}_{5/2} \rightarrow {}^6\mathrm{H}_{9/2}\right)} = \frac{A_{4\rightarrow J}}{A_{5/2\rightarrow 9/2}}\left(\frac{P_4(Tb)}{P_4(Sm)}\right) \qquad \textbf{eqn S30}$$

$$\Delta = \frac{\frac{4e^2\left(\omega_{4\rightarrow J'}\right)^3}{3\hbar c^3(8+1)}\left[\frac{n(n^2+2)^2}{9}\sum_{\lambda=2,4,6}\Omega_\lambda\left\langle {}^5\mathrm{D}_4\middle\|U^{(\lambda)}\middle\|{}^7\mathrm{F}_{J'}\right\rangle^2 + n^3 S_{md}\right]}{\frac{4e^2\left(\omega_{5/2\rightarrow 9/2}\right)^3}{3\hbar c^3(5+1)}\left[\frac{n(n^2+2)^2}{9}\sum_{\lambda'=2,4,6}\Omega_{\lambda'}\left\langle {}^4\mathrm{G}_{5/2}\middle\|U^{(\lambda')}\middle\|{}^6\mathrm{H}_{9/2}\right\rangle^2 + n^3 \underbrace{S_{md}}_{=0}\right]} \times \left(\frac{P_4(Tb)}{P_4(Sm)}\right) \qquad \textbf{eqn S31}$$

$$\Delta = \frac{2}{3}\left(\frac{\omega_{4\rightarrow J'}}{\omega_{5/2\rightarrow 9/2}}\right)^3 \frac{\left[n(n^2+2)^2\sum_{\lambda=2,4,6}\Omega_\lambda\left\langle {}^5\mathrm{D}_4\middle\|U^{(\lambda)}\middle\|{}^7\mathrm{F}_{J'}\right\rangle^2 + 9n^3 S_{md}\right]}{\left[n(n^2+2)^2\sum_{\lambda'=2,4,6}\Omega_{\lambda'}\left\langle {}^4\mathrm{G}_{5/2}\middle\|U^{(\lambda')}\middle\|{}^6\mathrm{H}_{9/2}\right\rangle^2\right]} \times \left(\frac{P_4(Tb)}{P_4(Sm)}\right) \qquad \textbf{eqn S32}$$

$$\Delta = \frac{2}{3}\left(\frac{\omega_{4\rightarrow J'}}{\omega_{5/2\rightarrow 9/2}}\right)^3 \left(\frac{\sum_{\lambda=2,4,6}\Omega_\lambda\left\langle {}^5\mathrm{D}_4\middle\|U^{(\lambda)}\middle\|{}^7\mathrm{F}_{J'}\right\rangle^2}{\sum_{\lambda'=2,4,6}\Omega_{\lambda'}\left\langle {}^4\mathrm{G}_{5/2}\middle\|U^{(\lambda')}\middle\|{}^6\mathrm{H}_{9/2}\right\rangle^2} + \frac{9n^2\hbar\left\langle {}^5\mathrm{D}_4\middle\|L+2S\middle\|{}^7\mathrm{F}_{J'}\right\rangle^2}{4m_e^2c^2(n^2+2)^2\sum_{\lambda'=2,4,6}\Omega_{\lambda'}\left\langle {}^4\mathrm{G}_{5/2}\middle\|U^{(\lambda')}\middle\|{}^6\mathrm{H}_{9/2}\right\rangle^2}\right) \times \left(\frac{P_4(Tb)}{P_4(Sm)}\right) \qquad \textbf{eqn S33}$$

eqn S33 may be simplified once all terms before the population ratio $\left(\frac{P_4(Tb)}{P_4(Sm)}\right)$, a priori, does not depend on the temperature, unless the Ln^{3+} occupies a center of inversion [25]. However, depending on the Tb^{3+} ${}^5\mathrm{D}_4 \rightarrow {}^7\mathrm{F}_{J'}$ transition (the choice of J'), three thermometric parameters can be derived from ***eqn S33***:

$$\Delta_1 = \frac{2}{3}\left(\frac{\omega_{4\rightarrow 6}}{\omega_{5/2\rightarrow 9/2}}\right)^3 \left(\frac{\sum_{\lambda=2,4,6}\Omega_\lambda\left\langle {}^5\mathrm{D}_4\middle\|U^{(\lambda)}\middle\|{}^7\mathrm{F}_6\right\rangle^2}{\sum_{\lambda'=2,4,6}\Omega_{\lambda'}\left\langle {}^4\mathrm{G}_{5/2}\middle\|U^{(\lambda')}\middle\|{}^6\mathrm{H}_{9/2}\right\rangle^2}\right) \times \left(\frac{P_4(Tb)}{P_4(Sm)}\right) \qquad \textbf{eqn S34}$$

$$\Delta_2 = \frac{2}{3}\left(\frac{\omega_{4\rightarrow 5}}{\omega_{5/2\rightarrow 9/2}}\right)^3 \left(\frac{\sum_{\lambda=2,4,6}\Omega_\lambda\left\langle {}^5\mathrm{D}_4\middle\|U^{(\lambda)}\middle\|{}^7\mathrm{F}_5\right\rangle^2}{\sum_{\lambda'=2,4,6}\Omega_{\lambda'}\left\langle {}^4\mathrm{G}_{5/2}\middle\|U^{(\lambda')}\middle\|{}^6\mathrm{H}_{9/2}\right\rangle^2} + \frac{9n^2\hbar\left\langle {}^5\mathrm{D}_4\middle\|L+2S\middle\|{}^7\mathrm{F}_5\right\rangle^2}{4m_e^2c^2(n^2+2)^2\sum_{\lambda'=2,4,6}\Omega_{\lambda'}\left\langle {}^4\mathrm{G}_{5/2}\middle\|U^{(\lambda')}\middle\|{}^6\mathrm{H}_{9/2}\right\rangle^2}\right) \times \left(\frac{P_4(Tb)}{P_4(Sm)}\right) \qquad \textbf{eqn S35}$$

$$\Delta_3 = \frac{2}{3}\left(\frac{\omega_{4\rightarrow 3}}{\omega_{5/2\rightarrow 9/2}}\right)^3 \left(\frac{\sum_{\lambda=2,4,6}\Omega_\lambda\left\langle {}^5\mathrm{D}_4\middle\|U^{(\lambda)}\middle\|{}^7\mathrm{F}_3\right\rangle^2}{\sum_{\lambda'=2,4,6}\Omega_{\lambda'}\left\langle {}^4\mathrm{G}_{5/2}\middle\|U^{(\lambda')}\middle\|{}^6\mathrm{H}_{9/2}\right\rangle^2} + \frac{9n^2\hbar\left\langle {}^5\mathrm{D}_4\middle\|L+2S\middle\|{}^7\mathrm{F}_3\right\rangle^2}{4m_e^2c^2(n^2+2)^2\sum_{\lambda'=2,4,6}\Omega_{\lambda'}\left\langle {}^4\mathrm{G}_{5/2}\middle\|U^{(\lambda')}\middle\|{}^6\mathrm{H}_{9/2}\right\rangle^2}\right) \times \left(\frac{P_4(Tb)}{P_4(Sm)}\right) \qquad \textbf{eqn S36}$$

Considering $n = 1.5$ and the values of $\langle {}^4G_{5/2} \| U^{(\lambda\prime)} \| {}^6H_{9/2} \rangle^2$ equal to 0.0096, 0.0061, and 0.0019 for $\lambda' = 2, 4, \text{and } 6$, respectively. The amplitude of each Δ parameter is rationalized owing to three factors: i) $\langle {}^5D_4 \| U^{(\lambda)} \| {}^7F_{J\prime} \rangle^2$, ii) angular frequency $\omega_{4\rightarrow J\prime}$, and iii) $\langle {}^5D_4 \| L + 2S \| {}^7F_{J\prime} \rangle$.

i) The Tb^{3+} $^5D_4 \rightarrow {}^7F_5$ emission has the highest values of $\langle {}^5D_4 \| U^{(\lambda)} \| {}^7F_{J\prime} \rangle^2$ (0.0142, 0.0013, 0.0022)

ii) $\omega_{4\rightarrow 6} > \omega_{4\rightarrow 5} > \omega_{4\rightarrow 3}$

iii) $\langle {}^5D_4 \| L + 2S \| {}^7F_3 \rangle^2 > \langle {}^5D_4 \| L + 2S \| {}^7F_5 \rangle^2 > \langle {}^5D_4 \| L + 2S \| {}^7F_6 \rangle^2$ $(0.68 > 0.16 > 0.00)$

8. Commentary on the Tb^{3+} $^5D_4$ lifetime in the presence of Sm^{3+}

On question can be naturally raised about the changing of the Tb^{3+} $^5D_4$ lifetime with temperature in the mixture Tb_2moshi_8:Sm_2moshi_8 sample (**Table S21**). The first intuitive explanation can be attributed to the Tb^{3+}-to-Sm^{3+} energy transfer, however, each metallacrown molecular unit is formed by one Ln^{3+} type (Tb^{3+} or Sm^{3+}) and the minimum distance between two Ln^{3+} centers in adjacent molecular units is 7 Å, which is considered a long distance for the Ln-Ln interactions.

Our theoretical calculations (section 6.3. Tb^{3+}-to-Sm^{3+} energy transfer and **Table S34**) show that the Tb^{3+}-to-Sm^{3+} energy transfer is indeed negligible ($W = 2.2\ s^{-1}$). Furthermore, it is apparent that, were the Tb^{3+}-to-Sm^{3+} energy transfer mechanism operative, the emission of Sm^{3+} $^4G_{5/2} \rightarrow {}^6H_{9/2}$ should rise with the temperature and this does not happen for the Tb_2moshi_8:Sm_2moshi_8 sample (**Figure 7b**).

Based on the points above and on the Ligand-to-Ln^{3+} energy transfer rates (intramolecular energy transfer), we can rationalize the changing of the Tb^{3+} $^5D_4$ level lifetime as follow:

i) $W_T^b \gg W_T$ for the Tb_2moshi_8 contributes to the population increase of the T_1 state

ii) The T_1 of the Tb_2moshi_8 molecule can transfer energy to the T_1 of the Sm_2moshi_8 (intermolecular energy transfer process) through a Förster-Dexter process.

iii) Once the T_1 is localized on the borders of the metallacrown compounds (Ln^{3+} ions could be seen in the focus of an ellipse), the intermolecular interaction between T_1-to-T_1 should reach shorter distances (< 7 Å), leading to fast energy transfer rates.

iv) Once the energy migrates from Tb_2moshi_8 to the adjacent Sm_2moshi_8 molecule, the Sm^{3+} ion enters in a dynamic equilibrium with the T_1 state due to $W_T \cong W_T^b$. This equilibrium is not affected by the presence of the Tb_2moshi_8 once $W_T \cong W_T^b$ stands for the intramolecular interaction.

The four points above can be visualized in the energy level diagram in **Figure S36**.

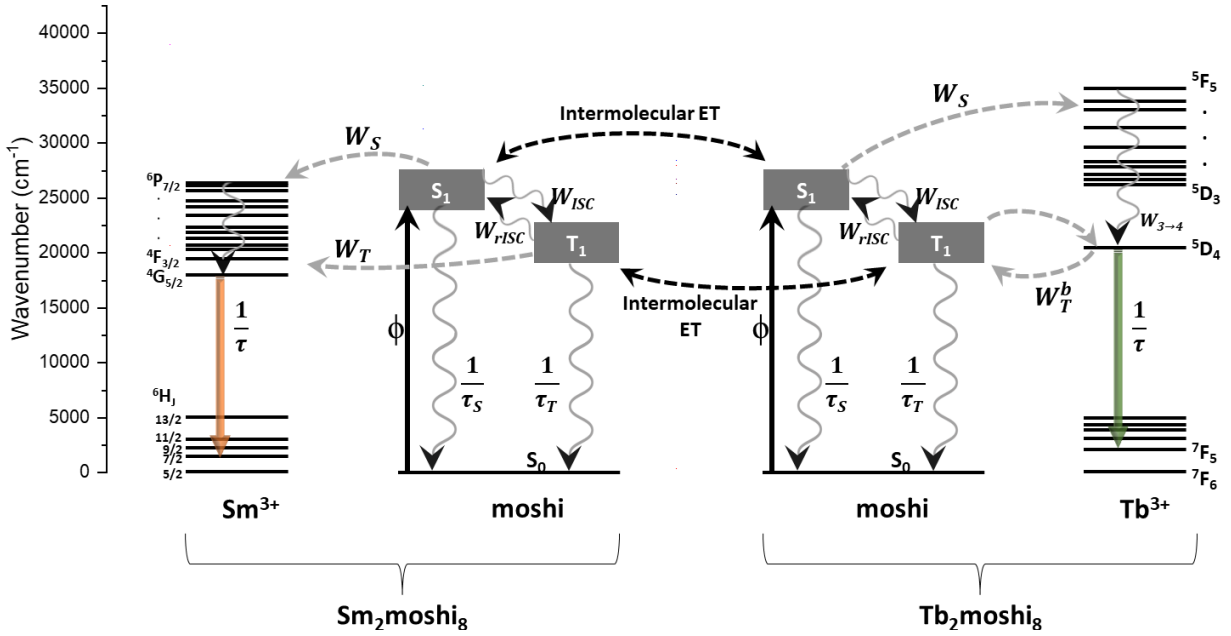

Figure S36. Schematic energy level diagram showing the energy migration in the Tb_2moshi_8:Sm_2moshi_8 mixture. The Tb^{3+} $^5D_4$ has a lifetime decreasing in the presence of Sm_2moshi_8 metallacrow due to the faster backward energy transfer to the T_1 state (W_T^b in the Tb_2moshi_8 side) and afterward, the intermolecular energy transfer (energy migration from Tb_2moshi_8 to Sm_2moshi_8) between T_1 states from different molecules could occur. If the direct Tb^{3+}-to-Sm^{3+} energy transfer is operative, the Sm^{3+} emission intensity should be increased and this is not observed (see **Figure 7B**).

9. References

(1) Nguyen, T. N.; Chow, C. Y.; Eliseeva, S. V.; Trivedi, E. R.; Kampf, J. W.; Martinić, I.; Petoud, S.; Pecoraro, V. L. One-Step Assembly of Visible and Near-Infrared Emitting Metallacrown Dimers Using a Bifunctional Linker. *Chem. - A Eur. J.* **2018**, *24* (5), 1031–1035. https://doi.org/10.1002/chem.201703911.

(2) Cirera, J.; Ruiz, E.; Alvarez, S. Continuous Shape Measures as a Stereochemical Tool in Organometallic Chemistry. *Organometallics* **2005**, *24* (7), 1556–1562. https://doi.org/10.1021/om049150z.

(3) Llunell, M.; Casanova, D.; Cicera, J.; Alemany, P.; Alvarez, S. Shape Version 2.1. Barcelona, Spain 2013.

(4) Judd, B. R. Optical Absorption Intensities of Rare-Earth Ions. *Phys. Rev.* **1962**, *127* (3), 750–761. https://doi.org/10.1103/PhysRev.127.750.

(5) Ofelt, G. S. Intensities of Crystal Spectra of Rare-Earth Ions. *J. Chem. Phys.* **1962**, *37* (3), 511–520. https://doi.org/10.1063/1.1701366.

(6) Jørgensen, C. K.; Judd, B. R. Hypersensitive Pseudoquadrupole Transitions in Lanthanides. *Mol. Phys.* **1964**, *8* (3), 281–290. https://doi.org/10.1080/00268976400100321.

(7) Wybourne, B. G. *Spectroscopic Properties of Rare Earths*; John Wiley & Sons, 1965.

(8) Moura Jr, R. T.; Carneiro Neto, A. N.; Longo, R. L.; Malta, O. L. On the Calculation and Interpretation of Covalency in the Intensity Parameters of 4f–4f Transitions in Eu^{3+} Complexes Based on the Chemical Bond Overlap Polarizability. *J. Lumin.* **2016**, *170*, 420–430. https://doi.org/10.1016/j.jlumin.2015.08.016.

(9) Carneiro Neto, A. N.; Teotonio, E. E. S.; de Sá, G. F.; Brito, H. F.; Legendziewicz, J.; Carlos, L. D.; Felinto, M. C. F. C.; Gawryszewska, P.; Moura, R. T.; Longo, R. L.; Faustino, W. M.; Malta, O. L. Modeling Intramolecular Energy Transfer in Lanthanide Chelates: A Critical Review and Recent Advances; 2019; pp 55–162. https://doi.org/10.1016/bs.hpcre.2019.08.001.

(10) Carneiro Neto, A. N.; Moura Jr., R. T. Overlap Integrals and Excitation Energies Calculations in Trivalent Lanthanides 4f Orbitals in Pairs Ln-L (L = Ln, N, O, F, P, S, Cl, Se, Br, and I). *Chem. Phys. Lett.* **2020**, *757*, 137884. https://doi.org/10.1016/j.cplett.2020.137884.

(11) Malta, O. L. Theoretical Crystal-Field Parameters for the YOCl:Eu^{3+} System. A Simple Overlap Model. *Chem. Phys. Lett.* **1982**, *88* (3), 353–356. https://doi.org/10.1016/0009-2614(82)87103-0.

(12) Malta, O. L. A Simple Overlap Model in Lanthanide Crystal-Field Theory. *Chem. Phys. Lett.* **1982**, *87* (1), 27–29. https://doi.org/10.1016/0009-2614(82)83546-X.

(13) Moura, R. T.; Carneiro Neto, A. N.; Longo, R. L.; Malta, O. L. On the Calculation and Interpretation of Covalency in the Intensity Parameters of 4f-4f Transitions in Eu3+ Complexes Based on the Chemical Bond Overlap Polarizability. *J. Lumin.* **2016**, *170*, 420–430. https://doi.org/10.1016/j.jlumin.2015.08.016.

(14) Carneiro Neto, A. N.; Moura, R. T.; Aguiar, E. C.; Santos, C. V; de Medeiros, M. A. F. L. B. Theoretical Study of Geometric and Spectroscopic Properties of Eu(III) Complexes with Ruhemann's Purple Ligands. *J. Lumin.* **2018**, *201* (83), 451–459. https://doi.org/10.1016/j.jlumin.2018.05.014.

(15) Malta, O. L.; Batista, H. J.; Carlos, L. D. Overlap Polarizability of a Chemical Bond: A Scale of Covalency and Application to Lanthanide Compounds. *Chem. Phys.* **2002**, *282* (1), 21–30. https://doi.org/10.1016/S0301-0104(02)00631-6.

(16) Moura, R. T.; Malta, O. L.; Longo, R. L. The Chemical Bond Overlap Plasmon as a Tool for Quantifying Covalency in Solid State Materials and Its Applications to Spectroscopy. *Int. J. Quantum Chem.* **2011**, *111* (7–8), 1626–1638. https://doi.org/10.1002/qua.22782.

(17) Moura, R. T.; Duarte, G. C. S.; Da Silva, T. E.; Malta, O. L.; Longo, R. L. Features of Chemical Bonds Based on the Overlap Polarizabilities: Diatomic and Solid-State Systems with the Frozen-Density Embedding Approach. *Phys. Chem. Chem. Phys.* **2015**, *17* (12), 7731–7742. https://doi.org/10.1039/c4cp05283h.

(18) Carneiro Neto, A. N.; Aguiar, E. C.; Santos-Jr., C. V.; de Lima, E. M.; Shyichuk, A.; Teotonio, E. E. S.; Faustino, W. M.; Brito, H. F.; Felinto, M. C. F. C.; Ferreira, R. A. S.; Longo, R. L.; Carlos, L. D.; Malta, O. L.; Moura Jr., R. T. JOYSpectra - Program for lanthanides luminescence calculations.

(19) Assunção, I. P.; Carneiro Neto, A. N.; Moura, R. T.; Pedroso, C. C. S.; Silva, I. G. N.; Felinto, M. C. F. C.; Teotonio, E. E. S.; Malta, O. L.; Brito, H. F. Odd-Even Effect on Luminescence Properties of Europium Aliphatic Dicarboxylate Complexes. *ChemPhysChem* **2019**, *20* (15), 1931–1940. https://doi.org/10.1002/cphc.201900603.

(20) Adati, R.; Monteiro, J.; Cardoso, L.; de Oliveira, D.; Jafelicci, M.; Davolos, M. The Influence of Different Ammonium Cations on the Optical Properties of Tetrakis GdIII and EuIII Complexes. *J. Braz. Chem. Soc.* **2019**, *30* (8), 1707–1716. https://doi.org/10.21577/0103-5053.20190073.

(21) Malta, O. L. Ligand—Rare-Earth Ion Energy Transfer in Coordination Compounds. A Theoretical Approach. *J. Lumin.* **1997**, *71* (3), 229–236. https://doi.org/10.1016/S0022-2313(96)00126-3.

(22) Carnall, W. T.; Crosswhite, H.; Crosswhite, H. M. *Energy Level Structure and Transition Probabilities in the Spectra of the Trivalent Lanthanides in LaF_3*; Argonne, IL, United States, 1978. https://doi.org/10.2172/6417825.

(23) Smentek, L. Theoretical Description of the Spectroscopic Properties of Rare Earth Ions in Crystals. *Phys. Rep.* **1998**, *297* (4), 155–237. https://doi.org/10.1016/S0370-1573(97)00077-X.

(24) Edvardsson, S.; Klintenberg, M. Role of the Electrostatic Model in Calculating Rare-Earth Crystal-Field Parameters. *J. Alloys Compd.* **1998**, *275–277*, 230–233. https://doi.org/10.1016/S0925-8388(98)00309-0.

(25) Carneiro Neto, A. N.; Moura, R. T.; Malta, O. L. On the Mechanisms of Non-Radiative Energy Transfer between Lanthanide Ions: Centrosymmetric Systems. *J. Lumin.* **2019**, *210*, 342–347. https://doi.org/10.1016/j.jlumin.2019.02.049.

(26) Malta, O. L. Mechanisms of Non-Radiative Energy Transfer Involving Lanthanide Ions Revisited. *J. Non. Cryst. Solids* **2008**, *354* (42–44), 4770–4776. https://doi.org/10.1016/j.jnoncrysol.2008.04.023.

(27) Ofelt, G. S. Structure of the f^6 Configuration with Application to Rare-Earth Ions. *J. Chem. Phys.* **1963**, *38* (9), 2171–2180. https://doi.org/10.1063/1.1733947.

(28) Kasprzycka, E.; Carneiro Neto, A. N.; Trush, V. A.; Jerzykiewicz, L.; Amirkhanov, V. M.; Malta, O. L.; Legendziewicz, J.; Gawryszewska, P. How Minor Structural Changes Generate Major Consequences in Photophysical Properties of RE Coordination Compounds; Resonance Effect, LMCT State. *J. Rare Earths* **2020**, *38* (5), 552–563. https://doi.org/10.1016/j.jre.2020.02.001.

(29) Aquino, L. E. do N.; Barbosa, G. A.; Ramos, J. de L.; O. K. Giese, S.; Santana, F. S.; Hughes, D. L.; Nunes, G. G.; Fu, L.; Fang, M.; Poneti, G.; Carneiro Neto, A. N.; Moura, R. T.; Ferreira, R. A. S.; Carlos, L. D.; Macedo, A. G.; Soares, J. F. Seven-Coordinate Tb^{3+} Complexes with 90% Quantum Yields: High-Performance Examples of Combined Singlet- and Triplet-to-Tb^{3+} Energy-Transfer Pathways. *Inorg. Chem.* **2021**, *60* (2), 892–907. https://doi.org/10.1021/acs.inorgchem.0c03020.

(30) Samanta, P. K.; Kim, D.; Coropceanu, V.; Brédas, J.-L. Up-Conversion Intersystem Crossing Rates in Organic Emitters for Thermally Activated Delayed Fluorescence: Impact of the Nature of Singlet vs Triplet Excited States. *J. Am. Chem. Soc.* **2017**, *139* (11), 4042–4051. https://doi.org/10.1021/jacs.6b12124.

(31) Wang, L.; Ou, Q.; Peng, Q.; Shuai, Z. Theoretical Characterizations of TADF Materials: Roles of ΔG and the Singlet–Triplet Excited States Interconversion. *J. Phys. Chem. A* **2021**, *125* (7), 1468–1475. https://doi.org/10.1021/acs.jpca.0c09767.

(32) Brédas, J. L.; Beljonne, D.; Coropceanu, V.; Cornil, J. Charge-Transfer and Energy-Transfer Processes in π-Conjugated Oligomers and Polymers: A Molecular Picture. *Chem. Rev.* **2004**, *104* (11), 4971–5003. https://doi.org/10.1021/cr040084k.

(33) Schmidt, K.; Brovelli, S.; Coropceanu, V.; Beljonne, D.; Cornil, J.; Bazzini, C.; Caronna, T.; Tubino, R.; Meinardi, F.; Shuai, Z.; Brédas, J.-L. Intersystem Crossing Processes in Nonplanar Aromatic Heterocyclic Molecules. *J. Phys. Chem. A* **2007**, *111* (42), 10490–10499. https://doi.org/10.1021/jp075248q.

(34) Beltrán-Leiva, M. J.; Solis-Céspedes, E.; Páez-Hernández, D. The Role of the Excited State Dynamic of the Antenna Ligand in the Lanthanide Sensitization Mechanism. *Dalt. Trans.* **2020**, *49* (22), 7444–7450. https://doi.org/10.1039/D0DT01132K.

(35) El-Sayed, M. A. Spin—Orbit Coupling and the Radiationless Processes in Nitrogen Heterocyclics. *J. Chem. Phys.* **1963**, *38* (12), 2834–2838. https://doi.org/10.1063/1.1733610.

(36) Kasha, M. Characterization of Electronic Transitions in Complex Molecules. *Discuss. Faraday Soc.* **1950**, *9* (c), 14–19. https://doi.org/10.1039/df9500900014.

(37) Hairer, E.; Wanner, G. Radau Methods. In *Encyclopedia of Applied and Computational Mathematics*; Engquist, B., Ed.; Springer Berlin Heidelberg: Berlin, Heidelberg, 2015; pp 1213–1216. https://doi.org/10.1007/978-3-540-70529-1_139.

(38) Carnall, W. T.; Crosswhite, H.; Crosswhite, H. M. *Energy Level Structure and Transition Probabilities in the Spectra of the Trivalent Lanthanides in LaF/Sub 3/. [Tables, Diagrams]*; Argonne, IL (United States), 1978. https://doi.org/10.2172/6417825.